SANDIA REPORT
SAND2010-0171
Unlimited Release
Printed September 2010

Operation and Analysis of a Supercritical CO_2 Brayton Cycle

Steven A. Wright, Ross F. Radel, Milton E. Vernon, Gary E. Rochau, and Paul S. Pickard

Prepared by
Sandia National Laboratories
Albuquerque, New Mexico 87185 and Livermore, California 94550

Sandia is a multiprogram laboratory operated by Sandia Corporation,
a Lockheed Martin Company, for the United States Department of Energy's
National Nuclear Security Administration under Contract DE-AC04-94AL85000.

Issued by Sandia National Laboratories, operated for the United States Department of Energy by Sandia Corporation.

Available to DOE and DOE contractors from
U.S. Department of Energy
Office of Scientific and Technical Information
P.O. Box 62
Oak Ridge, TN 37831

Telephone: (865) 576-8401
Facsimile: (865) 576-5728
E-Mail: reports@adonis.osti.gov
Online ordering: http://www.osti.gov/bridge

Available to the public from
U.S. Department of Commerce
National Technical Information Service
5285 Port Royal Rd.
Springfield, VA 22161

Telephone: (800) 553-6847
Facsimile: (703) 605-6900
E-Mail: orders@ntis.fedworld.gov
Online order: http://www.ntis.gov/help/ordermethods.asp?loc=7-4-0#online

SAND2010-0171
Unlimited Release
Printed September 2010

Operation and Analysis of a Supercritical CO_2 Brayton Cycle

Steven Wright, Ross Radel, Milton Vernon, Gary Rochau, and Paul Pickard
Advanced Nuclear Concepts Department
Sandia National Laboratories
P.O. Box 5800
Albuquerque, New Mexico 87185-MS1136

Abstract

Sandia National Laboratories is investigating advanced Brayton cycles using supercritical working fluids for use with solar, nuclear or fossil heat sources. The focus of this work has been on the supercritical CO_2 cycle (S-CO2) which has the potential for high efficiency in the temperature range of interest for these heat sources, and is also very compact, with the potential for lower capital costs. The first step in the development of these advanced cycles was the construction of a small scale Brayton cycle loop, funded by the Laboratory Directed Research & Development program, to study the key issue of compression near the critical point of CO_2. This document outlines the design of the small scale loop, describes the major components, presents models of system performance, including losses, leakage, windage, compressor performance, and flow map predictions, and finally describes the experimental results that have been generated.

THIS PAGE IS INTENTIONALLY BLANK

CONTENTS

TABLE OF FIGURES

Table of Tables

NOMENCLATURE

ASME	American Society of Mechanical Engineers
BNI	Barber-Nichols Incorporated
BWR	Boiling Water Reactor
DOE	Department of Energy
FEA	Finite Element Analysis
GenIV	Generation IV International Forum
IGBT	Insulated Gate Bipolar Transistor
KAPL	Knolls Atomic Power lab
LDRD	Laboratory Directed Research & Development
MAWP	Maximum Allowable Working Pressure
MCFV	Main-Compressor-Flow-Valve
NASA	National Aeronautics and Space Administration
NIST	National Institute of Standards and Technology
NRC	Nuclear Regulatory Commission
OD	Outside Diameter
PID	Proportional–Integral–Derivative
PWR	Pressurized Water Reactor
Refprop	NIST Reference Fluid Thermodynamic and Transport Properties Database
RPCSIM	Reactor Power and Control SIMulation code
RTD	Resistance Temperature Detectors
S-CO_2	Supercritical Carbon Dioxide
SCR	Silicon Controlled Rectifier
SNL	Sandia National Laboratories
TAC	Turbo-Alternator-Compressor
TRACE	TRAC/RELAP Advanced Computational Engine
T-D	Temperature-Density
T-S	Temperature-Entropy

1 Introduction

Sandia National Laboratories is investigating advanced Brayton cycles using supercritical working fluids for use with solar, nuclear or fossil heat sources. The focus of this work has been on the supercritical CO_2 cycle (S-CO_2) which has the potential for high efficiency in the temperature range of interest for these heat sources, and is also very compact, with the potential for lower capital costs. The first step in the development of these advanced cycles was the construction of a small scale Brayton cycle loop, funded by the Laboratory Directed Research & Development (LDRD) program, to study the key issue of compression near the critical point of supercritical working fluids. The small scale loop uses modular and reconfigurable hardware to form the necessary cycle configurations needed to investigate the key features and technologies of supercritical Brayton cycles This document outlines the design of the small scale loop, describes the major components, presents models of system and compressor performance, and describes the experimental results that have been.

Past efforts to study the S-CO_2 Brayton cycle have largely been analytical efforts (Dostal, 2004; Gong, 2006). Prior to the S-CO_2 work, SNL conducted an experimental study on low pressure closed Brayton cycles; Wright, 2006). It was this experiment that provided many insights about the fundamental operating principles of closed Brayton cycles and led to the effort to build a high pressure S-CO_2 Brayton loop.

This effort is hardware focused and requires the development of turbo-alternator-compressor technologies capable of operating with supercritical CO_2 at very high power densities, high speeds, high pressures, and high fluid densities. Component and system design studies were performed by both Sandia and Barber-Nichols Incorporated (BNI) to develop the specifications and component designs for the S-CO_2 compression and Brayton cycle test loops.

The key component of these loops is the turbo-alternator-compressor unit (TAC) and the technologies used in its design. In its final configuration, the TAC uses gas foil bearings, a high speed permanent magnet motor/alternator and labyrinth gas seals to reduce the rotor cavity pressure. Because of the extremely high power densities and fluid density, Sandia has filed a Technical Advance for the TAC design. The early tests are focused on measuring leakage flow rates, windage losses, balancing thrust loads and measuring the compressor performance characteristics. Many of these early tests used ball bearings (with limited life) rather than gas foil bearings to allow for early testing and to minimize gas foil bearing development risks.

SNL is working to develop large (>10 MW) S-CO_2 Brayton units for various electrical production schemes. As a first step in a phased development program, Sandia has contracted BNI, a small specialty turbo-machinery corporation (Barber Nichols, 2008), to perform detailed design, manufacture, and assembly of the S-CO_2 compression loop. This early Sandia S-CO_2 compression loop is intended to study the stability and control issues of the supercritical Brayton cycle near the critical point (Wright, 2008). The manufacture and assembly of the S-CO_2 loop was completed in May 2008. The testing and commissioning phase of this device continued through the end of the 2009 fiscal year. This document summarizes the performance characteristics of the turbomachinery and operating characteristics of the loop.

The report begins by first summarizing the design, status of assembly, and expected performance of the S-CO_2 loop. The next section describes the major components of the supercritical Brayton loop. Each component section includes a description of the component and its expected operating characteristics, illustrates the design and manufacture of that component with engineering design drawings and photos, includes a detailed analysis of that component using SNL's and BNI's steady state and dynamic design and analysis codes followed by measured data. The analysis section includes predictions and measurements of losses, leakage, windage, compressor performance, compressor inlet temperature and pressure control performance, and flow map predictions and measurements where available. The development and validation models that are capable of predicting these operational performance characteristics in supercritical CO_2 are important. Many models and fits are available for air and steam, but very little data exists for supercritical fluids, and the development and validation of these models is one of the main purposes of performing these tests. The final section of this report describes the experimental results that have been generated using the S-CO_2 compression and Brayton loops. These include a summary of the development, operation, and control experiments and results. More details can be found in the many reports generated by the S-CO_2 Brayton team. Some of these reports are listed below and are detailed in the references section.

- Status Report of Small Scale S- CO_2 Brayton Cycle Demonstration Program (2007)
- Supercritical CO_2 Brayton Cycle Compression and Control Near the Critical Point (2008)
- Initial status and test results for a supercritical CO_2 Brayton cycle test-loop (2008)
- Design of the Gen IV Supercritical CO_2 Split-flow Compressor Test Loop (2008)
- Analysis of Supercritical CO_2 Compressor Operation Near the Critical Point of CO_2 (2008)
- Gen IV S-CO_2 Brayton Cycle Test Loop Design and Split-flow S-CO_2 Compressor Test Loop Construction Description (2009)
- Supercritical CO_2 Compression Loop Operation and Test Results (2009)
- Supercritical CO_2 Heated, but Un-recuperated, Brayton Loop Operation and Test Results (2009)
- Supercritical CO_2 Test Loop Operation and First Test Results (2009)
- Supercritical CO_2 Brayton Cycle Power Generation Development Program and Initial Test Results (2009)

THIS PAGE IS INTENTIONALLY BLANK

2 S-CO_2 Compression Test Loop Summary

Sandia and its contractor Barber Nichols Inc. (Barber Nichols, 2008) have fabricated and are operating a supercritical CO_2 (S-CO_2) compression test-loop to investigate the key technology issues associated with this cycle. The key issues for the supercritical Brayton cycle include the fundamental issues of compressor fluid performance and system control near the critical point. Near the critical point very non-ideal fluid behavior is observed which often means that standard models for analyzing compressor performance cannot be used. Thus, one of the goals of the program is to develop data that can be used to validate the tools and models that are used to design the turbomachinery. Other supporting technology issues have also been investigated including bearing type, thrust loading, bearing cooling, sealing technologies, and rotor windage losses.

In the testing to date, the turbomachinery has reached maximum speeds of 65,000 rpm, peak flow rates of over 4.1 kg/s (9 lb/s) and pressure ratios of just over 1.65, at compressor inlet densities near 70% the density of water. The data from these tests indicate that the basic design and performance predictions for the compression loop are sound. The compression loop has operated the turbo-compressor on the liquid and vapor side of the saturation curve, very near the critical point, above the critical point and even in the saturation curve. The compressor has been operated near the choked flow regime and even in surge. At the current operating speeds and pressures, the observed performance map data agrees well with the model predictions and the results are presented in this report. These results have positive implications for the ultimate success of the S-CO_2 cycle.

2.1 *S-CO_2 Compression Test Loop and Hardware*

Figure 2-1 shows an engineering drawing of the supercritical compression test-loop. The loop sits on a skid that is approximately 2m x 3m and contains a motor-driven radial compressor, its motor/alternator controller, a flow meter orifice, and pressure drop orifice, a tube-and-shell gas-chiller, and miscellaneous compressors and ducting to control the rotor cavity pressure to reduce windage losses and to allow for fill and purge operations. The loop is modular and reconfigurable which allows the testing progress in phases and spreads the cost of hardware over a two-to-three year period.

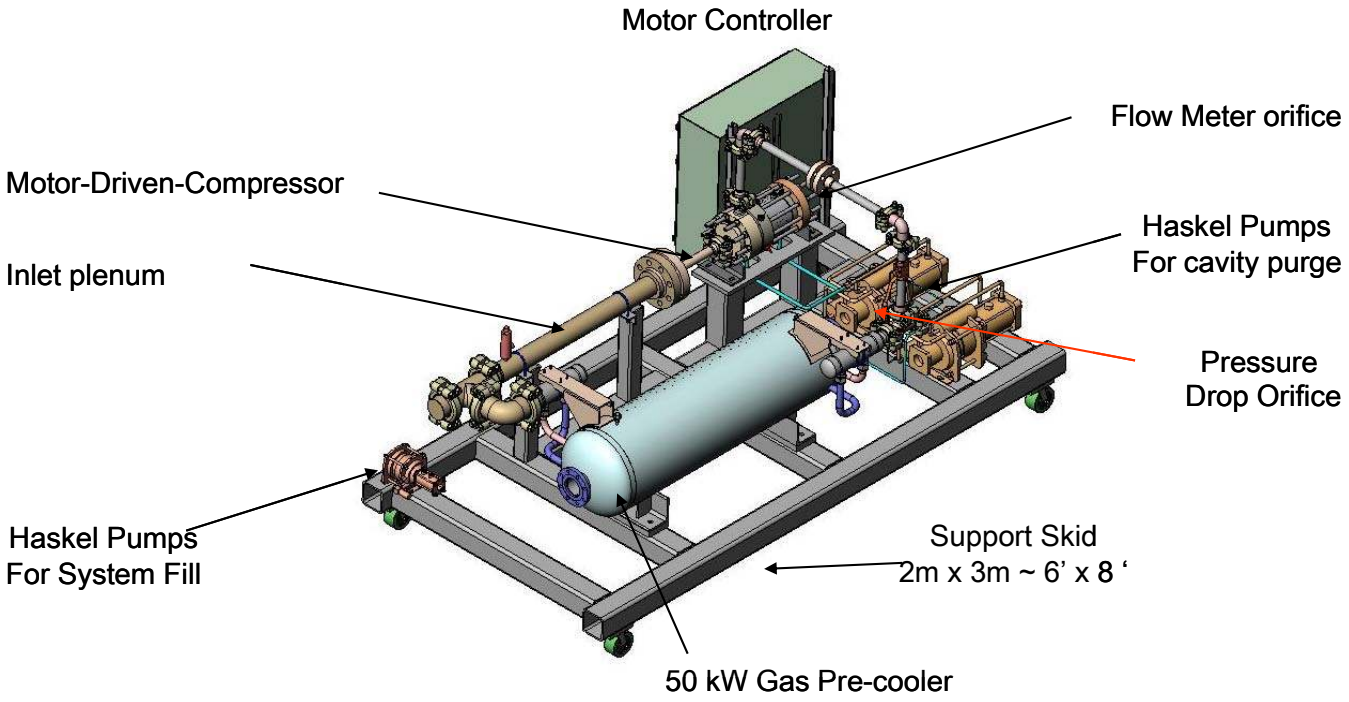

Figure 2-1: Engineering drawing of S-CO_2 Compression loop test skid.

A schematic layout of the compression loop, including the water cooling loop, is provided in Figure 2-2. Estimates of the state points, based on thermodynamic cycle analysis that show the temperature, pressure, flow rate, and power level of the components, are also provided. The "compression" loop consists of a motor-driven radial compressor (~50 kW), a flow meter (located after the compressor), a pressure drop orifice (in place of the turbine), and a gas chiller (50 kW). The main compressor in this loop is designed to operate at 75,000 rpm with a pressure ratio of 1.8 and a mass flow rate of 3.5 kg/s. These operating conditions are representative of the main compressor that will be used in all subsequent S-CO_2 Brayton loops (Wright, 2008). Notice that the entire 50 kW of heater power is rejected across the gas chiller, but that the temperature difference across the gas chiller is only 0.7 K for the design flow rate of 3.5 kg/s. This small change in temperature for such a large heat transfer is simply a reflection of the non-ideal properties that occur in CO_2 near the critical point and also illustrates some of the control issues.

The key component in this supercritical compression loop is the motor-driven compressor unit which is shown in Figure 2-3 as an engineering drawing. The first configuration of the motor-driven compression unit uses ball bearings. This allowed the thrust load to be measured via a load cell. The ball bearings are expected to have a limited lifetime that varies from 20 hours to 2000 hours depending on the thrust load that is assumed. The switch to gas-foil bearings was made in May of 2009.

A photo of the as-built and assembled S-CO_2 compression loop is shown in Figure 2-4. The photo shows a portion of the motor control system on the left side of the image. The data acquisition and control system is sitting on a cart, and the turbomachinery is located just above the data acquisition computer monitor. The large blue tank in the back of the image is the 50 kW tube-a-shell spiral heat exchanger. The water cooling was initially provided by PVC tubing that has since been changed to copper.

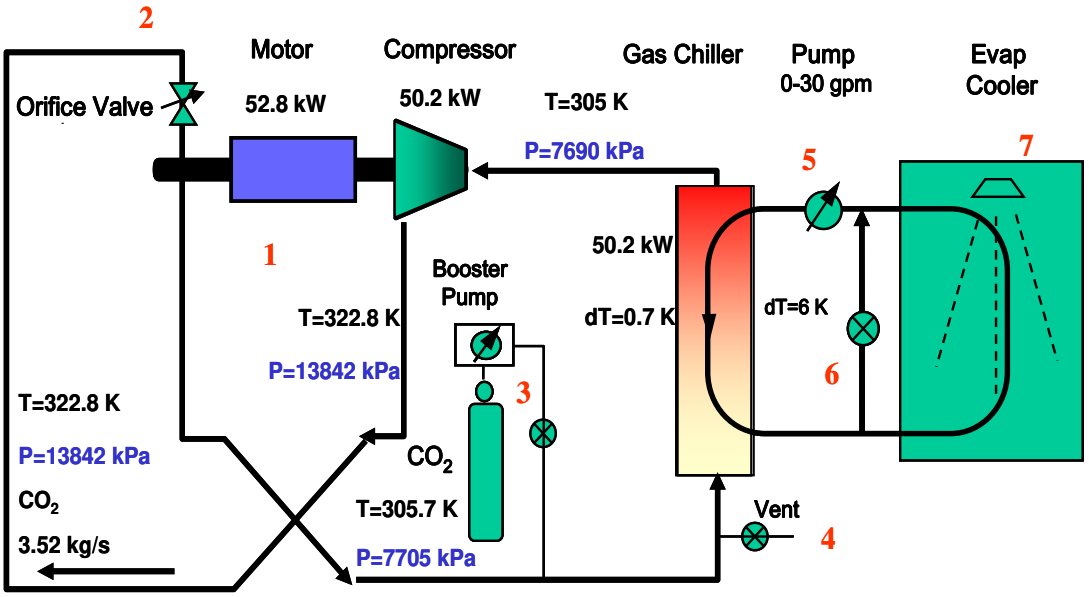

Figure 2-2: Schematic of supercritical compression loop using a 50 kWe motor driving a radial compressor at 75,000 rpm with a flow rate of 3.51 kg/s.

The S-CO_2 compression loop with various alternative configurations has seen over 80 tests since it was constructed in June of 2008. In May, 2009, the gas-foil bearings were also installed and run. It has proven to be a very flexible, robust, and valuable tool, that has attracted considerable interest and separate funding to extend the testing capabilities of the Sandia S-CO_2 compression loop.

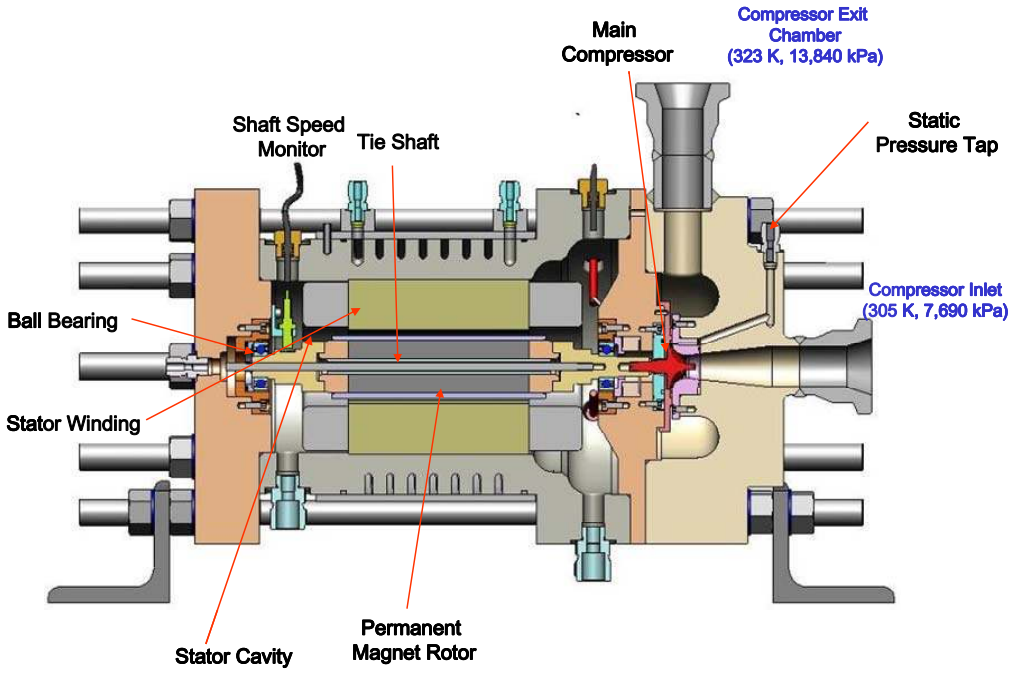

Figure 2-3: Schematic drawing of the motor-driven S- CO_2 compressor. This configuration uses ball bearings and has no turbine.

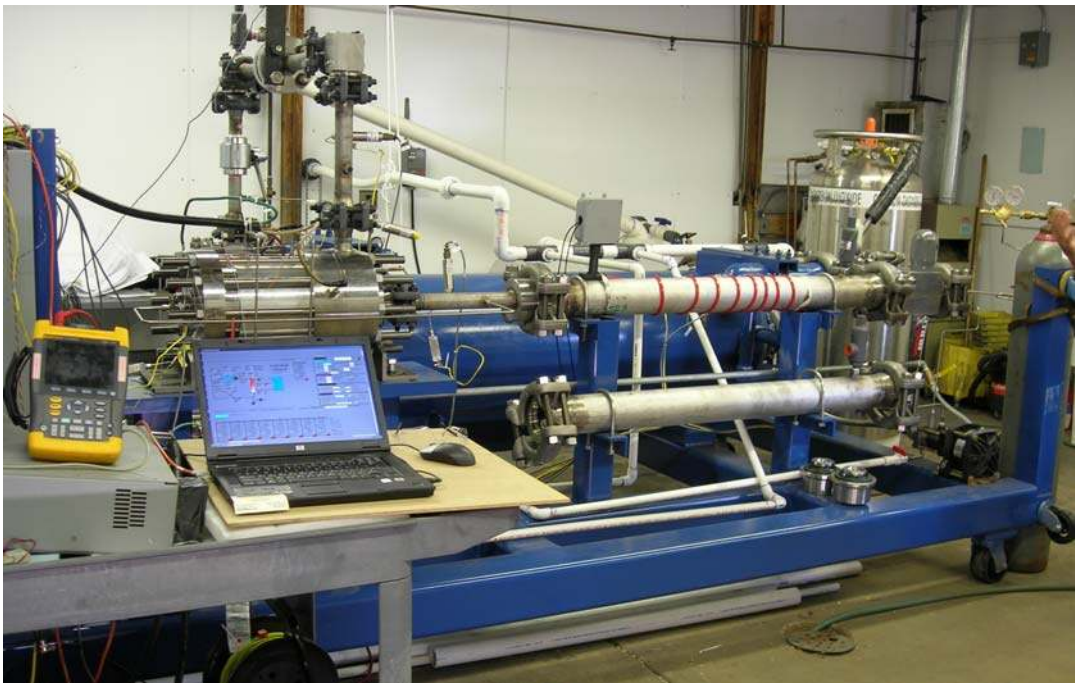

Figure 2-4: Photo of the Sandia S-CO_2 compression loop as assembled during the summer of 2008.

2.2 *S-CO_2 Heated but Un-recuperated Brayton Loop and Turbomachine*

The motor-driven compressor unit was designed so that a small turbine could be added to the rotating shaft in addition to the compressor. Because elastomers are used to seal the components on the turbomachine, the turbine hot inlet temperature must not exceed of about 560-600 K. In addition the small turbine was intended only to provide motor-assist power to reduce the motor power requirements. Still, cycle calculations indicate that power can be produced if the turbine inlet temperature is sufficiently high. Gas foil bearings can also be used. The gas-foil bearings were added because of the limited life of the ball bearings. The ball bearing race housings are instrumented with thermistors to measure the temperature. Similarly the gas-foil bearing support structure was instrumented with thermsitors as well. The switch to gas-foil bearings was made after sufficient thrust load measurements were made to assure that the actual thrust loads were within the capability of the gas-foil bearing thrust load.

In January, 2009, the turbomachinery was reconfigured to run with the turbine (Figure 2-5) using ball bearings. The compression loop was modified by adding 260 kW of heater power to form a heated, but un-recuperated, Brayton loop. This new configuration of the loop and several tests was contracted by Knolls Atomic Power Lab (KAPL). The turbine is very small (1.2 inches in diameter). It operates at low temperatures and was intended to provide about 10 kW of motor-assist power to increase the flow and pressure ratio capabilities of the loop. However, its small size allows it to produce considerable power even at low temperatures. The heated, but un-recuperated Brayton test results indicate that (when windage is excluded) the turbo-compressor is very near break-even conditions for a turbine inlet temperature as low as 60°C. Break-even, means that the turbine is producing almost as much power as the compressor uses. This is useful as it may allow future operations that make power at low temperature.

Figure 2-5 shows the LDRD turbo-alternator-compressor with the small turbine and the gas foil bearings installed. Figure 2-6 shows a schematic of the heated, but un-recuperated, Brayton loop and the instrumentation labels. In the schematic the black lines show the main S-CO_2 flow path while the red lines show the cavity purge lines. The label names for the temperature and pressure transducers are shown as T100 or P100, etc. An engineering drawing of the heated, but un-recuperated Brayton loop is shown in Figure 2-7, and a photo of the actual loop is presented in Figure 2-8. Notice that a Micro Motion Coriolis flow meter was installed in this loop to measure the compressor inlet flow rate and density. This device is very useful and also very accurate. The results from tests while the loop was in this configuration are described in Heated Un-recuperated Brayton Loop Results 5.8.

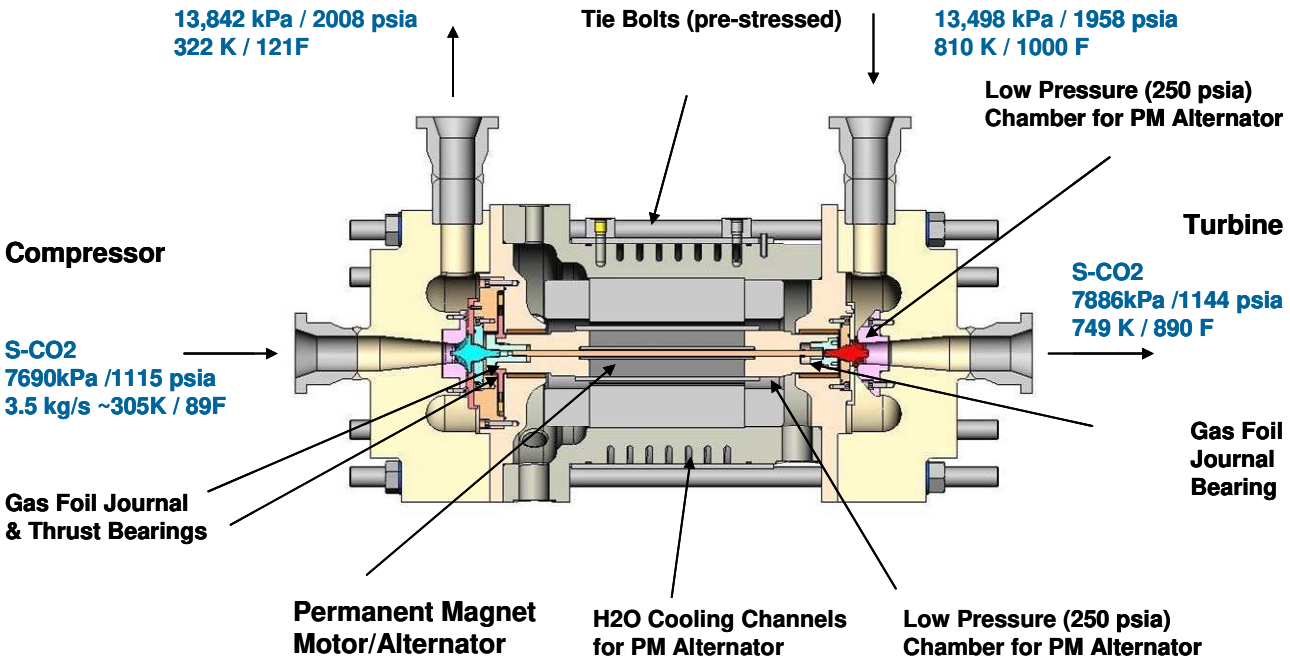

Figure 2-5: Turbo-alternator-shaft design for the SNL S-CO_2 test loop. This configuration uses gas-foil bearings and includes a small turbine (red).

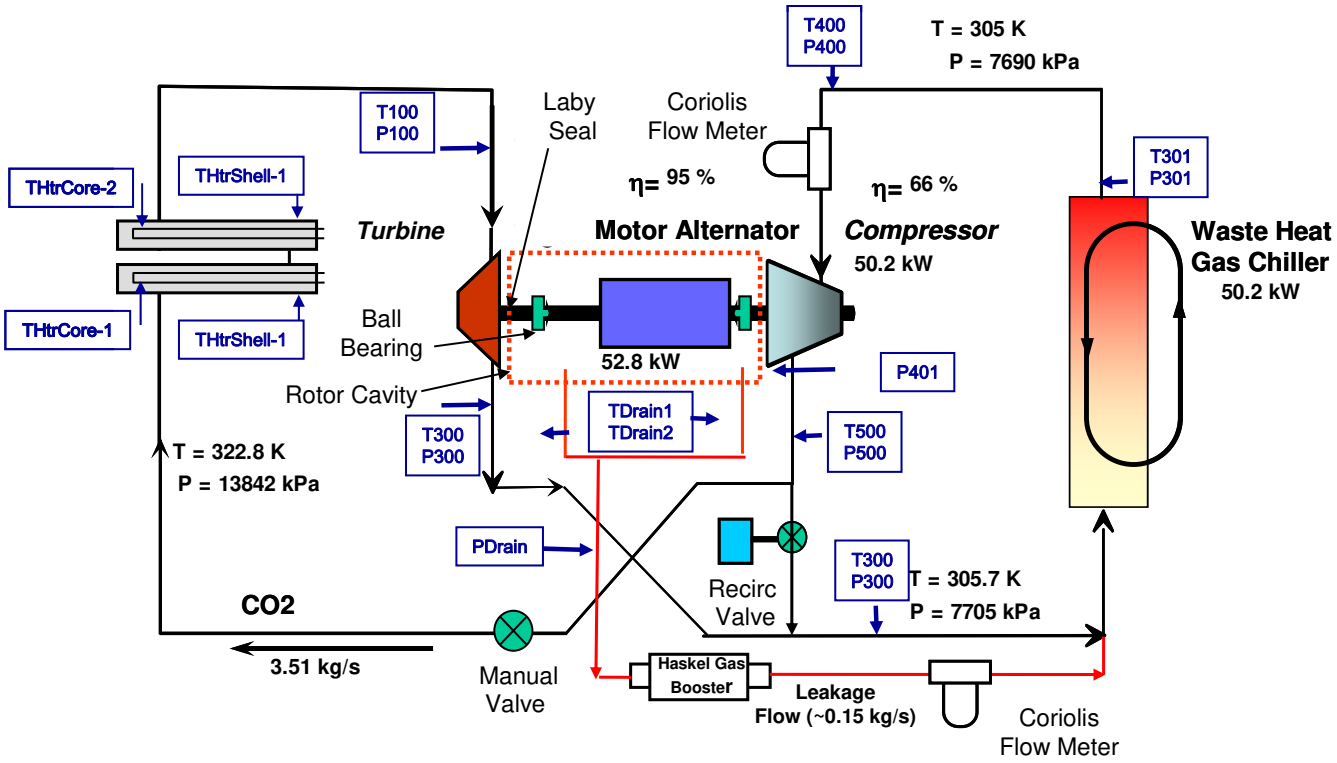

Figure 2-6: Simple diagram of the heated un-recuperated supercritical CO_2 Brayton loop.

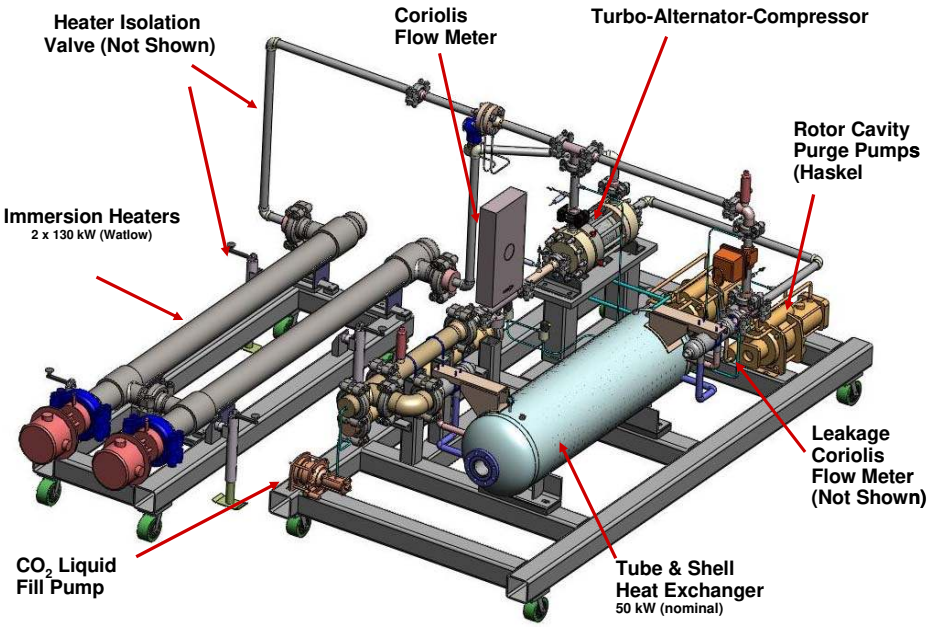

Figure 2-7: Engineering drawing of the heated but un-recuperated Brayton loop.

Figure 2-8: Photo of the heated, but un-recuperated, Brayton Loop. The foreground shows the heaters, the back ground shows the modified S-CO_2 test loop with the turbomachine configured as a turbo-alternator-compressor.

2.3 *Summary of Loop Operating Conditions Near the Critical Point*

The Temperature-Entropy (T-S) path that the CO_2 fluid takes in the gas chiller, the compressor and the recuperator is shown as a green dashed line in Figure 2-9. The green dots indicate the approximate temperature-entropy state points at the chiller inlet, the main compressor inlet and the compressor outlet. The T-S figure shows the lines of constant pressure. For convenience the lines of constant density are also shown as short red lines. On the right side of the saturation curve the fluid is more vapor like and the densities are on the order of 15% to 30% the density of water. In contrast on the left side of the dome (saturation curve) the fluid densities are more liquid like, 65%-80% the density of water.

In the compression process (vertical dotted green line), even though the pressure ratio is 1.8, the density changes only by 10% (from 0.608 kg/liter to 0.670 kg/liter). This "near-incompressibility" coupled with the high fluid density causes the power in the compressor to be low compared to an ideal gas. This very low power in the main compressor is one of the main reasons why the supercritical Brayton cycle achieves high efficiency. Another important non-ideal gas property is the large increase in heat capacity that occurs near the critical point. The process of vaporization that occurs below the critical temperature (31°C or 88°F) is still occurring above the "dome" (saturation curve). The heat of vaporization now shows up in the single phase region as a large increase in heat capacity. There are also large decreases in

density and increases in viscosity that occur above the dome as well, generally along the pseudo critical line shown as the blue dashed line in Figure 2-9. These increases are large. The heat capacity increases by over a factor of 10-30 depending on the pressure. This effect also increases the heat transfer coefficient because the heat transfer near the critical point is nearly a two-phase vaporization/condensation process and hence occurs very nearly at a constant temperature. This therefore causes a very low dT in the heat rejection gas-chiller. Because this small temperature change (dT) makes the cycle more "Carnot" like, it also results in and efficiency increase.

The effect of the pseudo-critical point is clearly seen in the operating state point values shown in Figure 2-2. Here the temperature drop in the gas chiller (which is rejecting 50.2 kW) is only 0.7 K due to the large increase in heat capacity. Again this illustrates the very high power density available in S-CO_2 systems.

These phenomena reveal two important practical control issues:
1. a very large amount of heat transfer is required to change the temperature, even by a little as 1 K (in the gas chiller) when the CO_2 is near the critical point, and
2. it will be very difficult to measure or to know the real fluid temperature to within a few tenths of a degree, let alone control it to within a few tenths of a degree K.

There are other factors that one wishes to control or manage to avoid potential operational difficulties. A control system is desired that will avoid allowing the compressor inlet conditions from entering the liquid–vapor dome of the T-S diagram. It is generally thought that pumping a two phase mixture will be more difficult for axial compressors, which is one of the reasons why the SNL compression loops use radial compressors. Even though the average density changes in the compressor are not large, it is recognized that entering the dome will result in phase changes that may cause unanticipated behavior. One goal of the test-loop is to have sufficient control of the compressor inlet temperature and inlet pressure to avoid entering the liquid-vapor dome or to purposely enter it, when desired. This will be done primarily by controlling the CO_2 inventory in the loop and by controlling the compressor inlet temperature. Some tests were intentionally operated in the two phase region and the results are described later in this report.

The Sandia S-CO_2 compression loop is being fabricated with an inventory control system that can vary the fill gas pressure so that a relatively larger range of compressor inlet pressures (5.0-9.2 MPa) can be explored. We will fill the loop from a series of gas bottles connected through a booster pump. Solenoid valves will be used to bleed gas into or from the loop to control the fill inventory. The control points 3 & 4 (see red numbers in Figure 2-2) indicate the fill and bleed control points.

Two mechanisms are used to control the compressor inlet temperature that we wish to vary from 290-318K. One is the speed at which the cooling water flows (control point 5 in Figure 2-2), and the second is the recirculation of warm water through the water control valve 6. In addition a heater to preheat the water has only been recently added to the loop. It has not been fully tested yet. It will be used to coarsely control the feed water temperature from the evaporator cooler. As already indicated, we expect that small changes in CO_2 temperature will require large changes in heat removal capability.
Heat removal and temperature control is further complicated by the fact that at Sandia the waste heat removal system uses a large evaporative cooler, with a large amount of coolant volume (400 gallons) at

relatively high flow rate of 260 gpm. We will also have large winter to summer feed water temperature variations (~278-298 K).

The combination of the variations in the feed-water pump flow rate and recirculation of the warm water will reduce the time it takes to reach a specified compressor inlet temperature, and will also allow for operations over a wide range of wet bulb temperatures throughout the year. To measure the fluid temperatures (water and CO_2) we will primarily use Resistance Thermometry Devices (RTD's) which have an accuracy of ~0.2 K. However, heat transfer down the length of the RTD electrode may significantly affect the accuracy of the temperature measurement when they are inserted, especially in the smaller 38-50mm ID ducting.

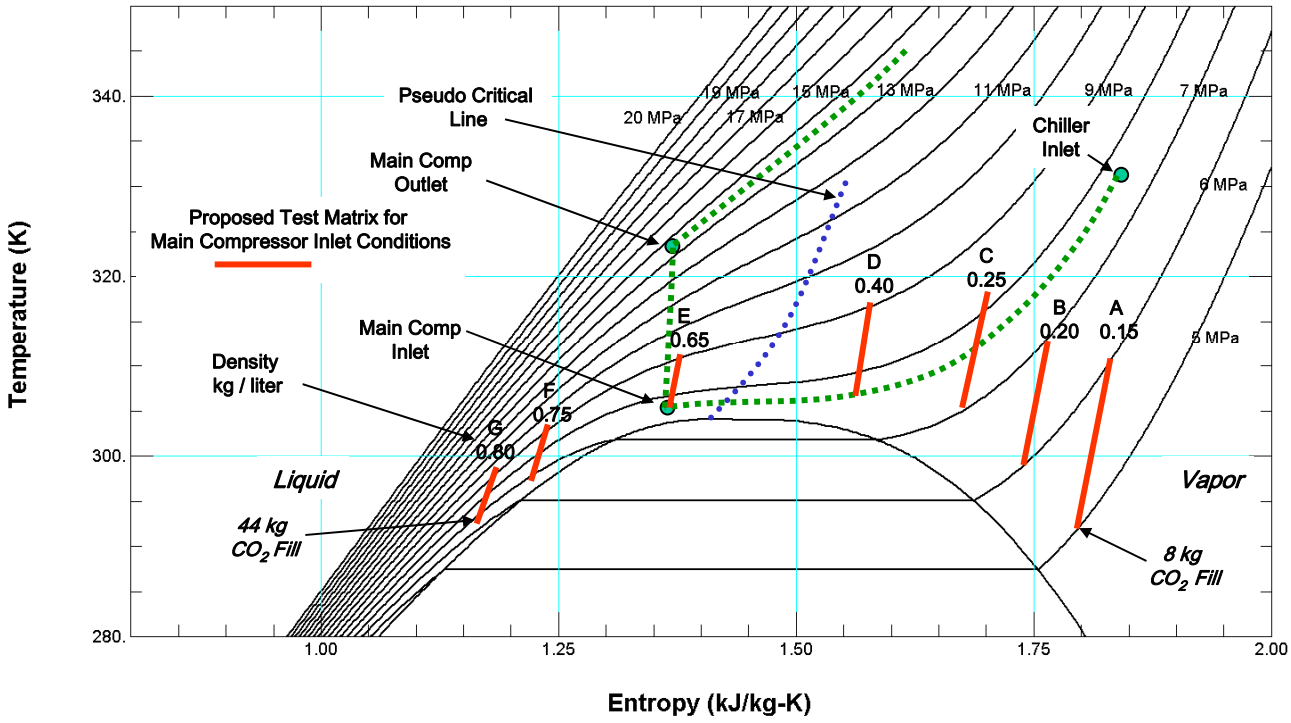

Figure 2-9: Temperature entropy diagram for CO_2 near the critical point. The green curves indicate the T-S path for CO_2 flow in the gas chiller, in the compressor, and during heating in either the recuperator or a heater. The red lines show the range of compressor inlet conditions that we intent to operate the loop at. Note that the test lines roughly follow the lines on constant density, and they vary from a low density of 0.15 kg/liter to a high of 0.80 kg/liter over a temperature range from 290 K to 318 K. The blue dotted line shows the pseudo-critical points where large peaks in the heat capacity and viscosity are observed.

2.3.1 Thermodynamic cycle analysis of the compression loop

Sandia's supercritical CO_2 cycle analysis tools were used to evaluate the operation of the S-CO_2 compressor for various compressor inlet temperatures and pressures. For simplicity's sake, we have estimated the compression loop operating conditions at three conditions. One is at or very near the critical point (305.3 K, 7690 kPa), the other is on the liquid side of the saturation curve (295 K , 7690 kPa) and the other is on the vapor side of the dome (295K, 5000 kPa). These operating conditions are approximately indicated by the lower portion of the red lines marked A, E, and F in Figure 2-2.

These conditions are summarized in Table 2.1 which provides the expected behavior of the loop as the compressor inlet conditions vary around the critical point near the top of the liquid-vapor dome. The table lists the state point operating temperatures and pressures at the inlet and outlet of each component in the loop. These state points are indicated by numbers 1-3, where 1 represents the compressor inlet, 2 the compressor outlet, and 3 the exit of the orifice, which is the same as the entrance to the gas pre-cooler (see Figure 2-2). These state point temperatures, pressures, mass flow rates and power are listed in the table for compressor inlet conditions at the design point, on the vapor side of the dome and on the liquid side of the dome with a shaft speed of 75,000 rpm.

The major observations to make are that as one moves the compressor inlet condition from the vapor side of the saturation curve (or dome) to the liquid side of the saturation curve (dome) through the design point, the mass flow rate increases, the pressure ratio increases, the compressor power increases, and the temperature rises decrease. In spite of these large changes, the efficiency of the compressor remains nearly constant. On the liquid side of the dome, the mass flow rate increases over the design point because the more liquid systems have higher fluid densities, and thus more coolant is flowing for the same volumetric flow through the compressor. The larger coolant flow rate also increases the power, the pressure ratios increase because more liquid-like fluids have lower compressibility. The lower compressibility of the more liquid fluids also means a lower temperature rise upon compression than in the more vapor like fluids. The efficiency stays the same, because the mass flow rate in the analysis was adjusted to keep the specific speed of the compressor near its optimum. This requires that the orifice area of the valve changes to provide the flow rate as indicated in this table.

Table 2.1 Expected operating conditions of the S-CO_2 compression test loop at the design point and on the liquid and vapor sides of the dome.

Property	Design Point	Vapor Side	Liquid Side
T1 (K)	305.3	295	295
P1 (kPa)	7690	5000	7690
H1 (kJ/kg)	309.3829231	436.3347377	253.5925441
T2 (K)	324.6590279	316.8887813	306.0362581
P2 (kPa)	13984	6461.477561	14898.44307
H2 (kJ/kg)	324.3133239	450.8616943	267.3396258
T3 (K) Isenthalpic	306.1755619	303.3268813	298.9849653
P3 (kPa)	7766.90	5050	7766.9
H3 (kJ/kg)	324.31	450.8616937	267.3396258
mdot (kg/s)	3.53	1	3.8
Chiller power (kW)	52.70430916	14.52695599	52.23891056
RPM (rev. per min.)	75000	75000	75000
mdotEq (kg/s)	3.5474701	3.785997516	4.31996661
Pressure Ratio	1.818450313	1.292295512	1.937378813
dH.Ideal (kJ/kg)	9.911067497	9.643668505	8.754601852
Efficiency	0.663818019	0.663846444	0.636833477

3 S-CO_2 Turbomachinery and Test-loop Components

3.1 *Turbomachinery*

In the S-CO_2 test loop, the turbomachinery is the key component in the entire loop. For the compression loop, the turbomachinery consists of a permanent magnet motor/alternator, the compressor, the diffuser vanes, the shroud, seals, bearings, and a water cooled housing. Figure 3-1 shows the details of the turbomachine and labels to identify the major components. The major function of the motor compressor is to spin the compressor wheel and thus provide pumping power to the CO_2. Approximately 50 kW of pumping power will be supplied by the motor that will also operate at up to 150 kWe as a permanent magnet generator/alternator. The compressor wheel is designed to spin at 75,000 rpm and pump approximately 3.5 kg/s of supercritical CO_2 at a pressure ratio of 1.8. The compressor inlet pressure is just above the critical pressure and has a fluid density of approximately 57% the density of room temperature water.

To compress gas efficiently, a number of components and design features within the compressor wheel system design must be developed and tested. In addition to the compressor wheel design and its performance modeling, design features must be included to provide seals, bearings, and thrust balance components (pump out vanes or other mechanisms). These components allow the turbomachinery system to reduce windage losses, to reduce the seal leakage flow rates (and thus control auxiliary pumping power) and provide for thrust load balancing. This section of the report first describes the compressor wheel and its expected performance characteristics. Later sections describes the analysis and measured results for the leakage and windage loss mechanisms, as well as brief discussions on rotor dynamics and thrust load balancing design features.

The overall design performance characteristics of the turbomachinery are provided in Table 3.1. Because the design for the turbomachinery is modular, it has been possible to replace compressor and turbine wheels, shrouds, bearing assemblies, and seals when modifications to the design were required. The rotor is also modular, and it uses a tie bolt to hold the rotor assembly together. For example, in the compression loop the initial journal bearings used ball bearings with substantial thrust load capabilities. Once the thrust loads were balanced, the journal ball bearings were replaced with gas-foil thrust and journal bearings. This modularity means that it is relatively easy to change components, or make changes to the designs. However, even though the design is flexible, it is still a complicated piece of machinery and requires several days to fully disassemble the turbomachinery and reassemble it with the proper pre-loaded stress on the fastening bolts.

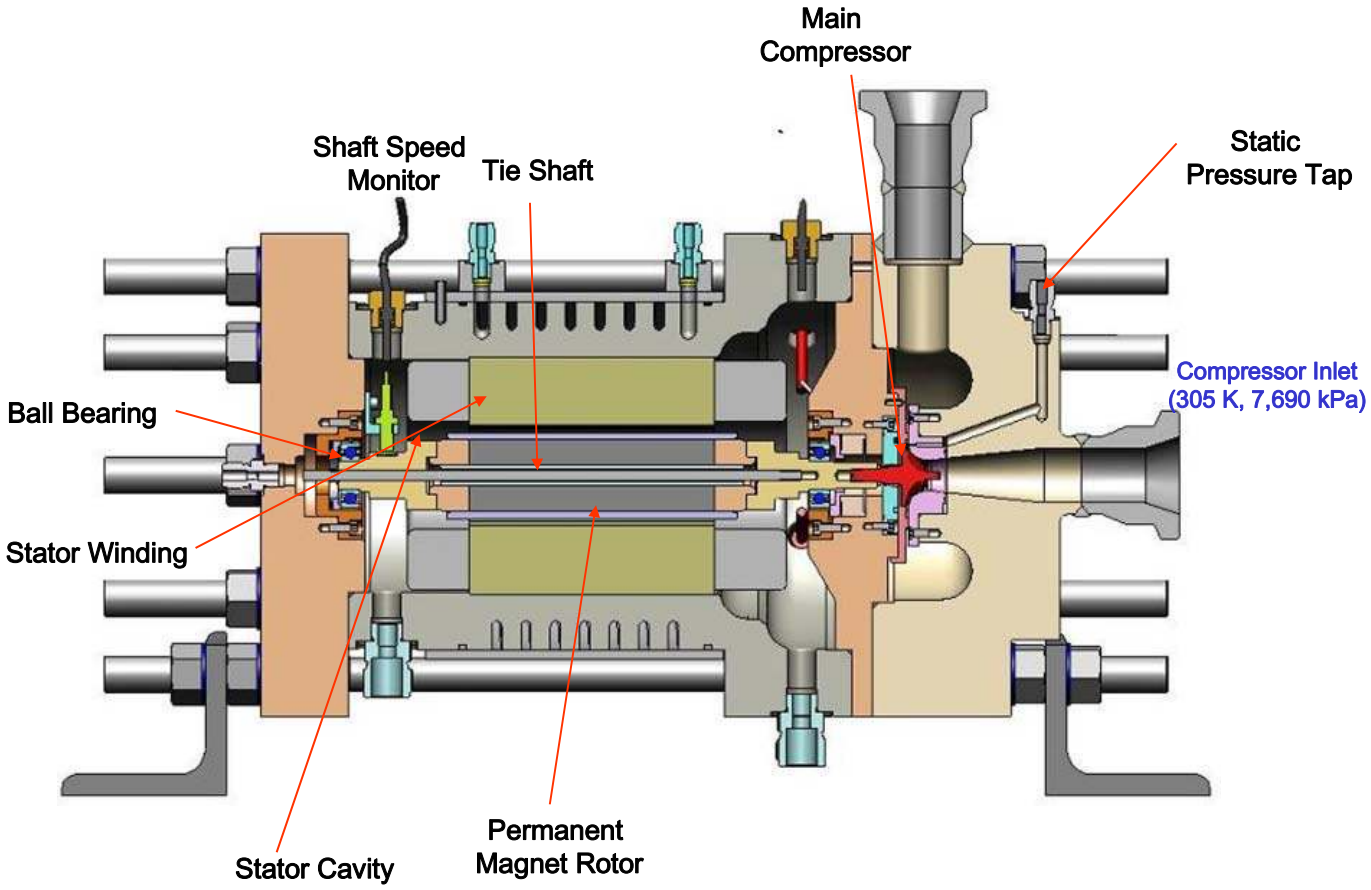

Figure 3-1: Detailed engineering drawing of the motor-driven compressor for the S-CO_2 compression loop. The slots in the housing provide water cooling capability.

Table 3.1 Summary of turbomachinery design and performance characteristics for the S-CO_2 compression loop.

Design Characteristic	Value	Design Characteristic	Value
Max Motor Power	50 kWe	Flow Rate	3.53 kg/s
Max Alternator Pwr	120-150 kWe	Pressure Ratio	1.8
Design Speed	75,000 rpm	Permanent Magnet	Sm-Co
Maximum Speed	80,000 rpm	PM cladding	Inconel
Housing MAWP	2600 psia	Stator	Uncanned
Housing HydroTests	3300 psia	Compressor Eff.	~66% (total – static)
Rotor Cavity Pressure	~150- 200 psia		

Figure 3-2 shows a photo of the manufactured compressor wheel (1.47" OD) including the blank from which the wheel was machined. The wheel and its detailed design were developed by Sandia's contractor Barber Nichols using a variety of existing in-house tools and codes.

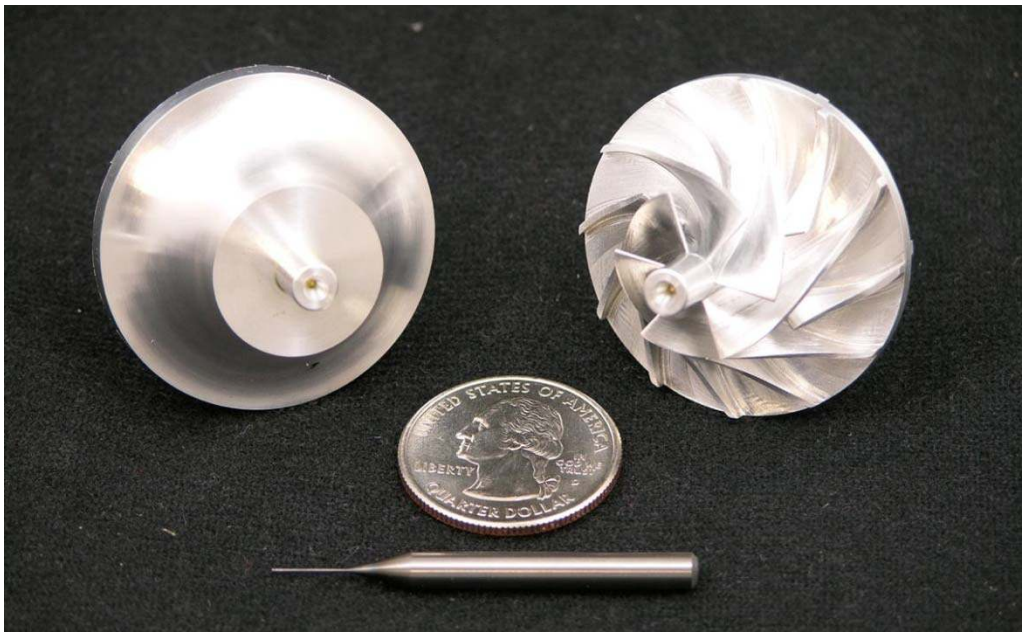

Figure 3-2: Nine S-CO_2 compressor wheels have been fabricated. This image shows the compressor wheel blank, the finished wheel, and one of the tools (not the smallest) used to machine the wheel.

3.1.1 Rotor Cavity

Figure 3-3 shows a detailed engineering drawing of the rotor, bearings, labyrinth seals, and compressor wheel. Frictional losses on the rotor are expected because the rotor is spinning at 75,000 rpm within the high density CO_2 fluid. At the compressor inlet design temperature (305.3 K) and pressure (7687 kPa), the fluid has a density that is approximately 57% the density of water. At these very high shaft speeds and in this very dense fluid, substantial losses are expected. To keep the rotor windage losses manageable, the rotor cavity pressure must be reduced. The initial design sets a goal of 200 psia for the rotor cavity. Seals and separate pumps are required to lower the rotor cavity pressure For simplicity and cost reasons we initially selected labyrinth seals, and the use of Haskel gas booster pumps to lower the cavity pressure. The labyrinth seal is illustrated in Figure 3-4 A and B. The labyrinth seal uses four teeth that closely approach staggered steps in the compressor shaft to limit the flow through the seal. In the S-CO_2 turbomachinery, the design clearance between the teeth and the root of the shaft is 0.0015".

Technologies other than stepped labyrinth seals were also considered and tested. Dry-liftoff seals, which will likely have about one order of magnitude less leakage than the labyrinth seals, are the preferred choice. However, commercially available dry-liftoff seals are much more expensive, relatively large compared to the shaft diameters being used in these designs, and do not normally operate at the high shaft speed that we are using in the turbomachinery. Thus, their use would require more development than labyrinth seals. Fortunately, because the turbomachinery uses a modular design it can easily be modified to add in components that would allow for the inclusion of dry-liftoff seals at a later date. Overall, it appears that the leakage flow rate through the labyrinth seals is on the order of 1-2% of the total mass flow rate per seal.

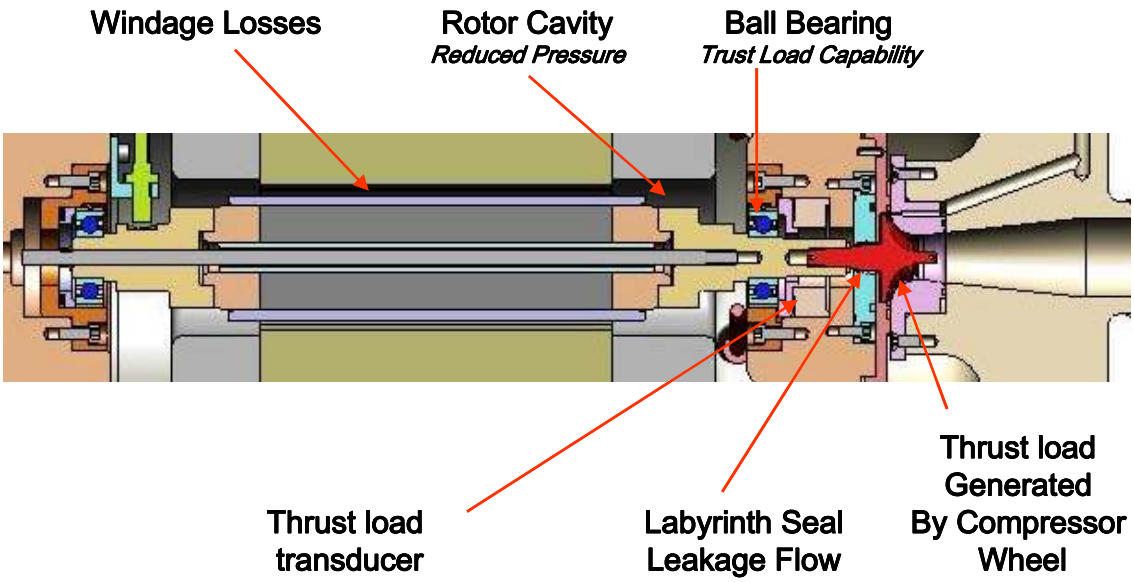

Figure 3-3: Issues associated with the PM rotor windage losses, ball bearing thrust capability, labyrinth seal leakage, and pump-out vanes on the compressor wheel are required for thrust balancing.

The Haskel 8AGD-5 gas booster pumps that are used to reduce the cavity pressure are shown in Figure 3-5. These pumps use compressed air to reduce the rotor cavity pressure and then discharge the compressed CO_2 back into the loop. The pumps are also water cooled, which will help lower the pumping power required to operate these pumps. The pumping power is determined by the leakage mass flow rate multiplied by the change in enthalpy required to pump the fluid from ~200 psia to the return pressure which is approximately 1120 psia. Of course this enthalpy change depends on the inlet temperature to the Haskel pump and the pump efficiency. The maximum Haskel pump inlet temperature is estimated to be 320 K, but could be substantially different depending on the amount of cooling provided to the housing and whether or not the rotor cavity is heated by magnetic losses. For the purposes of determining the Haskel pump pumping power, the pump inlet temperature is bounded by the lowest inlet temperature available which is 295 K (approximately the cooling water inlet T) and by our estimate for the highest temperature which is 320 K. The pump efficiency is estimated to be 85%.

The S-CO_2 loop utilizes two types of Haskel pumps during fill and operation. The pump used to fill the loop is an ALG-15 air driven liquid pump. This pump is operated with compressed air and is water cooled. The maximum allowable working pressure for this pump is 2500 psig. The loop also uses two 8AGD-5 Haskel pumps to pull down the rotor cavity pressure and return this gas to loop pressure downstream of the compressor. These pumps are also air driven and air cooled. Their maximum allowable working pressure is 2500 psig.

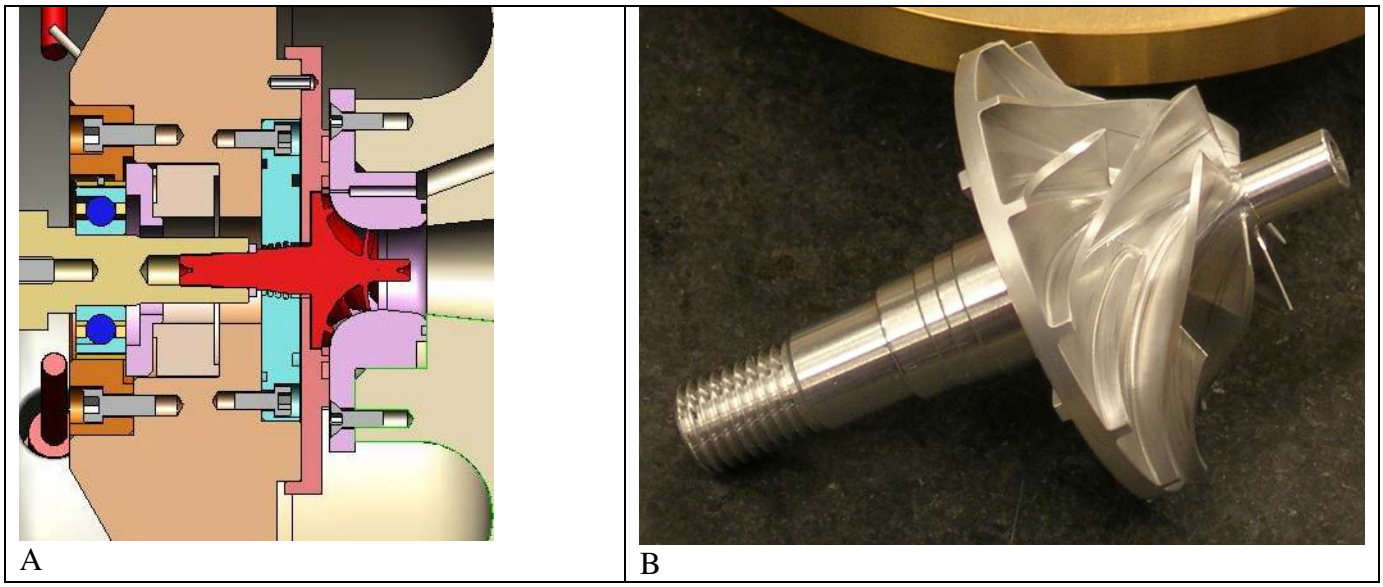

A B

Figure 3-4: The left image shows an engineering blow up of labyrinth seal. The light blue ring in made of brass and has four teeth that approach the steps on the rotating shaft. The right image shows a photo of the compressor wheel and the four steps on the shaft.

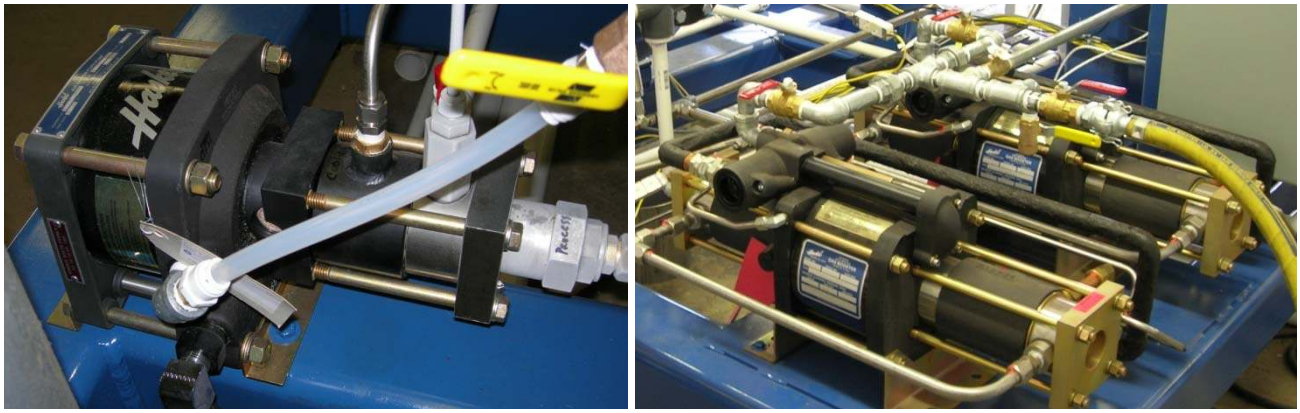

Figure 3-5: Pictures of the Haskel pumps on the SCO_2 loop.

3.1.2 Stress Analysis of Turbomachinery Housing

The S-CO_2 Brayton loop contains a few custom-built components, all of which are contained within the TAC unit pictured in Figure 3-6. Each of these custom components was analyzed with multiple methods to determine their maximum allowable working pressure (MAWP). First, simple hand calculations were performed by SNL to verify the basic design. Next, more detailed analyses were generated by Barber-Nichols. Finally, these analyses were verified by performing a detailed Finite Element Analysis (FEA) of each component for preload, shutdown, operating, and hydrostatic test scenarios. The results of each of these analyses for each custom component of the turbo-machinery, including the bolts, are found in the Pressure Safety Data Package.

The engineering drawing in Figure 3-7 is an example of the FEA results generated by SNL. Good agreement was seen between the Barber-Nichols and SNL FEA analyses. After construction, these components were assembled and hydro tested to 3300 psig. In order to maintain pressure, the bolts on

this pressure vessel must be pre-stressed. The turbine end plate was shown to have the lowest safety factor during operation, with a value of 3.6. All components were made from SS-304, except for the bolts, which are made with In-718.

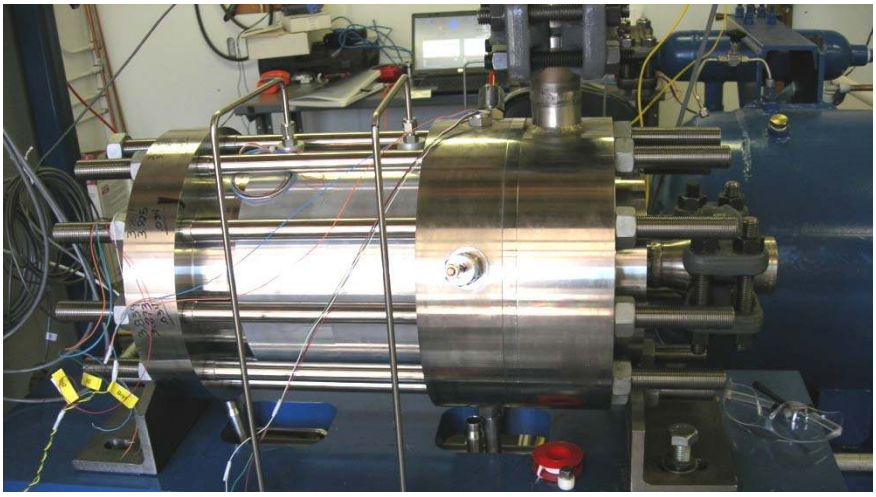

Figure 3-6: Photograph of Turbine-Alternator-Compressor assembly

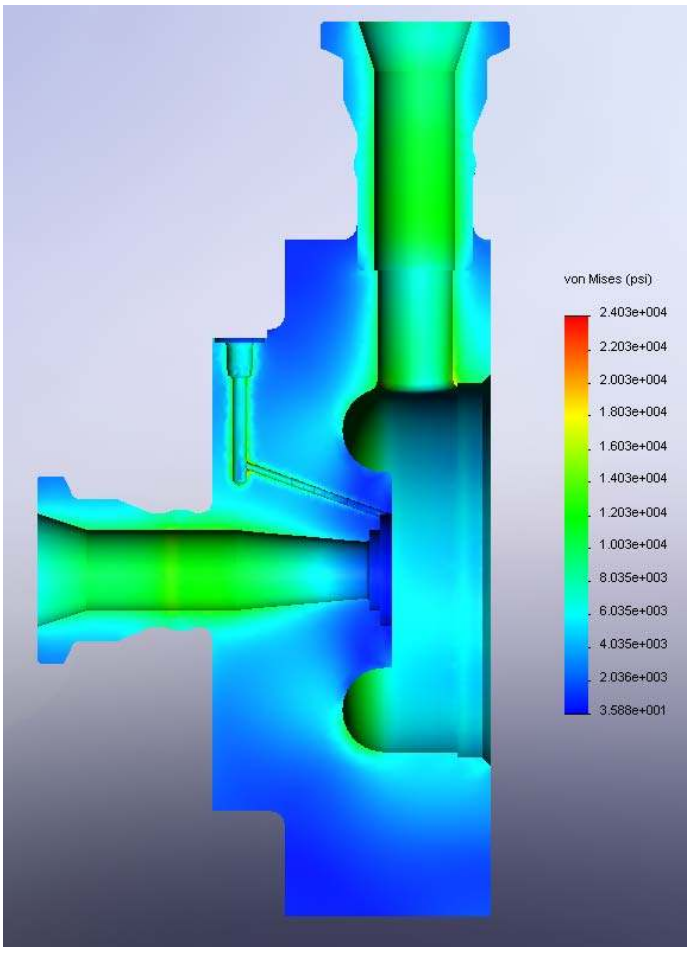

Figure 3-7: Finite Element Analysis results for the TAC turbine end plate

3.2 *Gas Chiller*

A small-scale tube and shell-like heat exchanger was designed and developed by BNI to support the smaller scale tests. This gas chiller is designed to reject ~50 kW at 30 gpm flow rate of water at ~76°F for a CO_2 exit temperature of 305.3 K at a mass flow rate of 3.5 kg/s . More heat can be rejected at larger flow rates or lower cooling water inlet temperatures. The spiral tube and shell like S-CO_2 gas chiller is illustrated in Figure 3-8, which shows the chiller with the outer shell removed. The two colors of the spiraled tubing contain the S-CO_2 fluid, while the cooling water flows in the annular passages between the two tubes. The general design description of the small pre-cooler is given in Table 3.2. Actual photos of the small pre-cooler during construction and installation in the compression loop are shown in Figure 3-9.

Table 3.2: General description and design of the coiled tube-and-shell like gas chiller.

Property Description	**Value**
Tube Diameter (OD)	.0381 m
Tube Wall thickness	0.0024 m
Length of a single Coiled Tube	19.15 m
Pitch of Coils	0.1016 m
Area of Gas / Liquid Heat Transfer	4.00 m^2 / 4.58 m^2
Hydraulic Diameter of Gas / Liquid	0.00333 m / 0.0144 m

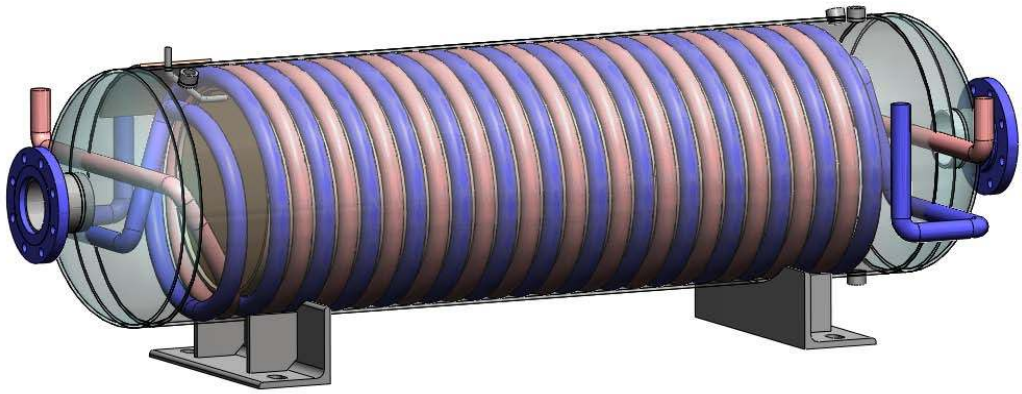

Figure 3-8: Engineering drawing of the compressor loop showing the ~50 kW gas chiller with the outer water housing jacket removed to show the S-CO_2 spiral cooling lines.

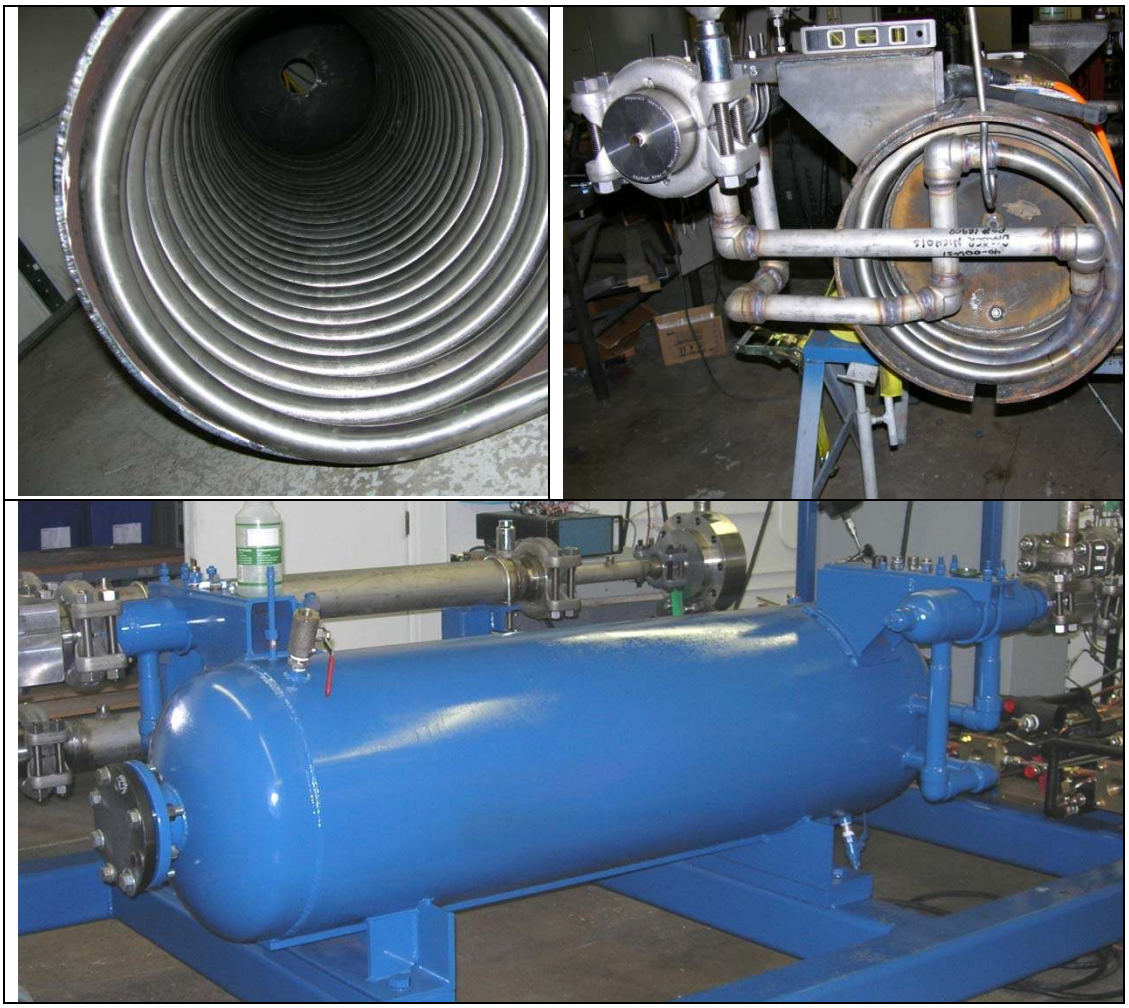

Figure 3-9: Photos of the small BNI fabricated gas chiller. The top photos show the CO_2 tubes coiled inside the water jacket and end fittings. The bottom figure shows the completed gas chiller installed on the compression loop skid.

3.2.1 Analysis and Modeling of the Gas Pre-cooler

The gas pre-cooler was modeled using an updated version of the SNL Reactor Power and Control SIMulation code (RPCSIM) (Figure 3-10) and the **T**RAC/**R**ELAP **A**dvanced **C**omputational **E**ngine (TRACE) (Figure 3-11). The original version of RPCSIM was described in Wright and Lipinski (Wright, 2006), however it has been modified to use the National Institute of Standards and Technology (NIST) Reference Fluid Thermodynamic and Transport Properties database (Refprop) and to use an enthalpy based solution method. This code was developed to help support SNL in operating and running the loop. It contains a number of simplifying assumptions (mass flow is constant around the loop, and compressible flow only is allowed in the compressor, turbine, and flow valve orifice. This makes the code fast running. The code is written in SIMULINK, (Mathworks, 2008) and uses the NIST Refprop 7 or 8 data base. The code is easy to use and modify. A component model can easily run faster than in real time, however, models that must operate as a loop make take as much as ½ hour to run a 200 second transient problem.

TRACE is a modernized thermal-hydraulics code designed to consolidate the capabilities of Nuclear Regulatory Commission's (NRC) 3 legacy safety codes - TRAC-P, TRAC-B and RELAP. It is able to

analyze large/small break Loss of Coolant Accidents (LOCA) and system transients in both Pressurized Water Reactors (PWR) and Boiling Water Reactors (BWR). The capability also exists to model thermal hydraulic phenomena in both 1-D and 3-D space. This code is much more sophisticated than RPCSIM, but it is relatively difficult to use and requires much longer run times.

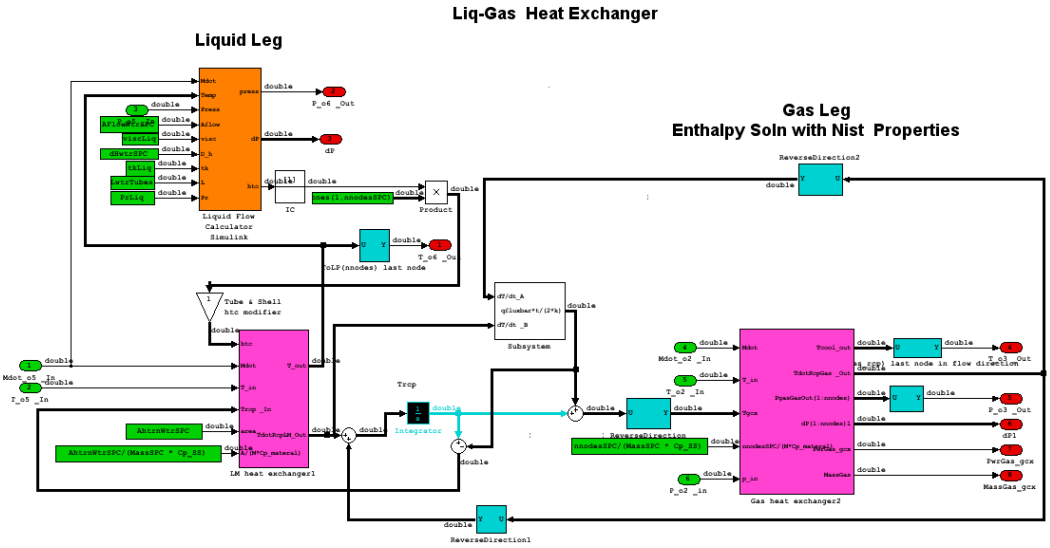

Figure 3-10: RPCSIM model of the gas chiller. The orange module calculates pressure drop and the heat transfer coefficient in the water leg. The pink module on the left calculates water temperature increase. The pink module on the right calculates heat transfer, pressure drop, and temperature change for the S-CO_2 leg.

The TRACE and RPCSIM codes were both used to model the gas chiller of the Sandia S-CO_2 compression loop. Both codes modeled the gas chiller as a counter flow heat exchangers and divided the S-CO_2 and water flow channels into 80 cells. The temperatures of these cells are plotted in Figure 3-12. A comparison of the initial results of the two codes are in very good agreement (<1 K difference). A closer examination of the input data for these two models reveals two small differences that are the likely cause for the observed temperature differences. First, the TRACE model has not yet been updated to reflect the as-built specifications of the gas chiller. This has led to small geometric differences in the models which will be corrected soon. The second more likely source of error is the thermal hydraulic properties that were used for the water mix. RPCSIM uses actual data for a 25% mixture of propylene glycol with water, while TRACE uses properties for pure water.

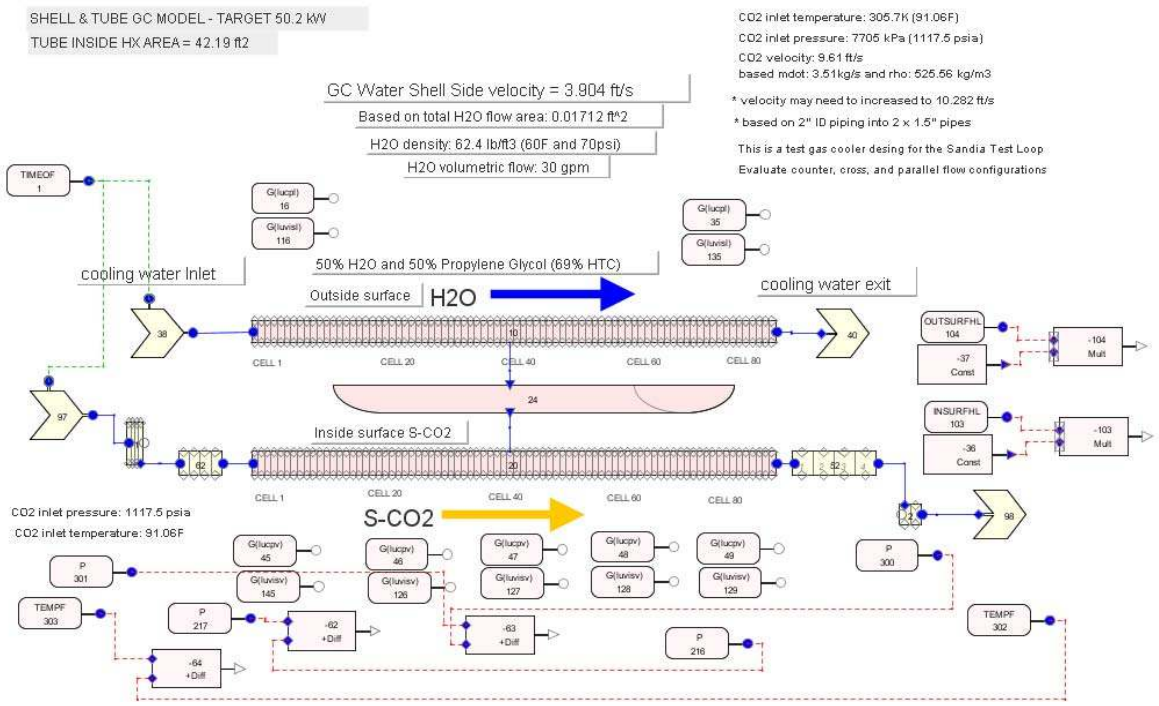

Figure 3-11: TRACE model of the gas chiller. The CO_2 and water flow paths are represented by nodalized pipes. These pipes are connected by a heat structure.

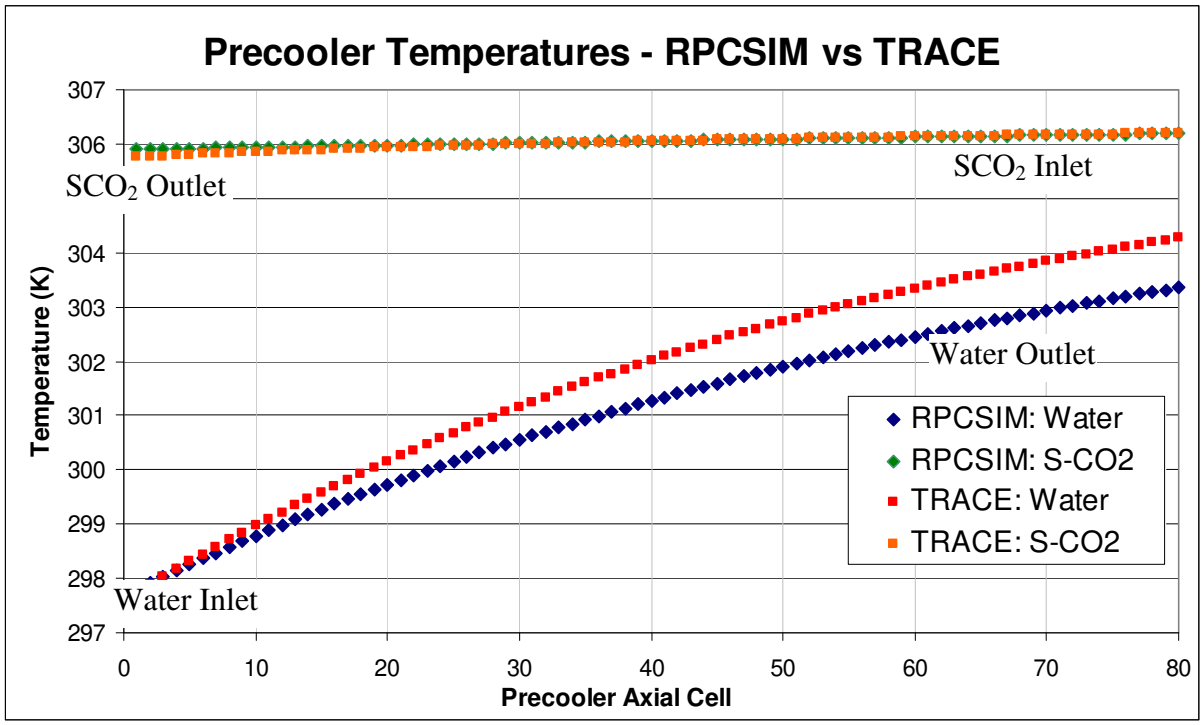

Figure 3-12: Predicted S-CO_2 and water temperatures within the SNL gas chiller. These temperatures were calculated using both the RPCSIM and TRACE codes.

3.3 *Watlow Heaters*

SNL and BNI have purchased commercially available immersion heaters from Watlow (Watlow, 2008). While these heaters are not included in the compression loop, they are built into the full Brayton loop discussed at the end of this report. These heaters provide 130 kW of electrical heating power per heater. Each heater also includes a heater controller. These controllers use Silicon Controlled Rectifier (SCR) switches to provide continuous control from 0 kWe to 130 kWe, using a 4-20 mA control signal. The design specs for these heaters are provided in Figure 3-13. The heaters are American Society of Mechanical Engineers (ASME) stamped and can operate at up to 1000°F = 810 K at 2585 psia. The Watlow heaters did not include the shells into which the immersion heaters need to be placed. SNL and BNI contracted Merrick Corporation to provide an ASME design for these heater shells. A contract was awarded to Springs, Inc to fabricate and ASME stamp the shells, which are designed to operate up to 2600 psia at 1000°F. Figure 3-14 shows a line drawing design for the heater shell.

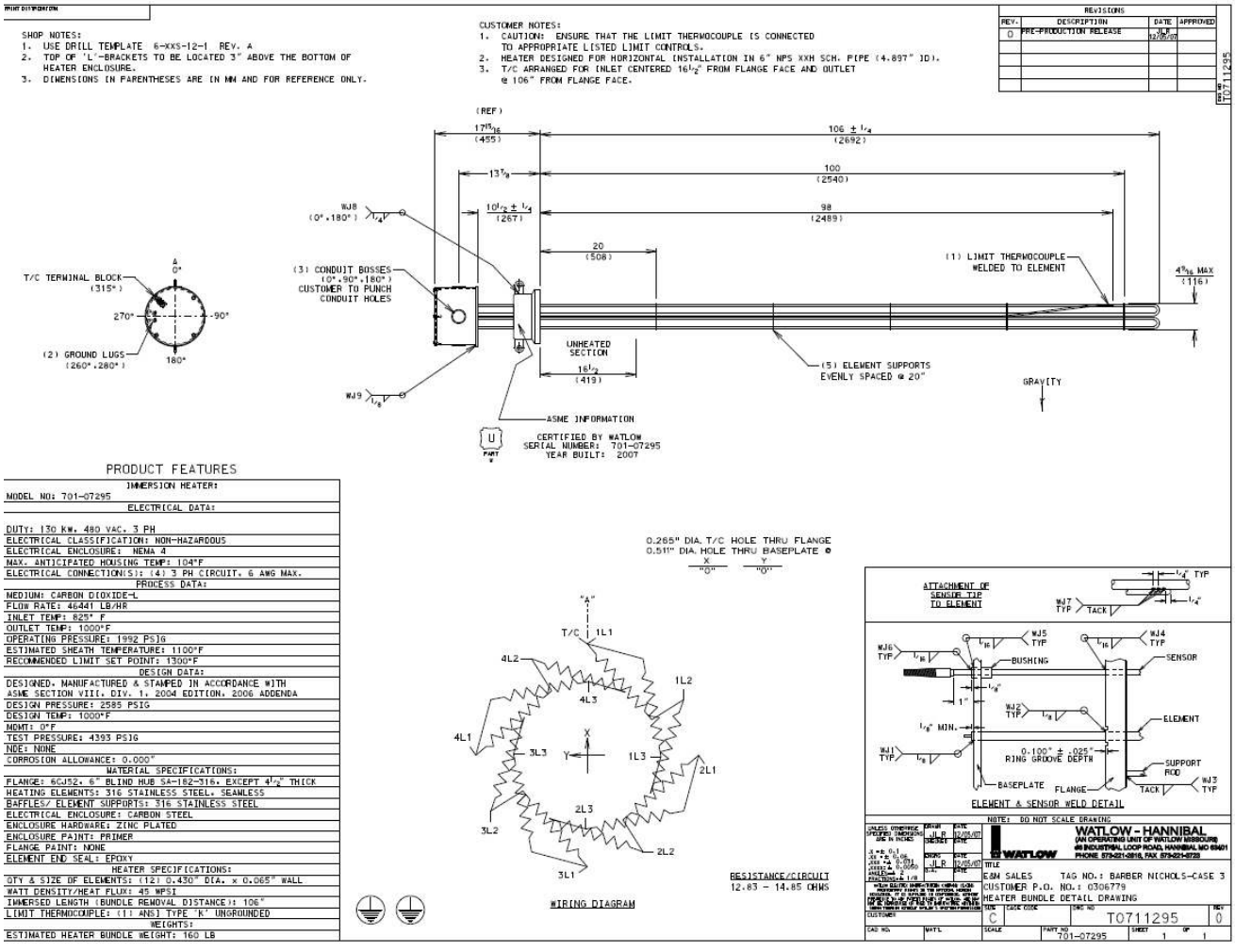

Figure 3-13: Watlow 130 kWe immersion heater design.

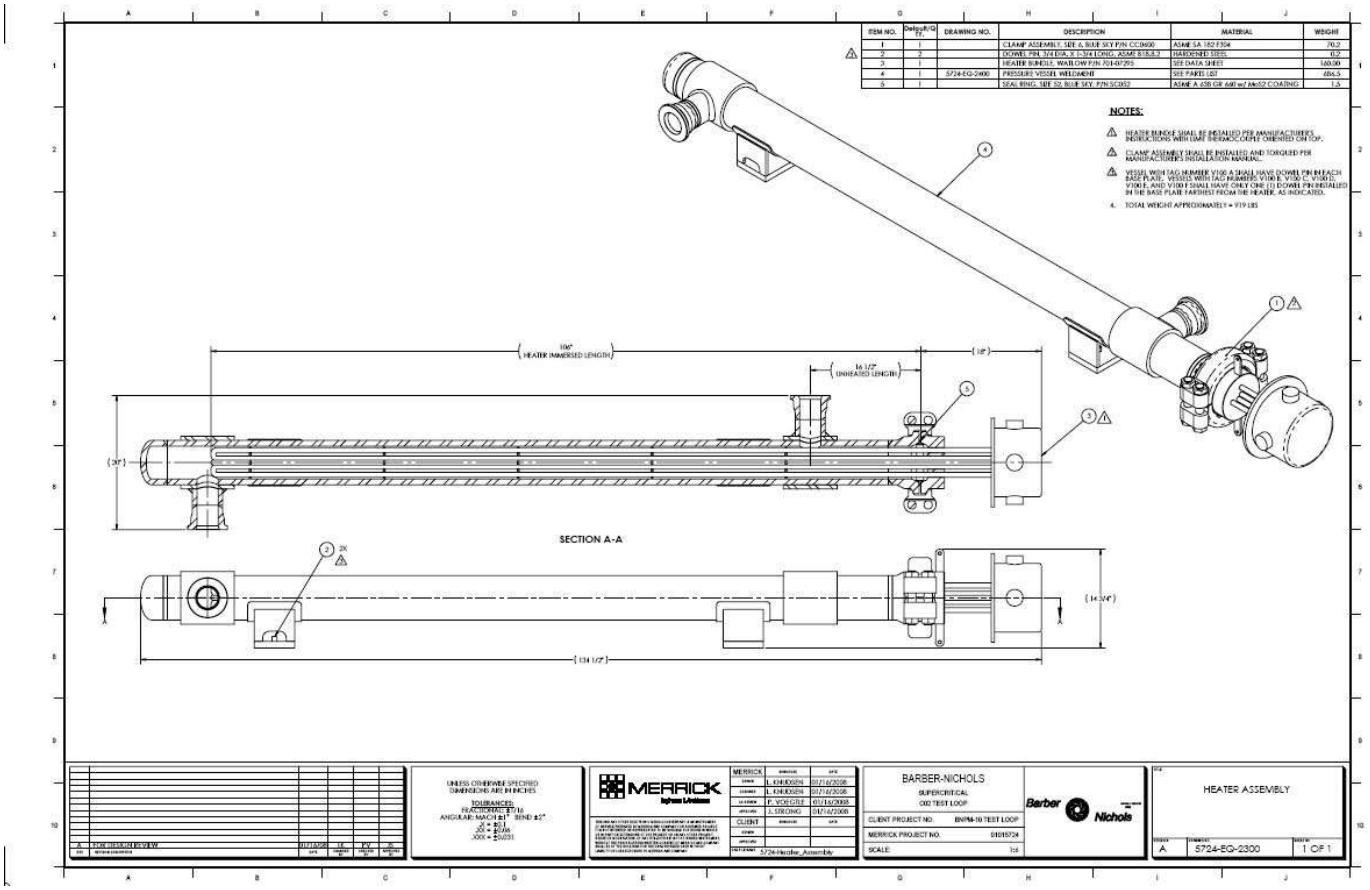

Figure 3-14: ASME stamped heater shell designed to operate at 1000° F (810 K) ~ 2600 psia.

3.4 *Motor Alternator and Controller*

Because the stator will be immersed in supercritical CO_2 fluid, the electrical windings and insulation will be exposed to this fluid. There is some concern that over time, the supercritical CO_2 will damage the insulation on the stator. Figure 3-15 shows a photo of the stator. At Sandia, we have used an autoclave to perform some screening tests that lasted up to two weeks and in some longer term tests that lasted several months to examine the compatibility of the stator with the S-CO_2.

In the screening tests, SNL placed a motor/alternator stator in a CO_2 autoclave. The stator was kept at 1700 psi for 2 days, and then depressurized in ½ hour. This cycle was repeated for 2 weeks. Resistance and weight change measurements were made. We observed minor weight reductions (< 1 gm) and reductions in elasticity of the lead wires. For the resistance measurements, no degradation in resistance was observed using a 1000 V at 1000 Mohm meter.

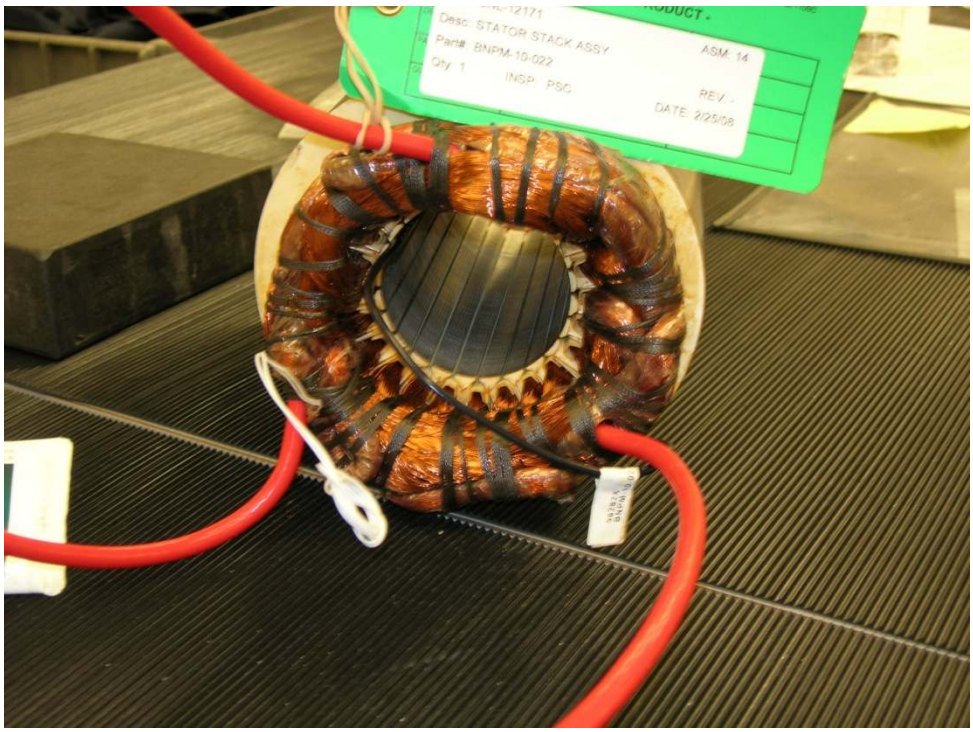

Figure 3-15: Photo of the PM stator for the supercritical CO_2 compression loop.

For the long term tests, SNL modified the autoclave to include electrical feed throughs in the lid of the pressure vessel. This then allowed SNL to check for electrical resistance changes to the stator over a long period of time. The tests results have shown that over a period of over 3 months, there have been no measurable resistance changes to the stator windings. These tests have currently been stopped, and SNL will use the electrical meter to observe the behavior in the actual stator.

The motor/alternator controller is shown in Figure 3-16. This device has operated the motor at power levels approaching 50 kWe and at speeds up to 65,000 rpm. The hardware was designed to motor at 50 kW and produce up to 150 kWe as an alternator. It uses some commercial switching circuits to drive the three phase motor or to load the alternator. The switching circuitry uses IGBT transistors, and pulse width modulation to drive the motor. The motor/generator needs a zero crossing signal to tell the circuit when to reverse the polarity of the voltage that is applied to the stator. This sensor was originally intended to be a speed proximity sensor, but this device did not work well as it was noisy. Instead a simple coil that was imbedded in the stator was used as the speed sensor. The operation of this variable speed motor controller has taken considerable time to work through a number of issues such as how to start the motor, especially on gas foil bearings, how to keep the speed sensor free from noise, when to shift to speed control, and how to deal with internally sensed faults such as over temp or sensed shorts. The motor controller has sensed two faults in the electrical feed throughs. These have sense been replaced with higher voltage capable feed throughs.

Figure 3-16: Motor alternator controller.

3.5 *Instrumentation*

To measure the fluid temperatures (water and CO_2), we use Resistance Thermometry Devices (RTD's) which have an accuracy of ~0.2 K and thermocouples which have an accuracy of ~1 K. These devices will be placed in the CO_2 at the inlet and exit of every device. Pressure transducers will also be used to monitor the pressure at the inlet and outlet of every component. There is also an orifice flow meter that is located after the compressor outlet. We have also purchased a Coriolis flow meter to measure the mass flow rate and CO_2 density. Two brands of Coriolis flow meters are found in the S-CO_2 loop; Micro Motion and Endress+Hauser. The Micro Motion flow meter has a maximum operating pressure of 4790 psig and is located at the compressor inlet, while the Endress+Hauser flow meter has a maximum operating pressure of 5000 psig and is located at the outlet of the Haskel pumps. Specification sheets and photographs for each of these meters can be found in the pressure data package.

3.6 *Control System*

A data acquisition and control system was assembled to monitor and control all of the state variables and status of the control mechanisms. This data acquisition system was installed by Sandia's Instrumentation and Control Contractor, Prime Core (PrimeCore, 2008) and is being used to monitor the system state variables during the commissioning tests. The control system was also connected to the Labview

(National Instruments, 2008) data acquisition and control system. The control system will use a variety of controllers (on-off or Proportional-Integral-Derivative [PID] control loops) to control the three major control mechanisms which include the fill inventory, the cooling water flow rate, and the warm water re-circulation fraction. The control system was described in the previous quarterly report. The new upgrades include the use of three new displays. The first two show the T-S diagram and the T-density diagrams near the saturation dome with the currently measured state points shown on the plot.

Figure 3-17 shows an image of the front panel on the control system. The top part of the screen shows a simple flow diagram of the loop with the temperature and pressure state points displayed real time on the display. The controls to the right control the water flow control valve which will be used to control the compressor inlet temperature. These controls also control the main - flow valve and have digital controls and set points for other systems that are currently not being used. The lower portion of the plot controls the shaft speed, heater power (if available) emergency shutdown and data file naming and storage. Figure 3-18 shows the compression loop control but with a real time display of the T-S diagram and the T-D (temperature – density) diagram. The state points for the compressor inlet, outlet, and gas chiller are plotted on this curve to visually illustrate to the operator exactly where on the T-S diagram the loop is operating with respect to the critical point. This display tab is illustrated in Figure 3-18. Another tab on the control system shows the compressor map and the location of the compressor inlet for the past 100 recorded time steps. To display this map, the data acquisition and control system must calculate the corrected enthalpy for every time point, which is done every time step. The sampling time is about 4 samples per second.

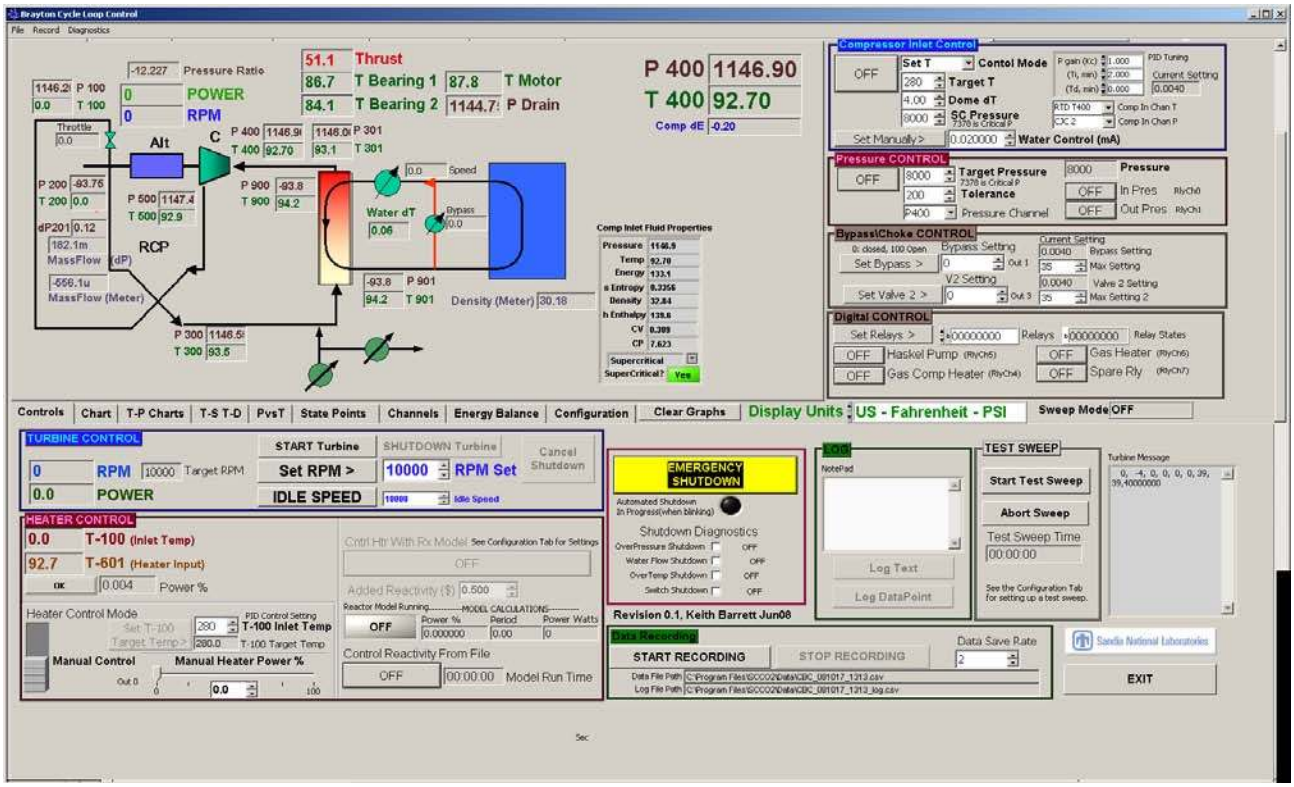

Figure 3-17: SNL supercritical CO_2 data acquisition and control system. The control system allows for the monitoring of the state points in the loop, compressor speed control, heater control, compressor inlet temperature and pressure control, inventory fill control, recirculation and orifice flow control, a reactor simulator, emergency shutdown capabilities, and file name control.

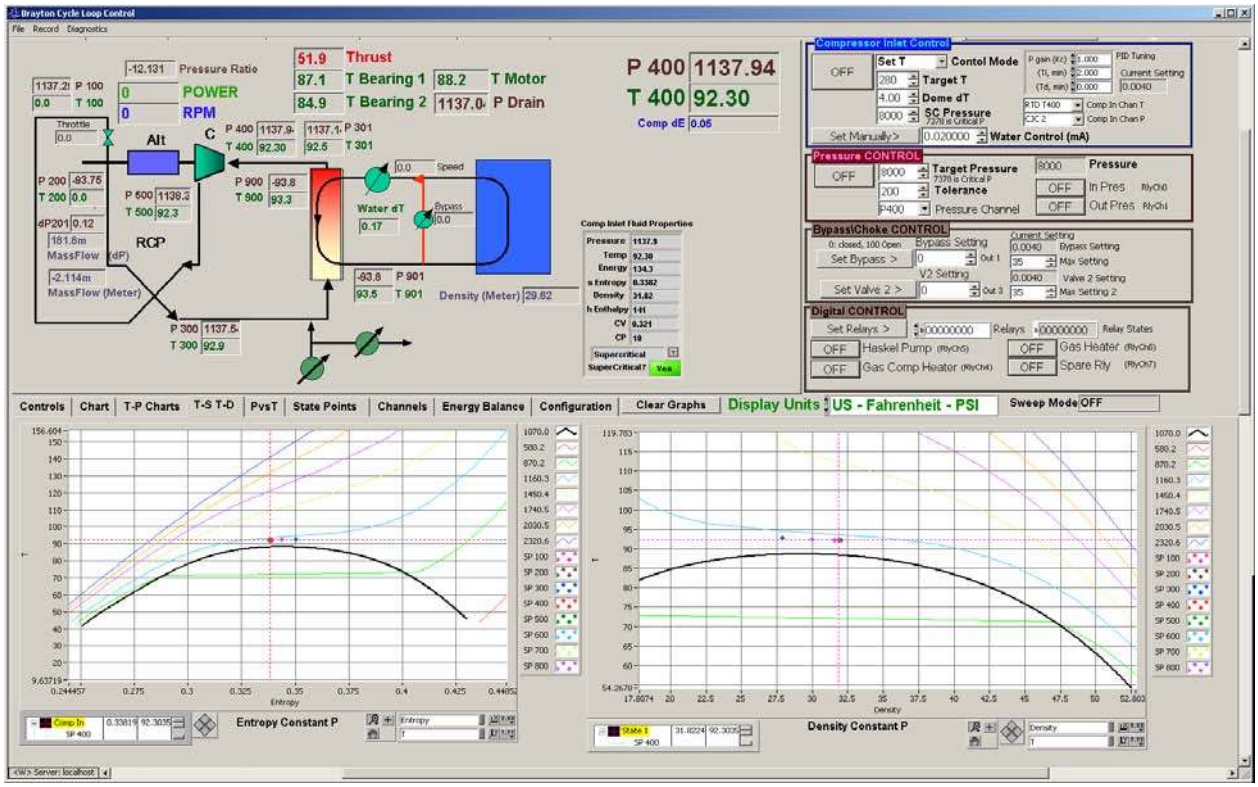

Figure 3-18: SNL supercritical CO_2 data acquisition and control system displaying the T-S and T-D state diagrams. The image on the lower left shows the T-S diagram and that the compressor inlet is very near the critical point. The display on the right shows a similar plot but shows the Temperature-Density (T-D) diagram. The black line is the saturation curve.

4 System Analysis of the Compression Loop

A complete dynamic system model for the S-CO_2 compression loop was developed in Sandia's RPCSIM code. A portion of this code was briefly discussed earlier. The block diagram model for the loop is illustrated in Figure 4-1, and each major block represents a component in the loop. The major components in the S-CO_2 loop include the compressor model, the orifice model, the inventory control model, and the gas chiller model. The gas chiller hardware and the results of the RPCSIM model were described earlier in this paper. In addition, the system model also includes the water side of the cooling loop including ducting.

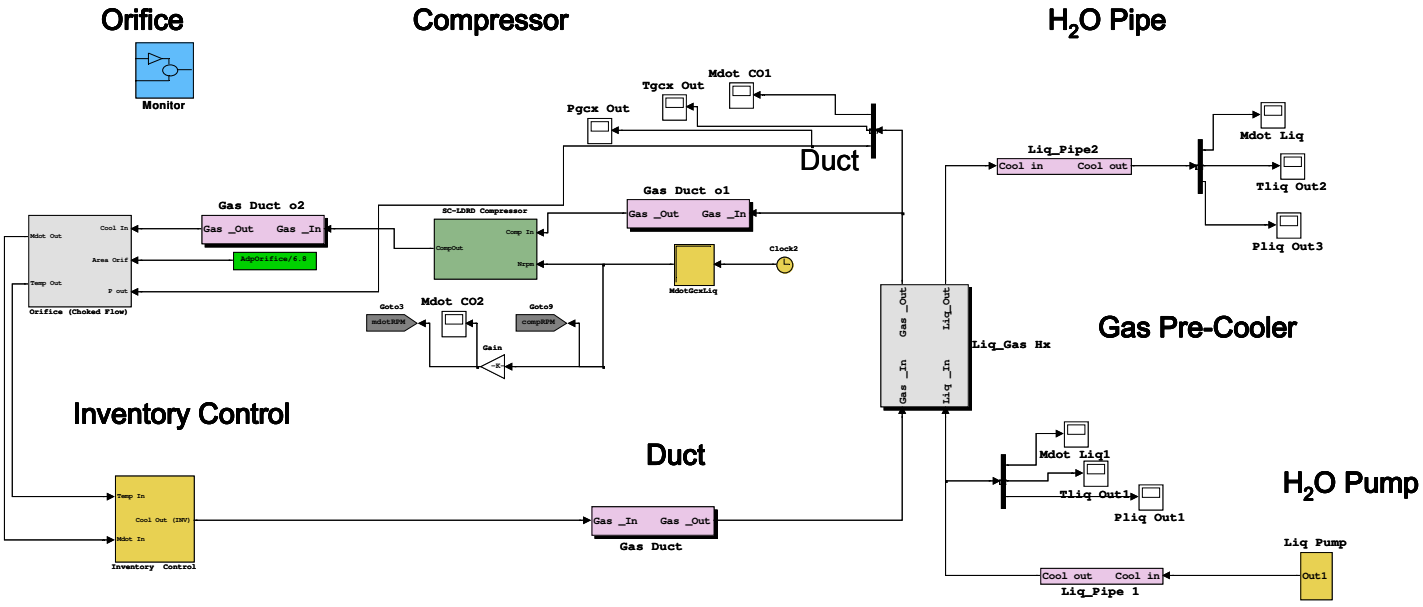

Figure 4-1: RPCSIM (Reactor Power and Control SIMulator) for the Sandia supercritical compression loop. This figure shows the SIMULINK modules that are used to model the compression loop. The model uses the NIST Refprop equation of state for supercritical CO_2 and it uses and enthalpy based non-linear solution technique to model the full dynamic system, including startup.

4.1 *Compressor Model Description*

The compressor model used an older version of the mean-line flow analysis compressor performance prediction tool as described earlier in this paper for its off-normal performance maps. This required multi-dimension look up tables (4D tables) for compressor inlet temperature, pressure, mass flow rate, and shaft speed. The inlet temperature could be varied from 307-313 K, the pressure could be varied from 7600 -9200 kPa. The mass flow rate and shaft speed could be varied from 0.01 kg/s and 100 rpm to 80,000 rpm. The look up tables interpolated between these inlet parameters to determine the outlet temperature and pressure. This approach worked reasonably well, provided the data stayed within the stated range, but it was very labor intensive to generate the 4D maps. At the current time, RPCSIM now uses fits to represent the performance maps of the compressor. These fits are a little easier to use, but

difficulties arise during startup when the compressor or turbine is far from the design point. Still we have been able to make the dynamic simulations provide reasonable results.

4.2 *Orifice Model*

The motor-driven compressor loop has no turbine, but uses an orifice to lower the pressure and temperature as it happens in the turbine, but without producing work. The orifice model predicts the mass flow rate given the inlet and outlet pressure and the flow area. It uses the model of compressible flow through a nozzle as described in Bird, Stewart, and Lightfoot (Bird, Stewart, and Lightfoot, 1969). This model works with choked or non-choked flow and assumes that the expansion is isenthalpic, which allows the exit temperature to be determined because the exit pressure is known.

4.3 *Inventory Control Model*

The inventory control simulation block, simply solves for the conservation of mass. This piece of code sums the mass over all components within the loop (which is temperature and pressure dependent) to determine the total mass. The compressor inlet pressure is then adjusted via a feed-back loop to assure that the total mass in the loop equals the fill mass. For the operating conditions modeled in this problem the loop was initially filled with 16.5 kg of CO_2 and the fill mass was held constant.

4.4 *Results of Dynamic Simulation for the S-CO_2 Compression Loop*

A startup transient was simulated in the RPCSIM-CO_2 code as the first problem. The results are illustrated in Figure 4-2. The transient starts the compressor at a shaft speed at near zero rpm and increases it linearly to 75,000 rpm in 10 seconds. The loop structure and the initial CO_2 fluid temperature were assumed to be 307 K. The cooling water started at 301 K and the flow rate increased from 0 to 43.3 gallons per minute in 10 seconds. The predicted results are shown in four plots within Figure 4-2. The top plot illustrates the power transferred to the CO_2 and the cyan line shows the power transferred to the cooling water. At steady state they are the same, but initially the pump puts more power in the gas than is transferred to the cooling water which results in an increase in the ducting and gas chiller structure temperature. The second plot shows the shaft speed (rpm, cyan) and the mass flow rate in kg/s (yellow and magenta). To first order, the mass flow rate is proportional to the shaft speed. The third set of curves show the temperatures at the compressor inlet (yellow), at the compressor outlet (magenta), and at the exit of the orifice (green). The fourth curve shows the inlet (green) and outlet (magenta) compressor pressures (Pa). As expected the pressure increases as the square of the shaft speed and hence is concave up.

In general the results from this prediction appear to be un-remarkable. The components behave as expected, and comparisons with steady state cycle analysis predict the same results if the same pressure ratio (~1.7) and compressor efficiency (80%) are used. However, there are a few observations that are important. First, the loop responds rapidly to changes. This means that the loop will reach its steady state temperature and pressure quickly, on the order of a few 10s of seconds. Evidence of this rapid achievement of equilibrium is seen in the power curve where the power transferred to the CO_2 equilibrates with the cooling water in about 20 seconds. Of course in this simulation there are not large temperature differences thus it does not take long to get to the new temperatures. The second observation is that in this compression loop, even though the gas pressure increased by a factor of 1.7, the inlet pressure remained nearly constant. This is a result of the fact that the average density in the loop stays constant,

and the fact that low pressure leg of the loop has a volume that is much larger than the high pressure leg. Both of these observations have been confirmed during loop operation.

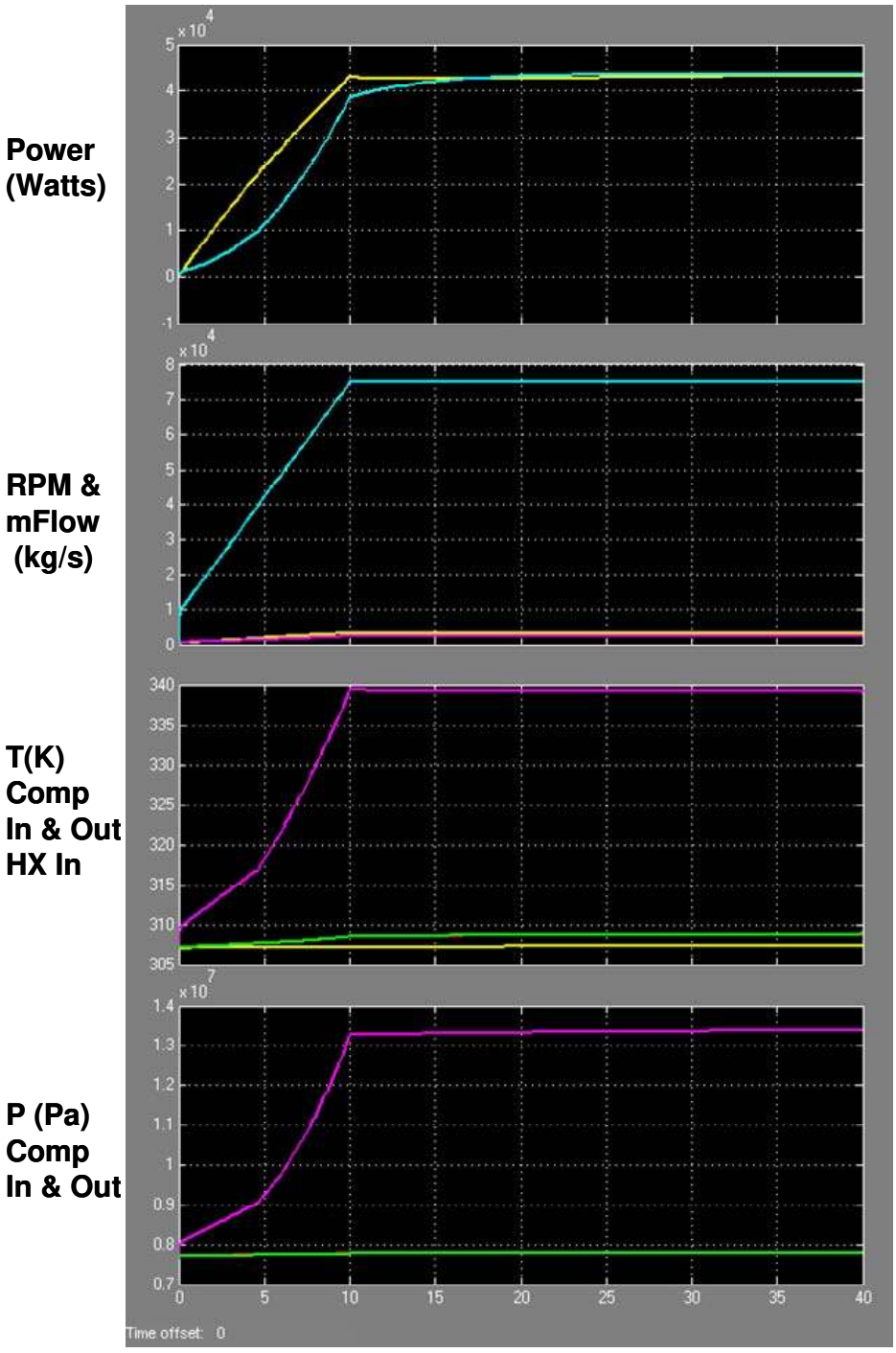

Figure 4-2: Dynamic simulation results illustrating the startup of the compression loop. The top figure shows the power added to the gas (yellow) due to the spin up of the compressor, and the blue curve shows the heat removed by the gas chiller. The second plot shows the spin up of the compressor (blue) while the lower curves show the mass flow rate. The third set of curves show the compressor inlet temperature (yellow) and the compressor outlet temperature (magenta). The bottom plot shows the compressor inlet pressure which remains nearly constant regardless of the shaft speed, and the compressor outlet pressure.

5 Test Results and Observations

This section provides a summary of the development, operation, and control experiments and results generated on the S-CO_2 compression and Brayton loops to date. More details can be found in the many reports generated by the S-CO_2 Brayton team. Some of these reports are listed below and are detailed in the references section.

- Status Report of Small Scale S- CO_2 Brayton Cycle Demonstration Program (2007)
- Supercritical CO_2 Brayton Cycle Compression and Control Near the Critical Point (2008)
- Initial status and test results for a supercritical CO_2 Brayton cycle test-loop (2008)
- Design of the Gen IV Supercritical CO_2 Split-flow Compressor Test Loop (2008)
- Analysis of Supercritical CO_2 Compressor Operation Near the Critical Point of CO_2 (2008)
- Gen IV S-CO_2 Brayton Cycle Test Loop Design and Split-flow S-CO_2 Compressor Test Loop Construction Description (2009)
- Supercritical CO_2 Compression Loop Operation and Test Results (2009)
- Supercritical CO_2 Heated, but Un-recuperated, Brayton Loop Operation and Test Results (2009)
- Supercritical CO_2 Test Loop Operation and First Test Results (2009)
- Supercritical CO_2 Brayton Cycle Power Generation Development Program and Initial Test Results (2009)

5.1 *Control of the S-CO_2 Compression Loop*

The schematic diagram of the supercritical compression loop that is illustrated in Figure 5-32 also indicates the major control mechanisms. These items are indicated by the red numbers in the figure and include the following:

1. **Compressor motor speed:** Changing the compressor speed directly affects the S-CO_2 flow in the loop. To first order, the mass flow rate is proportional to the compressor speed, the compression ratio is proportional to the speed squared and the compressor power is proportional to the third power of the speed. Therefore, changes in speed will have dramatic effects on temperature and power.
2. **Orifice Valve:** The orifice valve is used to adjust the flow rate and pressure ratio through the loop. Because the loop is closed, the sum of the pressure drop in the ducting, gas chiller, and in the orifice valve must equal the pressure rise in the compressor. Because the flow area in the orifice can be adjusted, it is possible to vary both the pressure ratio and flow rate at a fixed shaft speed by simply changing the valve setting on the orifice control valve. In the photos, this valve is shown as a manual valve, but we have replaced this valve with a motor-driven valve.
3. **Fill Inventory Valve:** The compression loop is filled from CO_2 gas cylinders through a Haskel booster pump. At room temperature, the fluid in a gas cylinder is a liquid at about 850 psia, thus the loop needs a pressure booster pump, a pressure regulator, and a valve to increase the pressure to nominal operating pressure of 1100 psia which is above the critical pressure (1070 psia). The S-CO_2 compression loop is designed to operate at a compressor inlet pressure that varies from 5000kPa (725 psia) to 9200kPa (1334 psia). At the lowest fill pressures, the CO_2 inventory in the loop is approximately 12 kg. At the highest fill pressures, the inventory is on the order of 43 kg.

4. **Inventory Bleed Valve:** This valve is used to bleed gas that is in the compression loop and thereby lower the inventory levels and the compressor inlet pressure. Opening this valve will lower the gas pressure in the loop.
5. **Cooling water pump speed:** The cooling water pump speed can be varied to change the flow rate of the coolant, which affects the water temperature to rise in the gas chiller and heat transfer coefficient. The pump speed is generally held constant.
6. **Cooling water recirculation valve:** This valve controls the amount of warm cooling water exiting the gas chiller that is circulated through the pump without going through the cooling tower. This will allow control of the cooling water inlet temperature over a wide range of conditions and will be needed during cold winter days.
7. **Cooling water tower spray:** At Sandia, the cooling tower has settings to control the set point temperature of the chilled water. Initially, the S-CO_2 controller will not be able to change this set point as it must be performed manually.

5.1.1 Control Example

Figure 5-1 shows a T-S (Tepmerature-Entorpy) map for CO_2 with the compressor inlet state point locations superimposed on the graph. The state points for five selected tests that were conducted by Sandia and Barber Nichols are shown as green stars on the plot. As the tests progressed in time (test sequence number) the compressor inlet density increases from a low of 0.148 kg/liter on the vapor side of the saturation dome to a high of 0.567 kg/liter, near the liquid side. Because the density increases, the mass or inventory of CO_2 in the loop varies from 8.2 kg for the lowest density to 31.7 kg for the high density test.

During the tests, the inlet temperature and pressure were manually controlled. The data acquisition and control system displays the T-S or the T-Density (T-D) map of supercritical CO_2. In real time, the display provides an indication of whether conditions were in the supercritical region or on the liquid or vapor side of the dome. During startup, the initial temperatures are at room temperature, which is well below the critical point. Thus during startup the CO_2 state points are on the saturation liquid-vapor curve. To get above the dome (saturation curve), the temperature was adjusted by heating the water temperature reservoir of ~300 gallons to 88-90°F or by running the compressor at low rpm (10,000) which required about 10 kW of motor power. No cooling was required because the room temperature of the water reservoir was well below the critical temperature.

The density was controlled by pumping more CO_2 into the loop or by venting. The Coriolis flow meter proved to be a valuable control signal as it measures the density directly. Increasing the density lowers the entropy as illustrated by the T-S curve of Figure 5-1. Note also that near the top of the dome the T-S curve shows that, as fluid is added to the loop one will observe only small changes in the fill pressure. This made it difficult to determine when to stop filling the loop based on pressure alone, but this issue was nicely solved by having the Coriolis meter that provides the density (provided the fluid is in the single phase region).

The water flow through the pre-cooler was not controlled other than by heating the water reservoir prior to starting a spin test. The gas booster pump operating speed was manually controlled by opening or closing a shut off valve. The CO_2 fill was controlled manually as well. Many of these activities will be automated in future configurations of the test hardware. Because the water recirculation valve was not

controlled during many of the tests, some tests allowed the compressor inlet conditions to drift into the two-phase region (in the dome).

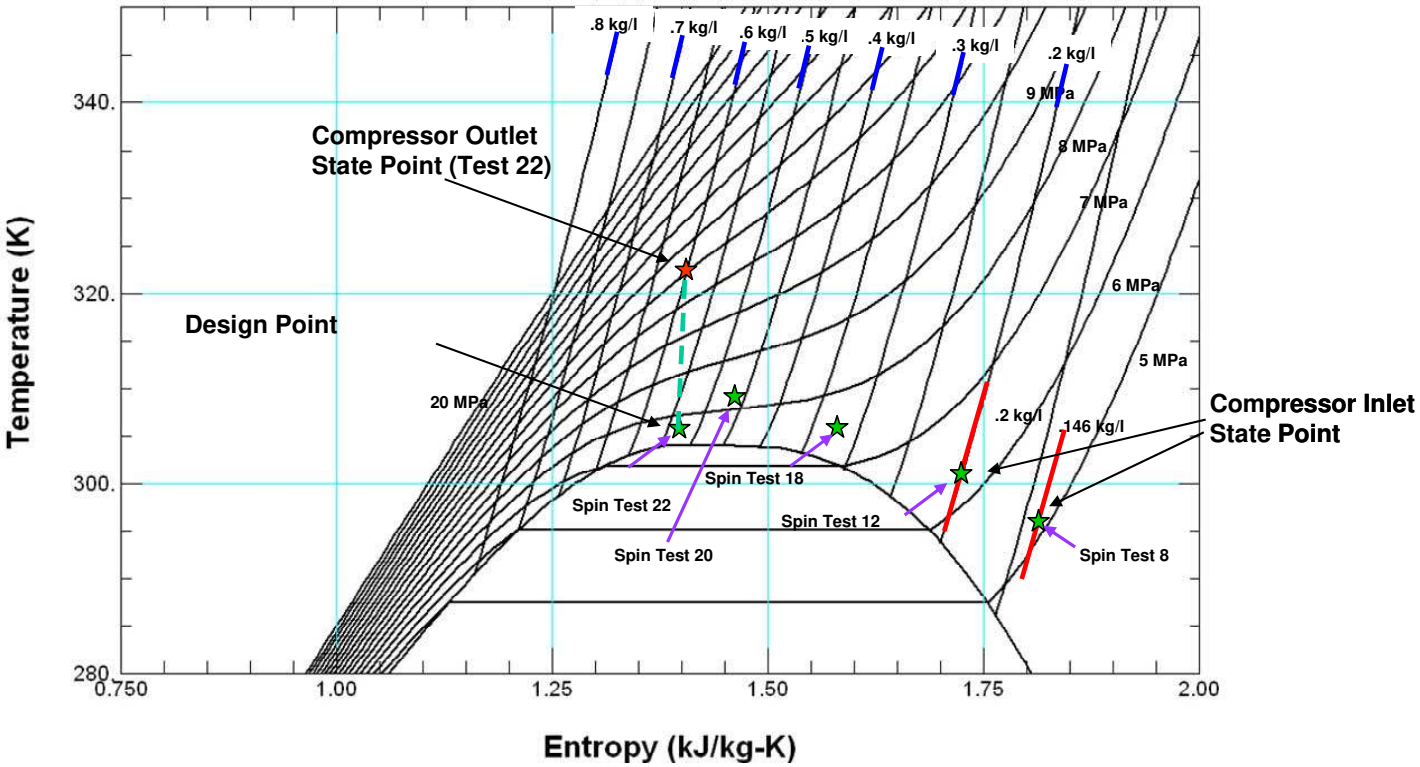

Figure 5-1: Temperature Entropy (T-S) plot showing the compressor inlet state point locations from selected spin tests.

5.1.2 Operating near the Pseudo-Critical Line

The T-S path that the CO_2 fluid undergoes in the gas chiller and in the compressor is shown as a green dashed line in Figure 5-2. The compressor inlet conditions are indicted by the large green dot at the lower left of the green dashed CO_2 path or line. As the control system varies the compressor inlet conditions, the location of this path moves around the liquid-vapor dome and changes shape to accommodate the new pressure ratios and temperatures. One of our major goals in this program is to measure the compressor response as we move the compression path around the liquid vapor dome.

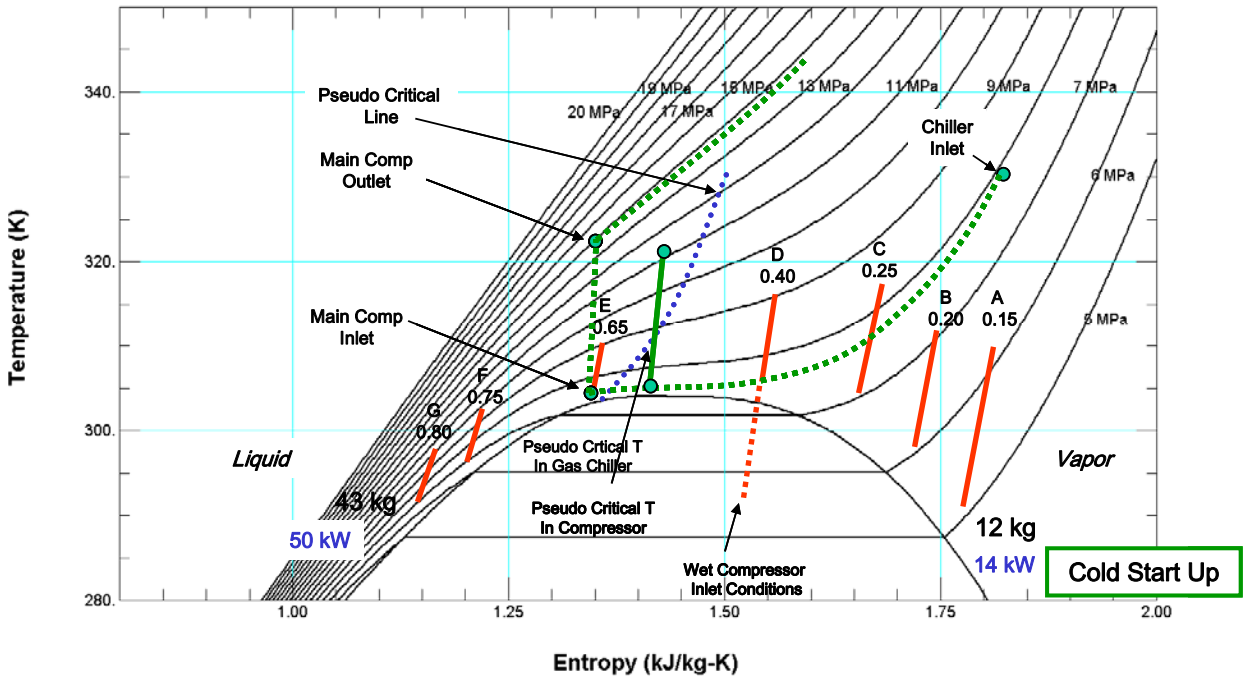

Figure 5-2: Temperature entropy diagram for CO_2 near the critical point. The green curves indicate the T-S path for CO_2 flow in the gas chiller, in the compressor and during heating in either the recuperator or a heater. The red lines show the range of compressor inlet conditions that we intend to operate the loop at. Note that they roughly follow the lines on constant density and vary from a low density of 0.15 kg/liter to a high density of 0.80 kg/m^3 over a temperature range from 290 K to 318 K. The blue dotted line shows the pseudo-critical points where large peaks in the heat capacity and viscosity are observed.

The blue dotted line in Figure 5-2 shows the approximate location of the pseudo-critical line. This line represents temperature and pressure conditions where large increases in heat capacity are observed due to the vaporization-like processes that are occurring at the pseudo-critical point. Note that at the design conditions, the pseudo-critical point occurs in the gas chiller. The increased heat capacity near the pseudo-critical point increases the heat transfer coefficient (through the Prandtl number) and causes a very low ΔT in the heat rejection gas-chiller. This means that at this point in the gas chiller the heat transfer is nearly isothermal and approaches boiling/condensation-like heat transfer processes. Note, that by moving the compressor inlet conditions to the right in this T-S plot (by lowering the fill inventory) the pseudo-critical point can be made to occur in the compressor. We intend to operate the loop with the pseudo-critical point in the gas chiller and in the compressor. These tests have not been performed to date.

The data acquisition and control system that Sandia uses was developed to help the operators understand and visually determine where the operating state points are with respect to the liquid-vapor saturation dome and the critical point. This control system was developed by Prime Core Systems on contract to Sandia (PrimeCore Systems, 2008). A number of plots are provided in this controller to help the operator. Figure 5-3 shows an image from our control system illustrating the T-S diagram of S-CO_2 which plots the state points for one experiment that stepped the shaft speeds from 10,000 rpm to 65,000 rpm. The red dots show the T-S locations at compressor inlet, the compressor outlet (green), and after the expansion valve (blue) which is also the location just before the gas chiller. Lines of constant pressure are also

shown on this plot. A similar plot on the temperature-density curve is also plotted. Notice that in this test the compressor inlet conditions started out on the saturation curve and that as we increased shaft speed the inlet temperature increased sufficiently to exceed the critical temperature.

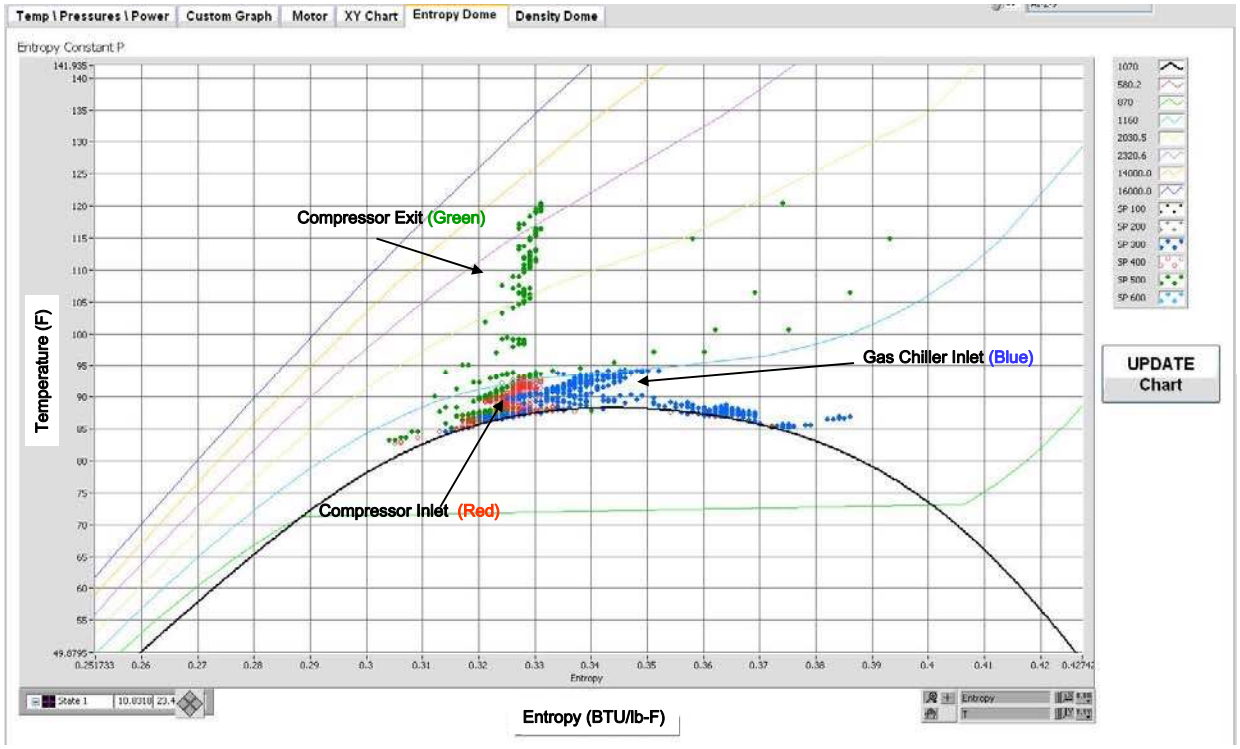

Figure 5-3: Image from the Sandia S-CO_2 compression loop control system showing the location of the state points on the T-S diagram. Red and green points are compressor inlet and outlet conditions (respectively) and the blue points are the T-S conditions after the flow control valve which is at the inlet to the gas chiller.

5.1.3 Entering the Dome (Saturation Curve)

The supercritical Brayton cycle takes advantage of the non-ideal properties of S-CO_2 to increase the efficiency of the cycle near the critical point. This requires that the compressor inlet temperature and pressure be maintained at conditions that are very close (~1-2°C ΔT, and 100 - 400 kPa ΔP) to the critical point. Because of the close approach to the critical point, it is desirable to understand the behavior of the system in case the compressor inlet-control system allows the inlet-conditions to drift below the critical point.

During system start up and preheating, Sandia and Barber Nichols have operated the compression loop for long periods of time (hours) while the compressor inlet conditions were below the critical point and thus in the two-phase region. The power provided by the compressor was generally capable of heating the loop cooling water and thus raise the compressor inlet temperature to above the critical point after a few hours of spinning. Figure 5-4 shows the measured temperatures during the portion of the test where the two-phase region was entered.

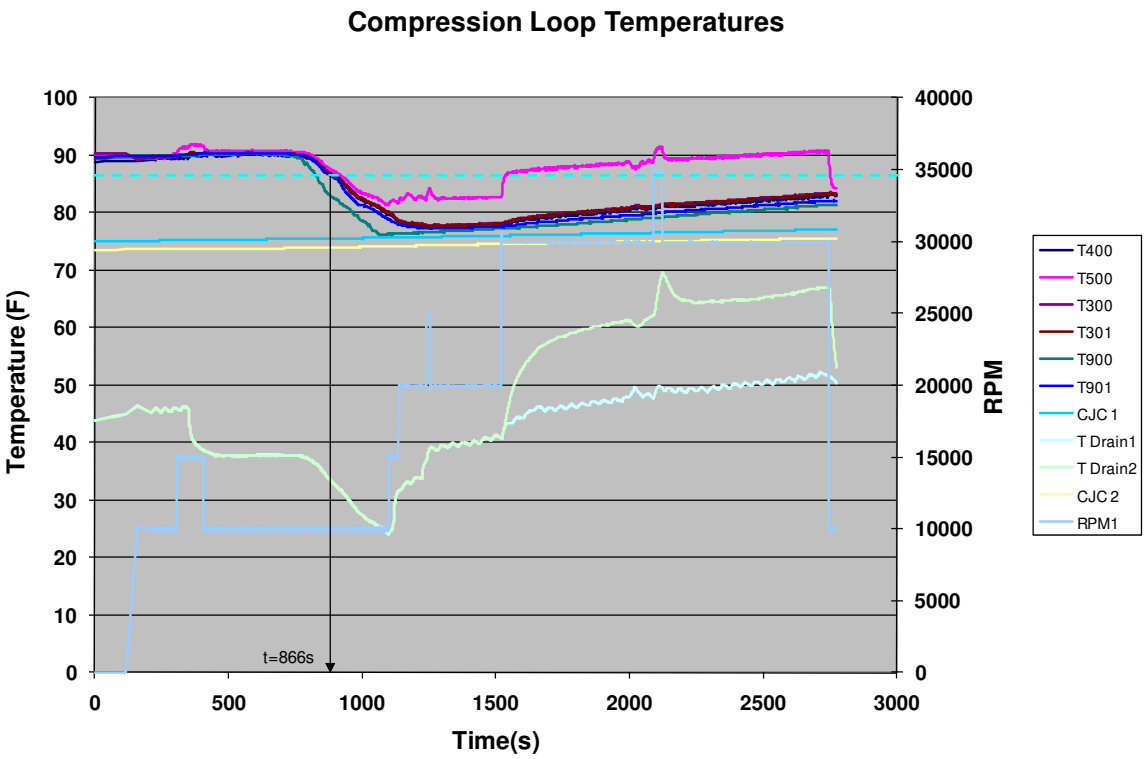

Figure 5-4: Recorded temperatures in test CBC_081202_0819 showing the reduction in temperature to below the critical point at 866 s into the test. T400 is the compressor inlet temperature and T500 is the outlet.

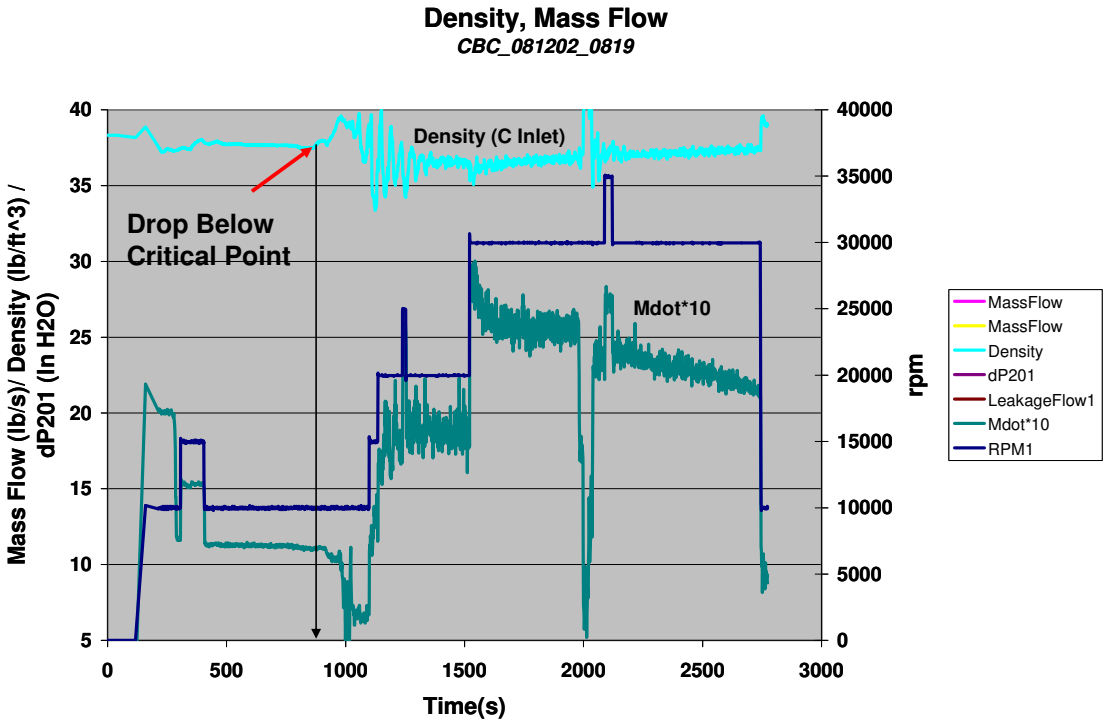

Figure 5-5. The behavior of the compression loop when the compressor inlet temperature and pressure fall below the critical point is illustrated in the above figure. Note that the measured flow rate is multiplied by a factor of 10.

In this operation of the compression loop, the compressor inlet conditions started out above the critical point but due to over-cooling the compressor inlet temperature and pressure drifted below the critical point. Typically, the target compressor inlet conditions were 90°F (305.4 K) and ~1100 psia (7600 kPa). The behavior of the loop in this test, when the compressor inlet fell below the critical point, is illustrated in Figure 5-5 and in Figure 5-6. These figures show the density and flow rate. These values were measured by the Micro Motion model DH150S Coriolis flow meter, which was located about 0.5 m before the actual compressor inlet. In the graphs, the flow rate is multiplied by a factor of 10 in Figure 5-5 and by a factor of 20 in Figure 5-6 so that good comparisons with the density fluctuations can be made.

Notice that as the inlet-conditions drop below the critical point the density and flow begin to show oscillations. The oscillation period is very slow (about 60 seconds), and the density of the oscillations vary from 33 - 40 lb/ft^3 (528-640 kg/ m^3). Even though the temperature and pressure signals clearly indicated that the compressor inlet was below the critical point they showed no indications of these oscillations. For a single phase fluid if the compressor were operating at constant speed the mass flow rate would be directly proportional to the density, however the expanded view (Figure 5-6) clearly shows that the mass flow and density are 180 degrees out-of-phase. This fact, together with the very slow period of oscillation, suggests that the oscillations are related to the fluid circulation time in the loop which is about 60 seconds at this flow rate, and it is not a compressor phenomenon. Similar behavior was observed in the heated, but un-recuperated, Brayton loop however the density of fluctuations span the full range of density from 15 – 40 lb/ft^3 (240-640 kg/m^3) and the mass flow rate and density fluctuations in this case were in phase. No fluctuations in pumping power were observed in either case, however it is likely the resolution of the power meter was too coarse to detect small power oscillations below 500 W.

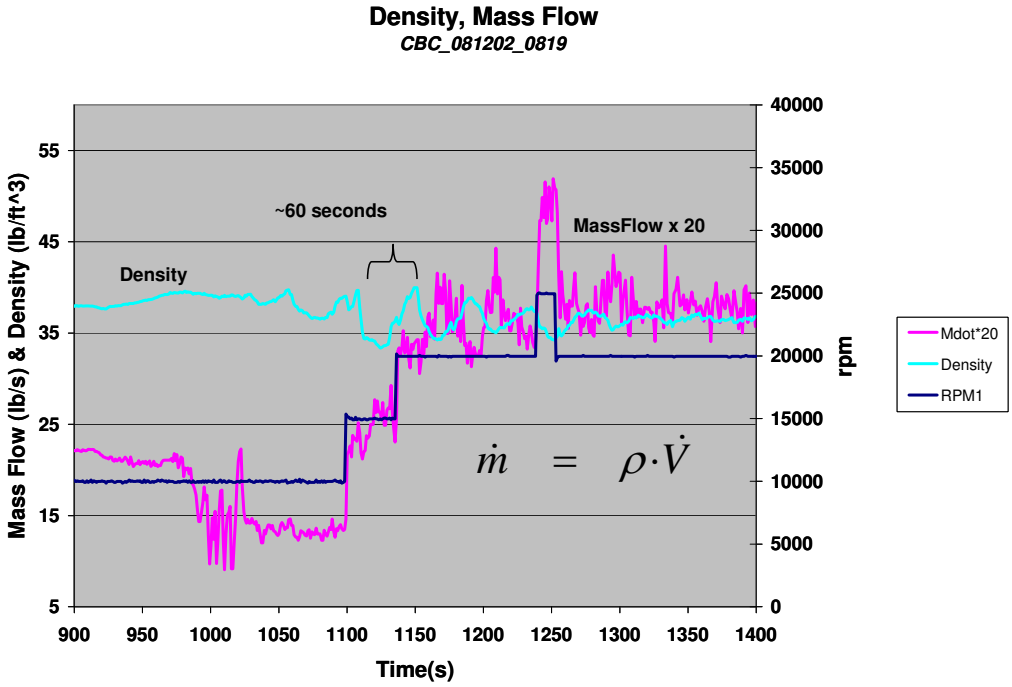

Figure 5-6. The figure shows an expanded view of the density and flow oscillations that were observed while operating below the critical point. Notice the out-of-phase relationship between measured mass flow rate and density.

5.2 *High Speed Spin Test*

Spin Test 22, (October 17, 2008), had a peak shaft speed of 65,000 rpm and pumped 5.25 lb/s (2.4 kg/s) at a compressor inlet of 92.6°F (306.8 K) and 1154 psia (7956 kPa). The maximum measured pressure ratio was 1.58 and the measured motor power was 53 kWe. Power level, compressor outlet temperature, pressure values, and other compressor performance values agree well with the predicted performance maps that were generated by Barber Nichols for these operating speeds (rotor windage losses are included). The results also agree with the Sandia mean-line flow analysis compressor model. The early agreement between models and measurements provides early confirmation of the design basis and performance predictions for the system.

More detailed plots of the measured data are shown in Figure 5-7 and Figure 5-8. Figure 5-7 shows the measured shaft speed (blue, rpm), power (magenta, W), and mass flow rate (green, lb/s). The mass flow was measured by the Coriolis flow meter. Before the test began, the gas chiller flow was started, and the orifice control valve was set to a fixed open fraction. The test began by starting the motor/controller and rapidly increasing speed to 10,000 rpm. The shaft speed was kept at this speed for several minutes to allow the loop to approach steady-state conditions. During this time the gas booster pumps were turned on to reduce the gas pressure in the rotor cavity. The reduced cavity pressure provides two functions. First it provides cooling to the bearings, and second it reduces the windage losses on the rotor.

Once equilibrium temperatures were reached the shaft speed was increased in increments of 10,000 or 5,000 rpm. At each shaft speed the compressor outlet temperature was allowed to approach steady-state conditions before going to the next shaft speed. The test was stopped after reaching 65,000 rpm to allow Sandia and Barber-Nichols to evaluate the performance of the turbomachinery and the loop before proceeding to the final 75000 rpm. A peak power of 53 kWe was measured in the motor controller, and a peak mass flow rate of 5.25 kg/s (2.38 kg/s) was measured by the Coriolis flow meter. The Coriolis flow meter also provides a real time measure of the compressor inlet density. This measurement shows that the inlet density remains constant (as expected) at 35.5 lb/ft^3 (0.567 kg/liter) regardless of the shaft speed.

Figure 5-8 shows the measured pressures and shaft speed as a function of time during this test. The compressor exit pressure P500 is shown as the purple curve while the dark blue line shows the static pressure at the tip of the compressor blade (P100). The inlet pressure (P400) is the cyan curve. Knowing the static pressure at the compressor tip and the total pressure at the compressor exit allows one to estimate the CO_2 velocity at the exit of the wheel, which helps confirm the compressor performance. The CO_2 fluid velocity was on the order of 85 m/s and the tip speed was 125 m/s.

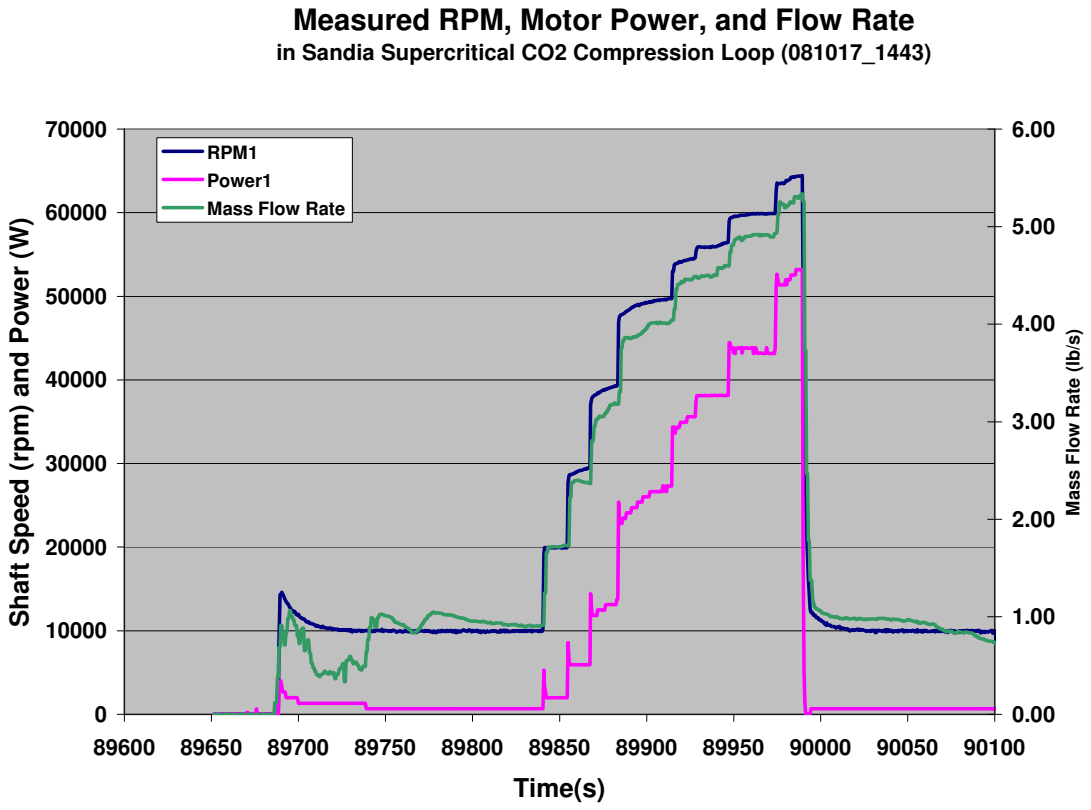

Figure 5-7: Measured motor power, mass flow rate, and shaft speed through the supercritical CO_2 compressor driven. Peak shaft speed in this test was 65,000 rpm, the flow rate 5.25 lb/s and the motor power was 53 kW.

The peak measured pressure ratio was 1.58. When the compressor was started the outlet pressure increases and both the inlet and exit pressure increases when the gas booster pumps are turned on. The booster pumps transfer some of the fluid from the rotor cavity volume (~ 4% of total volume) to the gas pre-cooler and compressor ducting volume which results in a pressure increase.

The brown curve in Figure 5-8 shows the rotor cavity pressure (Pdrain) which was reduced to about 500 psia by the gas booster pumps. The pressure then increased as the compressor exit pressure increased until it saturated at about 800 psia. At this point we believe that the gas booster pumps were in equilibrium with the leakage flow rate. In this test the gas booster pumps were cycling slowly (a few seconds per cycle). At higher speeds they are capable of lowering the rotor cavity pressure even further.

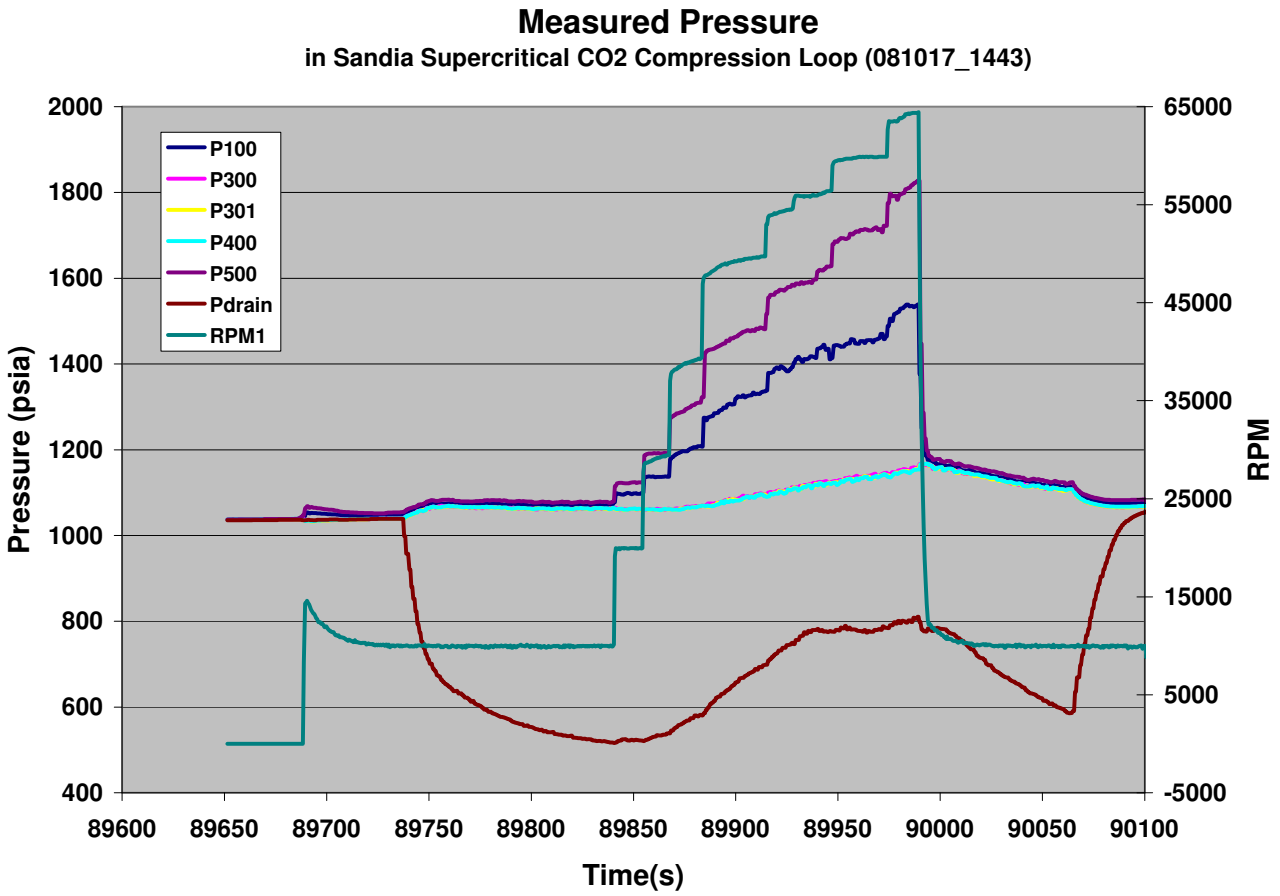

Figure 5-8: Measure pressure rise for the stair stepped increase in shaft speed. P500 is the compressor outlet pressure, P400 is the compressor inlet pressure, and P100 is the static pressure at the tip of the compressor blade. Pdrain is the rotor cavity pressure that was reduced to reduce windage losses.

5.3 *Compressor Performance*

The compressor wheel and its detailed design were developed by Sandia's contractor Barber Nichols using a variety of existing in-house tools and codes. Because the deviation of supercritical CO_2 fluid properties from ideal gas behavior is extreme, early attempts to use existing design tools and couple them to the NIST REFPROP (Lemmon, 2007) equation of state database (or other databases) for supercritical CO_2 proved unsuccessful. Furthermore, because the formulation and solution methods used by the available design tools is based on heat capacity rather than enthalpy, it is not even practical to rewrite existing design tools to call non-ideal fluid property libraries in place of equations derived from idealized fluid assumptions.

For the supercritical CO_2 compressor, Sandia's design contractor Barber-Nichols developed a methodology that allows traditional engineering design tools to be used despite substantial deviation from ideal gas behavior. The method involves the use of a surrogate fluid that possesses key similarities to the

actual fluid, but which can be more closely approximated by an ideal gas model. These key parameters were selected from turbomachinery similarity principles and non-ideal gas properties.

This method of analysis adjusts the density, temperature, and other properties of the surrogate fluid so that the volumetric flow rate and adiabatic head produce inlet and exit flow angles that are identical to those in the supercritical fluid. This results in a design that has the correct flow passage dimensions and velocity vectors for the same shaft rpm. In addition, the loss models for the near ideal gas (in the surrogate fluid) are applied and used to predict the isentropic efficiency for the supercritical fluid. This method introduces many approximations but provides a way to use existing loss models and design tools such as the NASA CCODP code (Galvas, 1973) to develop the detailed design of the turbomachinery and to predict its performance.

The development of this capability is extremely important and was performed early in the program, because these tools were needed to develop the detailed design so that the wheels could be manufactured. The method has been successfully applied to both supercritical CO_2 compressors and turbines. At the same time, Sandia has been developing its own code to predict supercritical CO_2 compressor and turbine performance. In spite of the very different approaches taken by these two methods, they produce similar results.

Table 5.1 summarizes the main design features of the main compressor. The first column describes the property, the second gives the variable name and units, and the last column provides the value. The small size of the compressor wheel is further exhibited by the height of the blade at the exit of the compressor, (only 1.7 mm), in spite of the fact that the compressor is pumping 3.53 kg/s or 13 tons per hour of CO_2 and operates at about 50 kW or 70 horse power.

At Sandia, we have developed a simple, but fundamental mean-line flow analysis code to model the compressor performance. This code is implemented in Excel, and uses enthalpy based sets of equations coupled to the NIST REFPROP data base to model the flow at the compressor inlet and outlet. The method closely follows the approach described in Japikse (Japikse, 1996 & 1997) and requires a non-linear solution to 19 simultaneous equations. The loss models use a combination of methods described by Jiang (Jiang, 2006) and Oh (Oh, 1997). The loss models currently account for inlet and outlet flow deviation, disk friction, clearance effects and other effects. The Sandia compressor model is still being developed and more effort needs to be applied to the implementation of the loss models and improved models for the diffuser.

Table 5.1: A summary of the S-CO_2 compressor wheel operating characteristics and the design dimensions are listed in this table. These values were used in the BNI design tools and the SNL mean line flow analysis code to determine the operating performance characteristics. The design pressure ratio is 1.8.

Compressor Operating Conditions	Variable	Units	Value
Shaft Speed rpm	Nrpm	rev/min	75000
Shaft Speed rps	Nrps	rev/s	1250
Inlet Temperature (total)	T.o1	K	305.30
Mass Flow Rate	mdot	kg/s	3.53
Inlet Pressure	p.o1	kPa	7687
Compressor Design Dimensions			
r.tip	r.tip	m	0.0186817
blade Height	b.2	m	0.001712036
Blade tip angle (minus is back swept)	beta.2b	deg	-50
Number of exit blades	Z.r		12
Thickness of blade	t.b	m	0.000762
Shroud Radius	r.s1	m	0.009372047
Hub Inlet Radius	r.h1	m	0.002537485
Inlet Blade Angle at tip	beta.1bt	deg	50
Exit Vaned Diffuser Angle	alpha.2	deg	71.5
Tip clearance	l.c1	m	0.000254

5.3.1 Measured Compressor Maps

This section of the report describes the test measurements that were used to map the performance characteristics of the main compressor. The goal of these tests was to spin the TAC at a fixed speed and then use the motor driven flow control valve to reduce the flow while recording inlet and outlet temperature and pressure along with the motor controller power. Overall the shaft was rotated at speeds varying from 45 krpm to 60 krpm in increments of 5 krpm.

Figure 5-9 and Figure 5-10 show a short section of the pressure, mass flow rate, and power data that was recorded in test CBC_081202_1003. The presented data was recorded while at 55 krpm. In both figures the shaft speed and motor controller power use the secondary axis located on the right side of the graph. The starting compressor inlet temperature and pressure were 304.4 K (88.3 F) and 7.536 MPa (1093 psia) which was very near the critical point (87.8°F /304.1 K and 1070 psia / 7377 kPa).

In Figure 5-9 the shaft speed was increased from 10 krpm to 55 krpm in about 10 seconds in a series of steps. These step changes in speed were limited to 15 krpm to avoid over currents in the motor controller. As the speed increases the outlet pressure increases as well. Once the shaft speed reached 55 krpm it was kept constant. At high speed (55 krpm) the compressor outlet temperature increased approximately 11.1 K (20°F). At 12,335 seconds into the recorded data the flow control valve was closed in steps, each valve closure step caused further increases in the compressor outlet pressure which also cause reductions in the mass flow rate. The maximum outlet pressure measured in this phase of the test reached 12.1 MPa (1757 psia).

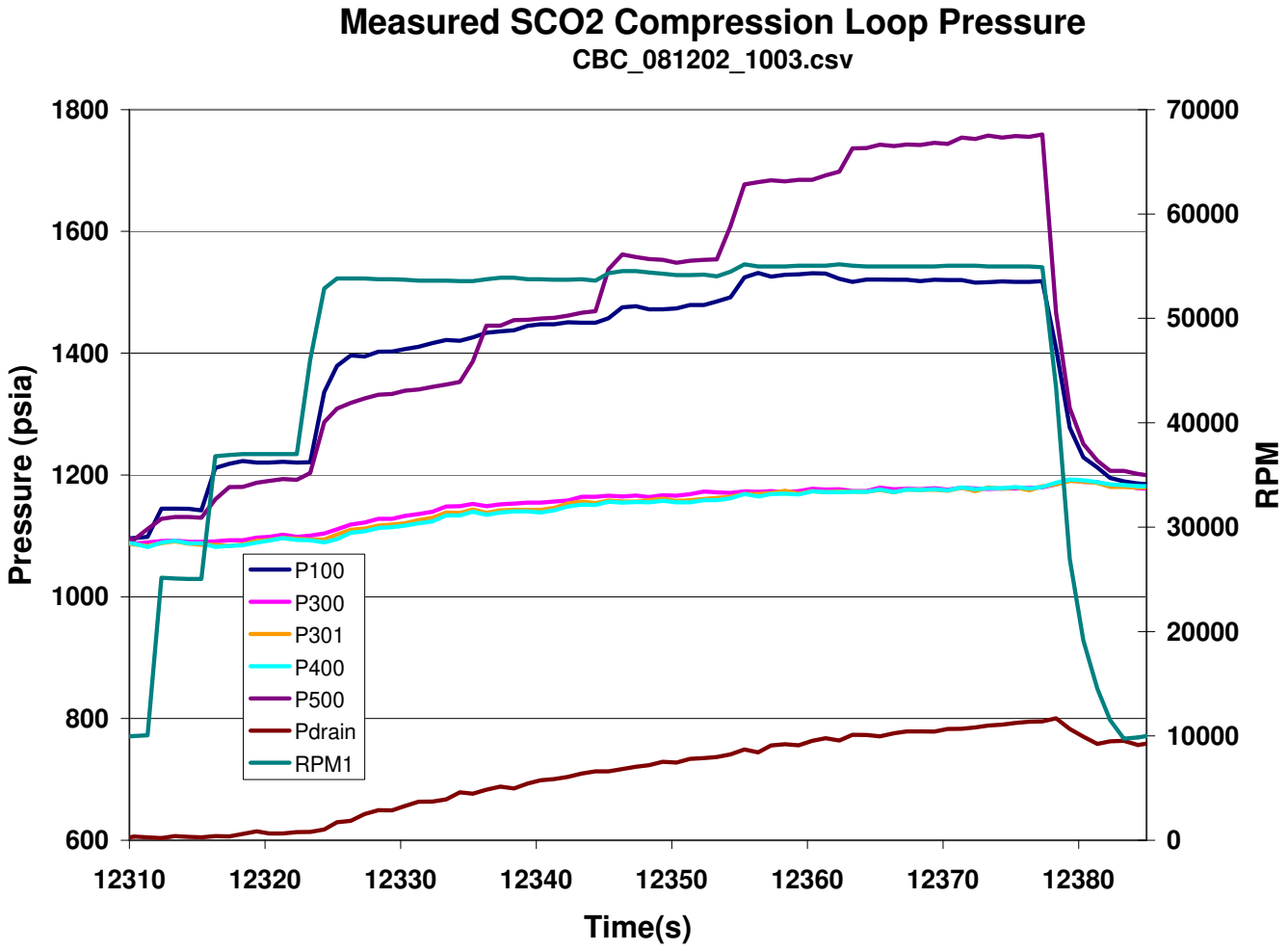

Figure 5-9: Measured pressure (psia) at the main compressor inlet (P400) and outlet (P500) as a function time. P100 is the static pressure at the tip of the compressor wheel. Pdrain is the rotor cavity pressure which was reduced to lower windage losses and to cool the bearings. The shaft speed is also shown.

Figure 5-10 shows the mass flow rate and the motor controller power for the same time period. The mass flow rate peaks at the beginning of the run when the shaft speed was 55 krpm because the flow valve is at its most open position. The motor controller power was at its maximum as well (near 41 kW). As the valve closes, the mass flow rate decreased from 3.95 kg/s (8.7 lb/s) to 1.64 kg/s (3.6 lb/s). While the outlet pressure increased and the motor power decreased as well. The motor controller power was measured in the controller. It is estimated that only about 93% of this power actually results in motor power torque to the compressor while the rest is lost in the switching circuitry and in magnetic losses within the stator windings.

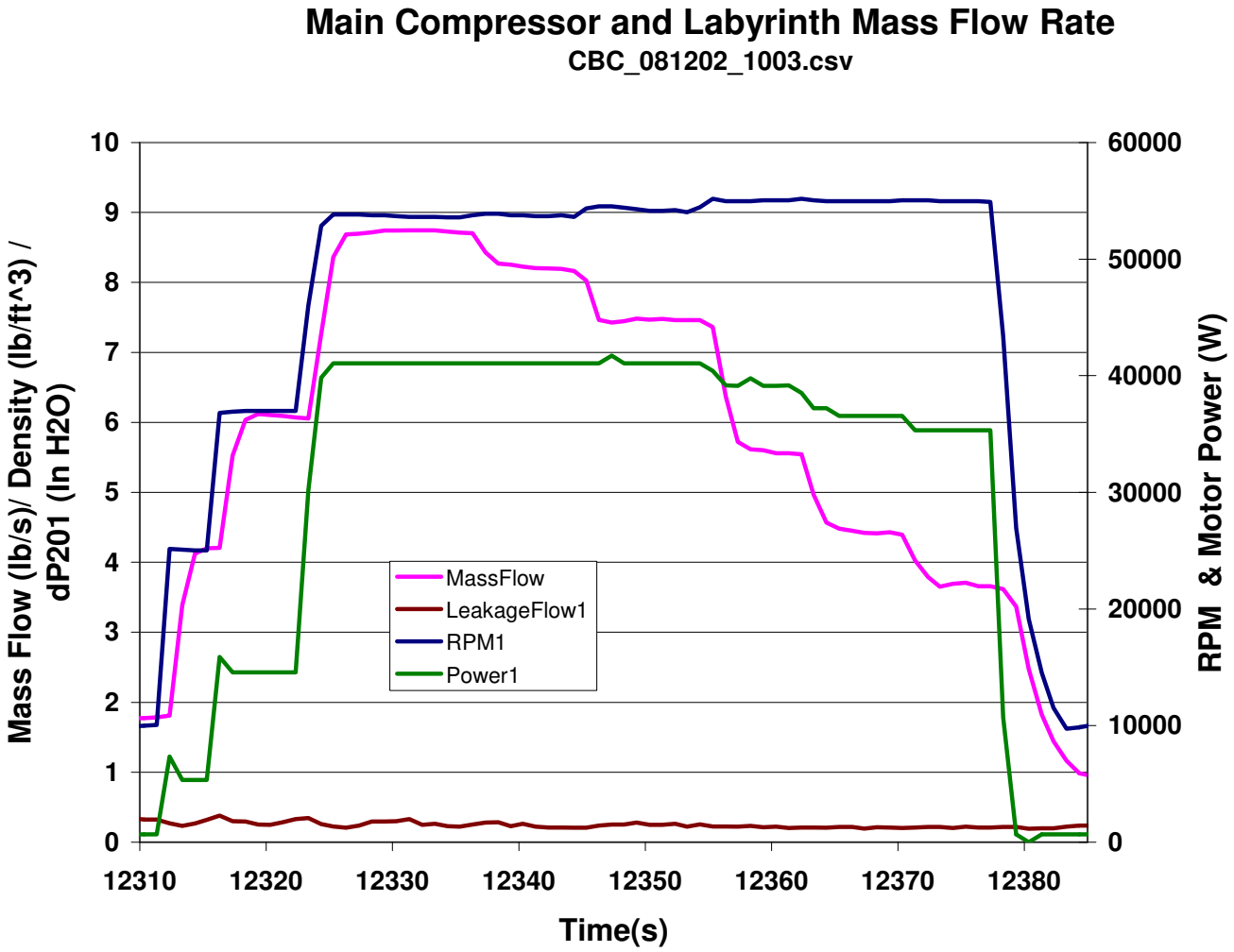

Figure 5-10: Measured mass flow rate and labyrinth seal leakage flow rate (lb/s) as a function of time. At ~12335 s the flow control valve was closed in a series of steps resulting in a decrease in flow from 8.7 lb/s to 3.6 lb/s.

The data provided in Figure 5-10 was used to make the performance maps. The maps consist of two curves. The first is shown in Figure 5-11 and plots the corrected or equivalent specific enthalpy change as a function of corrected or equivalent flow rate. The corrected values account for differences between the actual temperature and pressure at which the data was taken and the reference values. These equations are described in Glassman, 1972 and in Noalls 2008. The black lines show the predicted values and the markers show the measured values. The change in enthalpy values are based on the measured temperature and pressures.

The second performance map (see Figure 5-12) compares the measured efficiency with the predicted efficiency. The efficiencies are based on the measured motor controller power with corrections to account for windage losses and pump vane power losses which are estimated to be 17% of the windage losses. The windage losses are significant and must be included. The windage losses use the correlation by Vrancik (Vrancik, 1968) and depend on the measured rotor cavity density and viscosity which are estimated from the measured rotor cavity pressure and temperature. The efficiency plots are shown at

three different shaft speeds (45, 50, and 55 krpm) in Figure 5-12. The measured efficiency is shown with markers, while the predicted efficiency is shown as thin lines for each rpm.

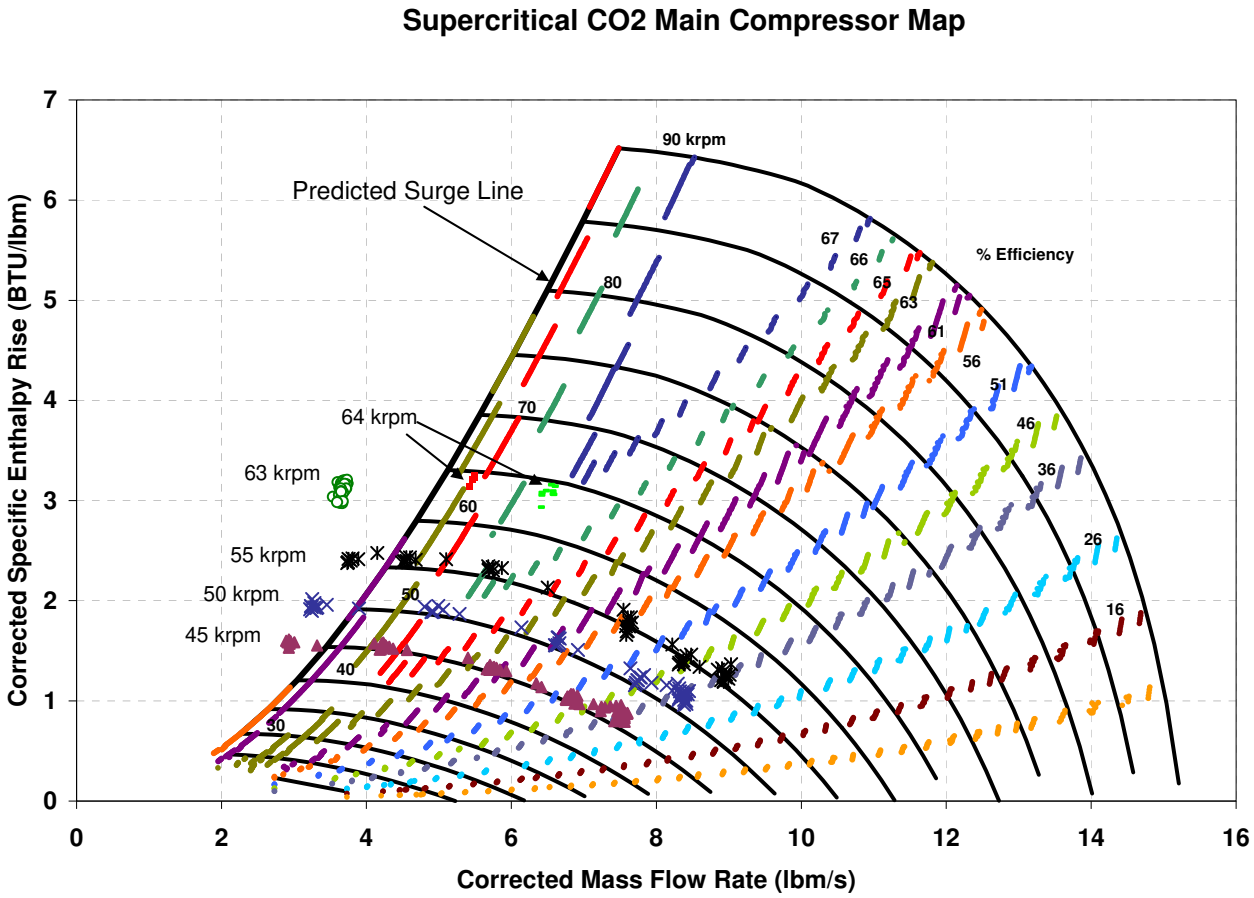

Figure 5-11: Comparison of the predicted and measured flow performance for the main compressor in the SNL supercritical CO_2 test loops. The plot shows the corrected enthalpy change as a function of corrected mass flow rate for parametric variations in corrected speed. This performance map was made at compressor inlet temperature and pressure conditions that were very near the critical point of 304.1 K and 7377 kPa. During these tests the compressor inlet conditions varied from 304.3 – 307 K and 7700-8139 kPa.

The compression loop used the motor driven compressor to measure the compressor performance map at varying inlet temperature and pressure levels near the top of the saturation curve (or dome). This was done by running the loop at constant shaft speed and then slowly closing the motor-driven main compressor flow valve. A plot of the resulting pressure ratio or enthalpy change as a function of flow rate defines the compressor performance map. The turbomachinery was instrumented with compressor inlet and outlet RTD's to measure temperature and pressure transducers to measure the inlet and outlet pressure. In addition, the compressor also has a pressure transducer that measures the static pressure at the compressor tip (labeled P100). Thermistors were used to measure the motor and bearing temperature. As already mentioned, a Coriolis flow meter located near the inlet of the compressor was used to measure flow rate and fluid density. The direct measurement of fluid density proved to be valuable for controlling the fill process and for controlling the preheating during the approach to the critical point.

The agreement between prediction and measurement is good. Overall, we believe that this validates the "similarity" approach used to predict the performance curves and to design the compressors and turbines.

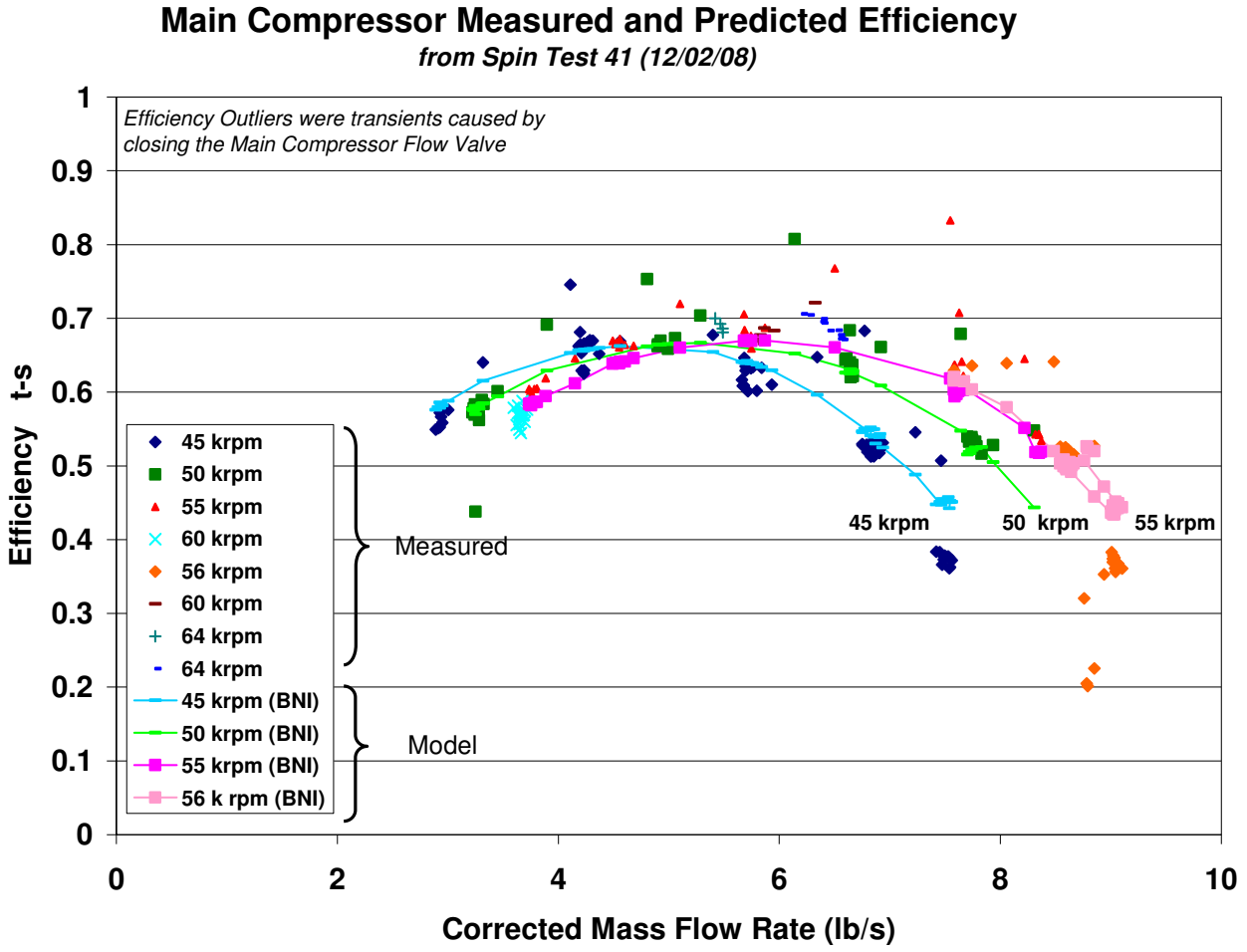

Figure 5-12: Comparison of the predicted and measured compressor efficiency for the main compressor in the SNL supercritical CO_2 test loop. The plot shows the compressor efficiency (t-s) a function of corrected mass flow rate for parametric variations in corrected speed. This performance map was made using the same compressor conditions and data as the enthalpy map shown in the previous figure.

5.4 *Windage Losses*

Because the shaft speeds are high (large fractions of the speed of sound) and because the fluid densities are large (approaching the density of water), significant friction occurs between the moving shaft and the fluid. These losses are called windage losses. The high pressure and high density in the S-CO_2 Brayton cycle can also cause significant thrust loads, and leakage flow rates through seals that must be properly managed by the design. The initial configuration of the S-CO_2 compression loop uses labyrinth seals on the compressor shaft to separate the rotor cavity from the high pressures in the compressor (and turbine). The gas-foil bearings and the ball bearings are located in the rotor cavity. The rotor cavity operates at reduced pressure (density) to lower the frictional losses.

In the Sandia compression loop separate gas booster pumps lower the pressure and density in the rotor cavity by pumping the CO_2 out of the rotor cavity and back into the low pressure leg of the loop. This is illustrated by the red lines in Figure 2-6 and in Figure 2-7. In addition the compressor wheel uses pump-out vanes to balance the forces across the compressor and thus reduce the thrust load on the shaft. The rotor cavity pressure also affects the thrust load. The turbo-alternator-compressor has two types of rotor shafts. One shaft uses ball bearings and the other shaft uses gas foil bearings. The ball bearing rotor has a limited life, but it is configured with a load cell to measure the axial thrust load (see Figure 5-13). The load cell is used to measure the actual thrust and to validate the thrust models. Because the thrust load capability of gas foil bearing is limited, it also allows the manufacturer (Barber Nichols) to trim the pump-out vanes. A flow meter was also installed to measure the leakage flow rate through the rotor cavity.

The final configuration of the compression loop will operate with gas-foil bearings. Separate tests of gas-foil bearings (DellaCorte, 2006) reveal that the power losses in the gas foil bearing increases with gas pressure, just as the windage increases with pressure. Thus, to avoid overheating the bearings, it is desirable to operate the gas-foil bearings at low pressures as well. In the Sandia/Barber-Nichols turbo-alternator-compressor design, our design goal is to operate the rotor cavity a pressures below approximately 300 psia. The leakage flow through the labyrinth seals also provides the necessary cooling because the gas cools substantially upon adiabatic expansion through the labyrinth seal.

To estimate windage losses we use the model developed by NASA (Vrancik, 1968). In the Vrancik model, the frictional losses are calculated from the geometry of the rotor and the properties of the fluid, given the Reynolds number of the fluid in the gap between the rotor and the stator. The equation for the windage losses is:

$$Pwr = \pi C_d(\mathrm{Re})\rho r_{rotor}{}^4 \omega^3 L_r$$

Where C_d is a discharge coefficient that is a function of the Reynolds number, ρ is the fluid density, r is the radius of the rotor, ω is the angular frequency of the rotor, and L_r is the length of the rotor. Note that the power is directly proportional to the fluid density, the shaft speed to the third power, and to the radius of the rotor to the 4th power. This makes the actual power losses very sensitive to the shaft speed and size. Early evaluations indicate that the fractional power losses due to windage decrease as the size of the machine increases.

The Reynolds number and the discharge coefficient are defined by the equations

$$\mathrm{Re} = r_r \frac{t_{gap}\omega\rho}{\mu} \quad \text{and}$$

$$C_d = 2.04 + 1.768\ln(\mathrm{Re}\cdot\sqrt{C_d}) - \frac{1}{\sqrt{C_d}}.$$

The rotor radius is defined as r_r, t_{gap} is the gap between the rotor and the stator, and μ is the viscosity of the fluid. It is found that the discharge coefficient is not a strong function of Reynolds number, but varies from 0.01 to 0.06 (a factor of six) for Reynolds numbers that vary from 10^8 to 10^4 (four orders of magnitude), though important this term does not strongly affect the power loss. Note also that the discharge coefficient term is the only term in the equation that is sensitive to the gap width. Another

model using Taylor-Couette (Bruckner, 2009) flow could also be used could also be used to model the windage losses.

By using these equations, and the dimensions defined in Table 5.2, it is possible to estimate the power loss for the design, however some caution needs to be given. This model and correlation was developed based on measured data for air and steam. It was never intended to work with supercritical fluids. In addition, it was originally derived for laminar Reynolds number but generalized to work at high (or turbulent) Reynolds number, nevertheless comparisons with data (Vrancik, 1968) indicate that the generalizations are correct for air and steam. For supercritical CO_2 the correlations appear to provide reasonable estimates provided the local non-ideal CO_2 properties are used.

For estimation purposes, it is assumed that the rotor cavity temperature is bounded by the between the cooling water temperature in the turbomachinery housing and the compressor outlet temperature. Thus, the rotor cavity temperature is generally between the low temperature of the cooling water at 295 K and may be as large as ~320 K.

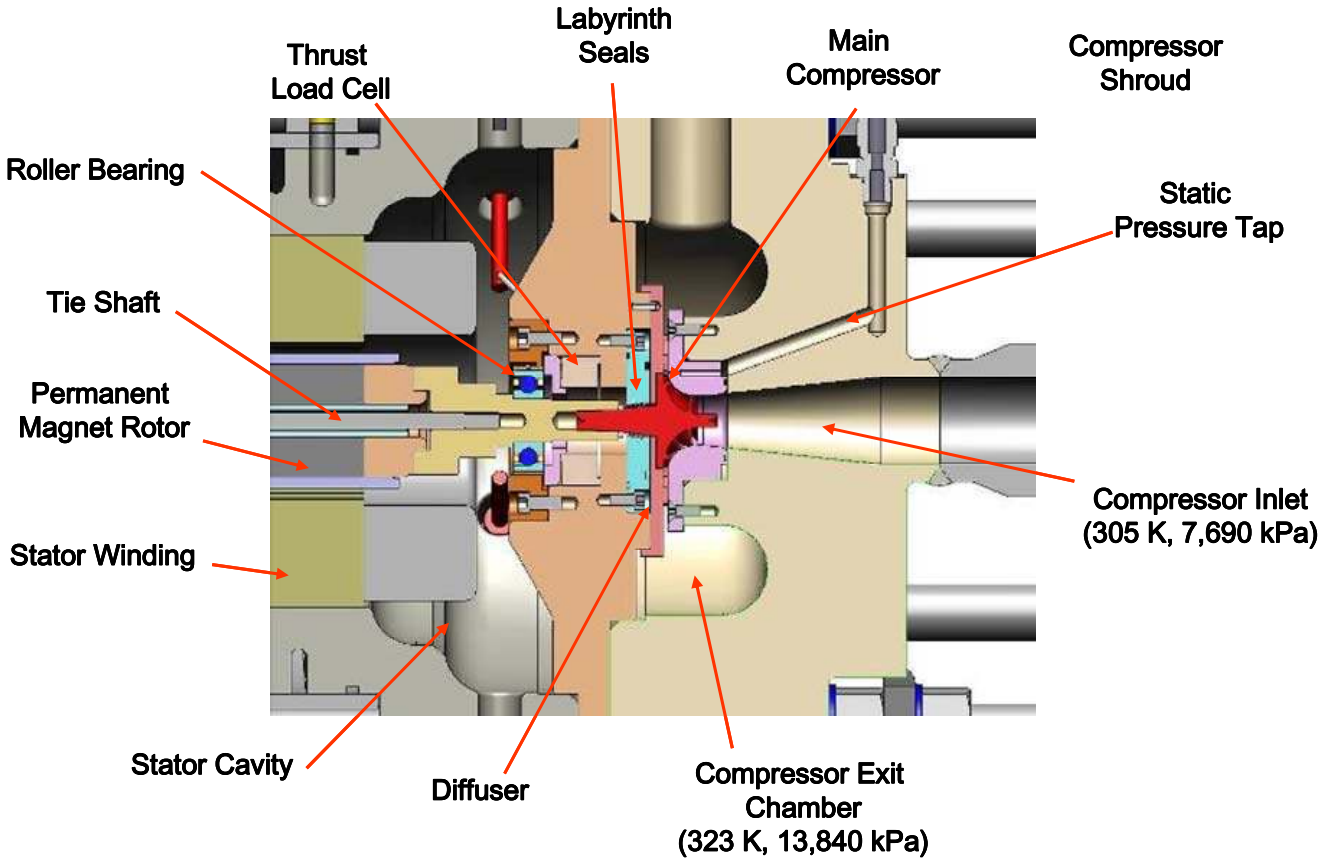

Figure 5-13: Detail of main compressor, labyrinth seals, ball bearings, and location of other major components.

Figure 5-13 shows the rotor shaft, bearings, labyrinth seal, main compressor, and the pump out port which is the opening at the bottom of the stator cavity (not labeled). The CO_2 flows from the high pressure compressor wheel outlet, past the back side of the compressor wheel, through the labyrinth seal and then into the rotor cavity. As the CO_2 expands in the labyrinth seal, it cools, strikes the bearings, then

into the rotor/stator cavity. It is possible to cool the CO_2 so much that it freezes. When this happens it is generally very difficult to start spinning the rotor shaft regardless of whether ball bearings or gas-foil bearings are used.

Table 5.2: Approximate design values for the S-CO_2 windage loss calculations.

Rotor Cavity Property	Value
Radius	25.4 mm
Shaft speed	75,000 rpm
Gap	3.175 mm
Effective length of rotor	168 mm
Viscosity of CO_2	~1.6 x 10^{-5} Pa s
Maximum density of CO_2 at (7690 kPa & 320 K)	0.213 kg/liter

Figure 5-14 illustrates the rotor windage loss and how it varies as a function of cavity pressure. Unfortunately, at 320 K (the maximum assumed cavity temperature) and 900 psia (the maximum assumed cavity pressure that is very near the critical pressure, 1115 psia), the losses are high. At these values the rotor cavity windage losses are expected to be on the order of 35 kW-40 kW, which nearly equals the capability of the motor control system and the pumping power for the compressor. Clearly, this magnitude of power loss is unacceptable. To avoid these windage losses we used a turbomachinery design that lowers the rotor cavity pressure.

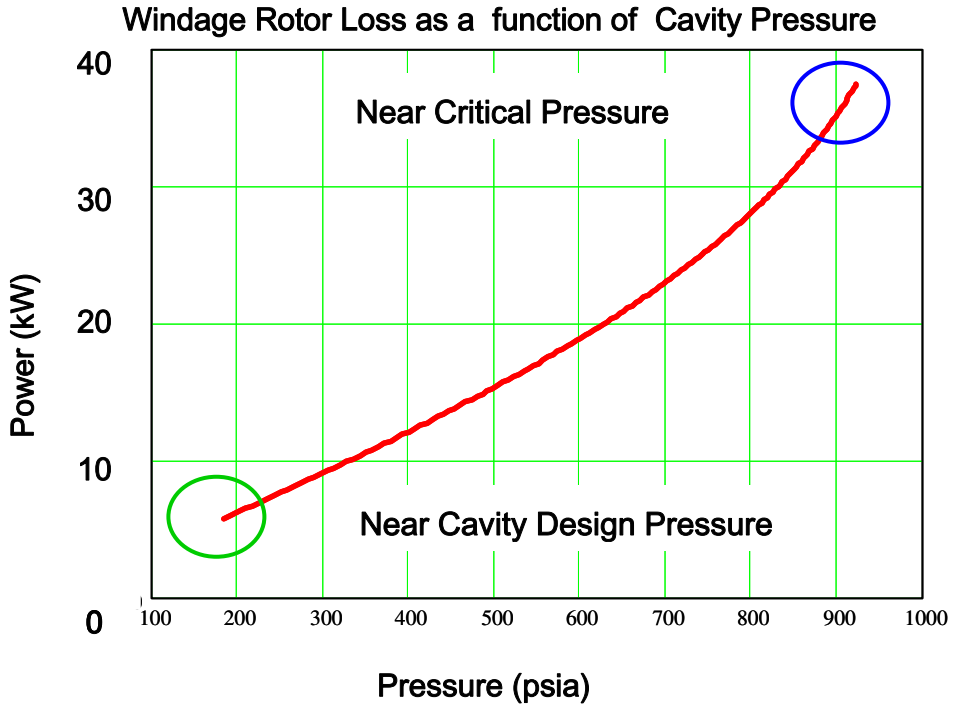

Figure 5-14: Calculated windage loss for the S-CO_2 turbo-alternator-compressor as a function of rotor cavity pressure.

These types of early scoping calculations and estimates led us to design the rotor cavity to operate at reduced pressures. At ~200 psia, when the density of the CO_2 is about 0.25 kg/liter, the windage losses are on the order of 4-5 kW. At the design operating conditions, the rotor should be producing approximately 125 kW of alternator power. This then puts the windage loss estimate at 4% of the generated power which seems to be a reasonable value for this small scale test-loop. Of course the pressure that can actually be achieved depends on the rate of leakage into the rotor cavity and the capability of the booster pump used to scavenge the gas in the rotor cavity. These effects of seal leakage flow rates are described in more detail in section 5.5.

5.4.1 Measured Windage Losses

Figure 5-15 shows the measured pressure from one test that was designed to measure windage effects. In this test the shaft speed was held relatively constant at 35,000 rpm while the rotor cavity pressure was reduced in steps from 800 psia, to 470 psia. The windage was estimated from the measured motor power minus the compressor power. The compressor pumping power was determined from the enthalpy change across the compressor times the mass flow rate. The difference between the total measured power and the compressor pumping power provide the estimate for the windage. Figure 5-16 shows the measured rotor power (cyan), and the measured estimate for the windage (magenta). The yellow line in Figure 5-16 in shows the predicted windage losses based on the model by Vrancik. As can be seen the windage is a significant fraction of the total motor power (~30 %) but that the model and measured estimate agreement is very good which simply confirms that the standard models for windage work equally well for supercritical fluids. The windage model and the windage measurement estimates were also compared to other data at higher shaft speeds, and while not quite as accurate as the data shown here, they still show reasonable agreement.

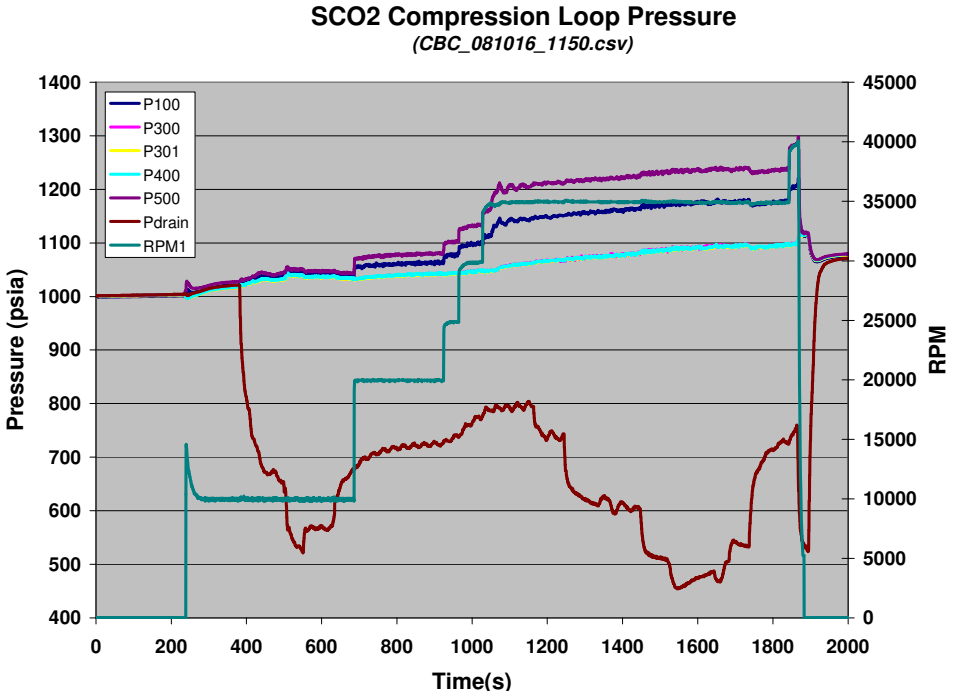

Figure 5-15: Shaft speed (rpm), rotor cavity pressure (Pdrain), inlet pressure (P400), outlet total (P500) and outlet static pressure (P100) for CBC_081016_1150.csv. This was a test to measure windage loss and thrust load at constant speed but with various rotor cavity pressures.

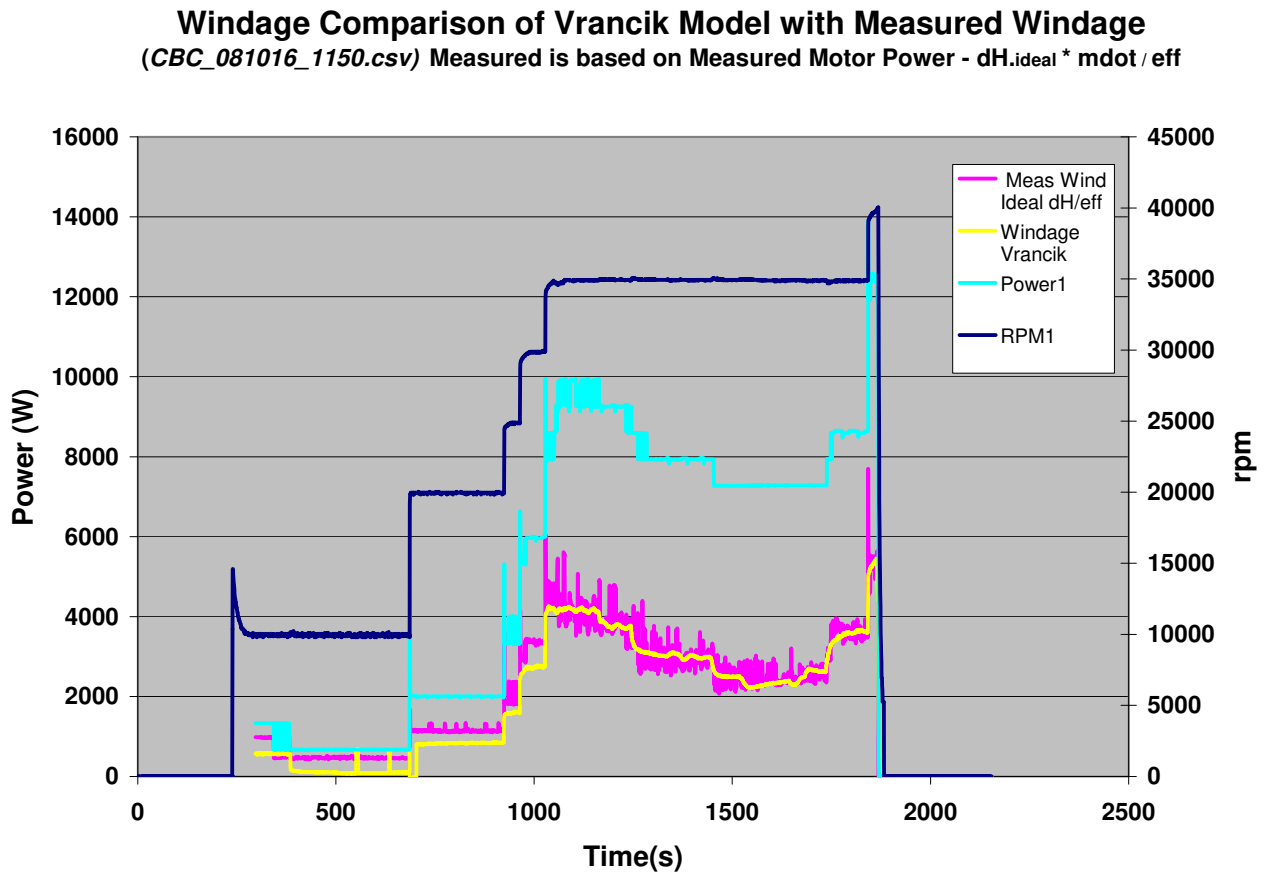

Figure 5-16: Comparison of windage estimates based on measured data (magenta) with the Vrancik model from NASA (yellow) for CBC_081016_1150.csv.

5.5 *Seal Leakage Losses*

The labyrinth seal is illustrated in Figure 5-17 A and B. The labyrinth seal uses four teeth that closely approach staggered steps in the compressor shaft to limit the flow through the seal. In the S-CO_2 turbomachinery, the design clearance between the teeth and the root of the shaft was 0.0015". Technologies other than labyrinth seals could be used. Dry-liftoff seals, which will likely have about one order of magnitude less leakage than the labyrinth seals, are the preferred choice. However, commercially available dry-liftoff seals are much more expensive, relatively large compared to the shaft diameters being used in these designs, and do not normally operate at the high shaft speed that we are using in the turbomachinery. Thus, their use would require more development than labyrinth seals. Fortunately, because the turbomachinery uses a modular design it can easily be modified to add in components that would allow for the inclusion of dry-liftoff seals at a later date. Post tests measurements of the clearance between the teeth on the labyrinth seal and the shaft indicate that the actual clearance after wear-in is .004". This unfortunately increases the magnitude of the leakage by a factor of 2.5 -3.0 above our original design values. The wear-in is believed to occur during startup when the rotor-shaft transitions through the first and second critical modes at approximately 8,000 rpm.

The leak rate through the labyrinth seals are estimated by using a correlation by Egli (Egli, 1937), or by a simpler but related correlation by Martin, (Martin, 1908). The Egli correlation was provided to SNL by Barber Nichols Inc. In addition, SNL has checked these estimates by using simple choked flow and compressible flow through orifice calculations based on formulas provided in Bird Stewart and Lightfoot (Bird, 1969) and by Martin. A discharge coefficient of 0.61 for all models. In general, the flow through the labyrinth seal is proportional to the flow area, and the upstream pressure, and density. Unfortunately due to the complexity of the turbomachinery the actual values for the seal upstream density and pressure are uncertain.

Figure 5-17 shows a detail of the compressor wheel and the location of the labyrinth seals. At operating conditions, the compressor inlet pressure is ~1120 psi (~7690 kPa), but the exit pressure can be as high as ~2007 psia (~14,000 kPa). The pressure on the back face of the wheel is uncertain, but for the purposes of bounding the leakage flow estimates, we have assumed that it equals the compressor exit pressure and temperature which are typically 324-325 K and 2007 psia. In actuality, the upstream pressure could be significantly smaller than this because the pump-out vanes on the back face of the compressor wheel are provided to approximately reproduce the pressure profile that exists along the front face of the wheel (this is done to balance the thrust load). Thus, the actual pressure will likely be much lower than the full 2007 psia. An analysis by Vernon (unpublished) indicates that the pressure at the entrance to the labyrinth seal is actually closer to the compressor inlet pressure than to the outlet pressure. As will be shown in the figures below, this lower upstream pressure greatly reduces both the leakage flow rate and the subsequent pumping power.

Table 5.3 reproduces the originally estimated leakage flow rate that was provided to SNL by Barber Nichols Inc. This calculation is based on a 1937 correlation by Egli (see, Egli, 1937) where the leakage rate of steam was measured through multiple stepped labyrinth seals. Based on this correlation, the labyrinth leakage is estimated to be 0.154 lb/s or ~0.068 kg/s. This flow rate is only 2% of the total mass flow rate of 3.53 kg/s. The SNL estimates are shown in the bottom portion of Table 5.3 for these same operating conditions. Note that the leakage flow rates estimates of 0.088 and 0.077 kg/s agree fairly well with the Egli correlation leakage flow rate of 0.068 kg/s. For comparison purposes, the last two columns show what the leakage flow would be for an upstream seal pressure of 7700 kPa (~1120 psi) rather than 13,842 kPa. The mass flow rate for these two cases is 0.032 kg/s assuming choked flow which is about two to three times less flow rate than for the higher upstream cavity pressure. Overall, it appears that the leakage flow rate through the labyrinth seals is on the order of 1-2% (per seal) of the total mass flow rate, and is most strongly dependent on the upstream pressure at the seal.

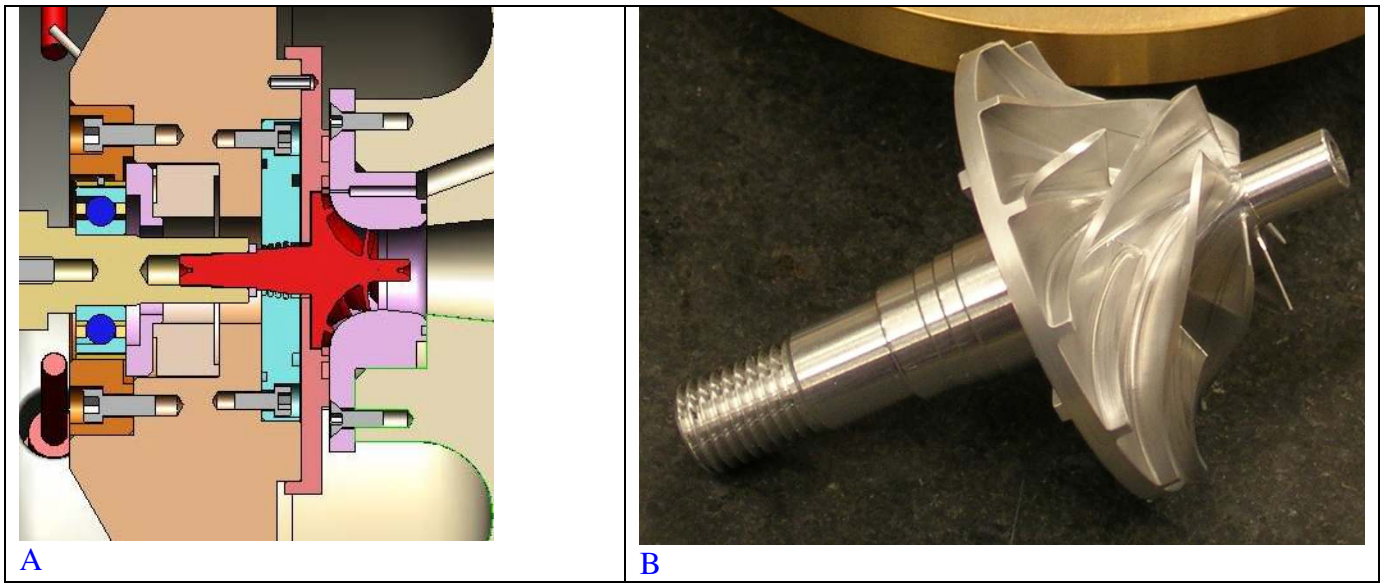

Figure 5-17: The left image shows an engineering blow up of labyrinth seal. The light blue ring in made of brass and has four teeth that approach the steps on the rotating shaft. The right image shows a photo of the compressor wheel and the four steps on the shaft.

Table 5.3: Estimate of labyrinth seal leakage flow rate using the Egli correlation provided by Barber Nichols.

Property		Value	Units
Land thickness	thick	0.02	
INPUT	Symbol		
Upstream pressure	Po	2007	psia
Upstream specific volume	vo	0.025	ft^3/lb
Down stream pressure	Pdown	200	psia
Radial clearance, small delta	clear	0.0015	inch
Diameter of seal	Dia	0.55	inch
Axial space between lands	space	0.05	inch
Number of lands	n	4	
Staggered 1=yes, 2= no	YorN	1	
OUTPUT			
Leakage area	A	0.002592	
clearance/spacing	ratio	0.075	
leakage	G	0.154463	lb/sec
leakage in scfm (of air) units		123.5708	cfm

Haskel pumps are used to reduce the cavity pressure. These pumps use compressed air to reduce the rotor cavity pressure and then discharge the compressed CO_2 back into the loop. The flow path was illustrated earlier in Figure 2-6. The pumping power is determined by the leakage mass flow rate multiplied by the change in enthalpy required to pump the fluid from 200-300 psia to the return pressure which is approximately 1120 psia. Of course this enthalpy change depends on the inlet temperature to the Haskel

gas booster pump and the pump efficiency. The maximum Haskel pump inlet temperature is estimated to be 320 K, but could be substantially different depending on the amount of cooling provided to the housing and whether or not the rotor cavity is heated by magnetic losses. For the purposes of determining the Haskel pump pumping power, the pump inlet temperature is bounded by the lowest inlet temperature available which is 295 K (approximately the cooling water inlet T) and by our estimate for the highest temperature which is 320 K. The pump efficiency is estimated to be 85%.

The pumping powers that were estimated for our design and scoping calculations, prior to operating the turbomachinery, are shown in the green row of Table 5.4. For a Haskel pump inlet temperatures of 320 K and for the largest leakage (choked flow conditions) and at an upstream pressure of 13,842 kPa, the pumping power was 12.24 kW. If the upstream pressure were 7,700 kPa, the pumping power would be 4.5 kW at 320 K and 4.3 kW at 295 K. To realize a pump inlet pressure of 295 K, the cavity leakage flow would have to be cooled by the water cooling system.

We have also estimated the mass flow rates and pumping powers at the maximum up stream pressure of 13,842 kPa, but at elevated temperatures that vary from 325 K to 360 K. These results are illustrated in Figure 5-18. As just shown, there is considerable variation in the estimated leakage flow that varies from a low of 0.032 kg/s to a high value of 0.88 kg/s. The pumping power depends greatly on upstream pressure conditions, but also on the pump inlet temperatures. All of these values were unpredictable early in the program when the design decisions were made, hence the design was based largely on bounding estimates using the tools and correlations just described. This just points out the need to measure these leakage results, which was some of the very first test that was performed on the compression test-loop.

In summary, the leak flow rates for this small scale proof-of-principle S-CO_2 test loop are on the order of 1-2% of the total compressor mass flow rate per seal. However, because the pumping powers are relatively large (12 kW – 4 kW) there is a strong need to include features that reduce the pumping power such reducing the leakage flow rate by using better seals, or by pre-cooling the leakage flow prior to compressing it back into the loop. However, because of large uncertainties in the operating conditions the actual leakage rates need to be measured.

It is also worth pointing out that this compression loop has only one compressor and one labyrinth seal. In later loops, the loops will have up to two compressors and two turbines with each wheel having a seal. Thus, measuring and understanding these loss mechanisms and developing good rules to scale these results to larger systems is important. Fortunately, based on our current understanding of the leakage flow for these designs, we expect that the fractional pumping power for large commercial systems to be much smaller than for this proof-of-principle test-loop, largely because more conventional sealing technologies can be used. Another reason is that in a larger system the generated power will grow as the radius squared, while the leakage flow rate grows proportional to the radius, thus it will be much easier to keep the fractional windage losses low in these larger systems.

Table 5.4: Estimated leakage flow rate through the labyrinth seal and pumping power. Third to last Column compares BNI/Egli at 13842 kPa with SNL choked flow results (near bottom of column). For comparison, the SNL choked flow leakage flow is shown at an upstream pressure of 7700 kPa, with pumping powers for Haskel pump inlet temperatures of 320 and 295 K.

Leakage Flow Rate Estimates through Labyrinth Seals			Egli (BNI)	SNL @ 7700 kPa	SNL @ 7700 kPa
Leakage Flow Rate (Egli)	**mdot.leakage**	**kg/s**	**0.068181818**		
Rotor Cavity Temperature	T.rc	K	**320**	**320**	**295**
Rotor Cavity Pressure	p.rc	kPa	1379	1379	1379
Enthalpy of rotor Cavity	H.rc	kJ/kg	514.0282014	514.0282014	490.213375
Efficiency of Haskel Pump	eff.HP (Haskel Pump)	-	0.85	0.85	0.85
Exit Pressure of HP	P.exit	kPa	7700	7700	7700
Temp of HP exit	T.out.HP	K	483.8526998	483.8526998	451.382254
Enthalpy of HP exit	H.out.HP	kJ/kg	652.8451996	652.8451996	616.0237866
Pumping Power of HP (single stage)	**Pwr.HP**	**kW**	**12.24486371**	**4.527406818**	**4.103207261**
shaft radius	**r.s**	**m**	**0.006985**	**0.006985**	**0.006985**
gap	**t.gap**	**m**	**0.0000381**	**0.0000381**	**0.0000381**
Orifice Area	S.o	m^2	1.67213E-06	1.67213E-06	1.67213E-06
T.gas Upstream of Orifice			**325**	**325**	**325**
P.gas Upstream of Orifice			**13842**	**7700**	**7700**
den.o2			647.3292932	198.3421303	198.3421303
Cp.rv			0.949689484	0.949689484	0.958212819
Cv.rv			0.703613305	0.703613305	0.690452759
Gamma.rv			1.34973213	1.34973213	1.387803592
Gamma Upstream			3.686802832	2.449371612	2.449371612
Leakage Choked Flow	**mdot.CF**	**kg/s**	**0.088208677**	**0.032614211**	**0.032614211**
Leakage (Comp flow Nozzel)	**mdot.orifice**	**kg/s**	**0.077188917**	**0.029017862**	**0.029017862**
Barber-Nichols Egli Correlation	**mdot.Egli**	**kg/s**	**0.068181818**		

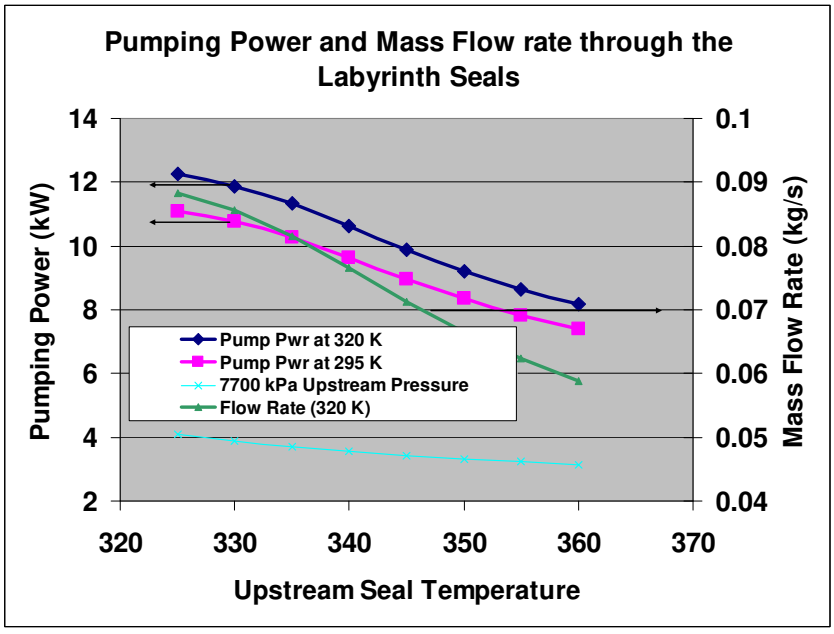

Figure 5-18: Estimated ranges of pumping powers and mass flow rates for various conditions. The dark blue and magenta curves show the estimated pumping power required to pump the fluid as a function of upstream temperature. The magenta curve illustrates the effect that pre-cooling the gas down to 295 k has on the pumping power. The mass flow rate is shown as the green curve for both the magenta and dark blue curves. However, an even larger power reduction benefit can be achieved if the pump-out vanes reduce the upstream labyrinth seal pressure to the comp inlet pressure of 1115 psi versus the exit pressure of 2007 psia. In this case the pumping power could be as low as 3-4 kW.

5.5.1 Measured Labyrinth Leakage Flow Rates

The previous section described some of the estimates that were made to determine leakage flow rates and to estimate windage losses prior to manufacturing the loop. This section describes the results from a test that measured the actual leakage flow. In this test (CBC_081201_1420), the shaft speed was varied in steps from 10,000 rpm to 40,0000 rpm while the rotor cavity pressure was held nearly constant at ~500 psia, see Figure 5-19. (A similar tests to 65,000 rpm was also performed.) In these tests an Endress+Hauser ProMass 83M Coriolis flow meter was used to directly measure the leakage flow rate that was scavenged by the gas booster Haskel pumps. Figure 5-19 shows that the compressor inlet pressure (P400, cyan curve) varied from 1050 - 1100 psia while the gas rotor cavity pressure (Pdrain) slowly changing from 500-580 psia (brown curve).

The data in Figure 5-19 plus the measured temperatures of the drain lines was used to compare the predicted flow rate with the measured flow rate. These results are shown in Figure 5-20. The measured leakage flow rate (LeakageFlow1) is shown as the brown line in Figure 5-20, and the predicted flow rate using the Martin correlation (Leakage Martin, red curve). This figure also shows the measured data, including compressor inlet pressure (P400), rotor cavity or drain pressure(Pdrain/1000), main compressor flow rate (MassFlow/10, magenta) and compressor inlet density (Density/100, cyan). Notice that the leakage flow rate is not sensitive to shaft speed. Other tests show that the leakage flow is primarily sensitive to the flow area, the inlet pressure and density, and very weakly to the rotor cavity pressure. The red curve shows the predicted flow rate using a measured 0.004" gap between the shaft and the labyrinth teeth using the Martin correlation though other correlations would work equally well (Egli16, and Vermes17). The agreement is reasonable, and would only require a small increase in the gap thickness to predict the observed value. (Similarly a small change in the upstream pressure to the orifice would also increase the predicted flow rate.) At this time the oscillations in the measured leakage flow rate are not understood, but it is believed to be caused by fact that the flow meter is measuring a two-phase fluid.

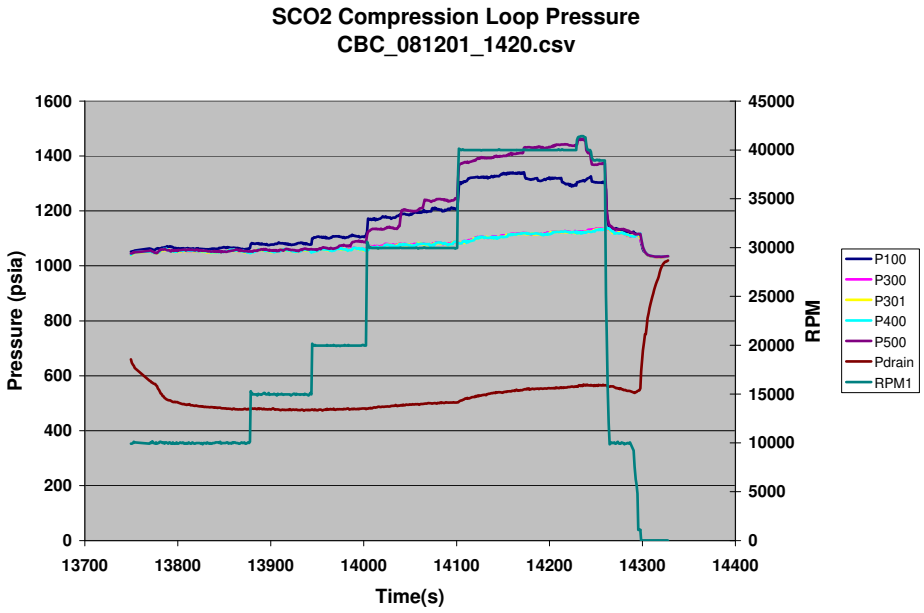

Figure 5-19: Measured pressures and shaft speed in compression loop test CBC_081201_1420. The test was designed to measure leakage flow rates and thrust load as a function of shaft speed for near constant rotor cavity pressure (Pdrain).

The predicted leakage is based on the "Martin" model for non-choked flow through multiple labyrinth seals and is calculated from the following formula:

$$\dot{m} = C_d S_o \sqrt{p_1 \rho_1 \left(\frac{\left(1 - {}^{p_2}/_{p_1}\right)^2}{N - \ln\left({}^{p_2}/_{p_1}\right)} \right)}$$

S_o is the flow area and C_d is the discharge coefficient which is assumed to be 0.61 and N is the number of teeth (four) in the seal. The leakage is on the order of 0.2 lb/s per seal. The designed flow rate is 7.7 lb/s so the leakage is on the order of 3% per seal in this test.

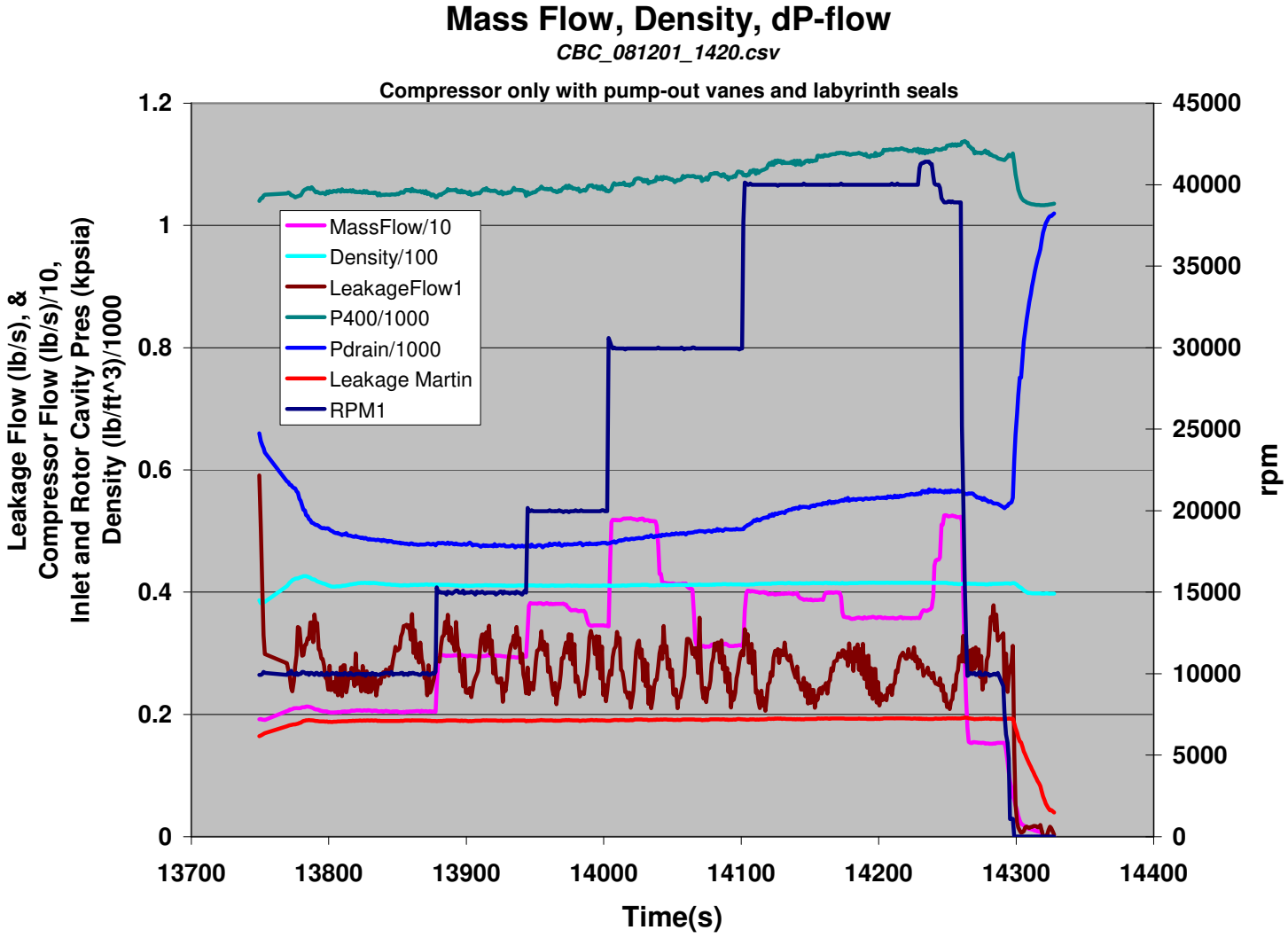

Figure 5-20: Measured (brown) and predicted (red) leakage flow rate through the four tooth labyrinth seal.

5.5.2 Gas-Foil Bearings

As previously described the early turbomachinery for the compression loop used ball bearings. However, because of the limited bearing life, the design also included the option to operate with gas-foil bearings. A

second rotor shaft (see **Figure 2-5**) was built to work with the gas-foil bearings. Both journal bearings and thrust load bearings are required. Photos of the bearings that were installed in the turbo-compressor are illustrated in Figure 5-21. The left image shows the thrust bearings. These are standard bump foil supported Inconel pads. It is estimated that these thrust bearings can support up to 225 lbs of thrust at the design speed of 75,000 rpm. In the thrust load testing performed in the single compression loop, thrust loads were always less than 80 lbs, so the expectation is that these bearings will function properly. The right image in Figure 5-21 shows the Capstone journal bearings. Barber Nichols has an agreement with Capstone Microturbine that allows them to use the Capstone journal and thrust bearings. Barber Nichols has elected to use only the Capstone journal bearings because the thrust load capacity of the BNI bump-foil gas bearings shown in Figure 5-21 is greater than the capacity of those in the Capstone design.

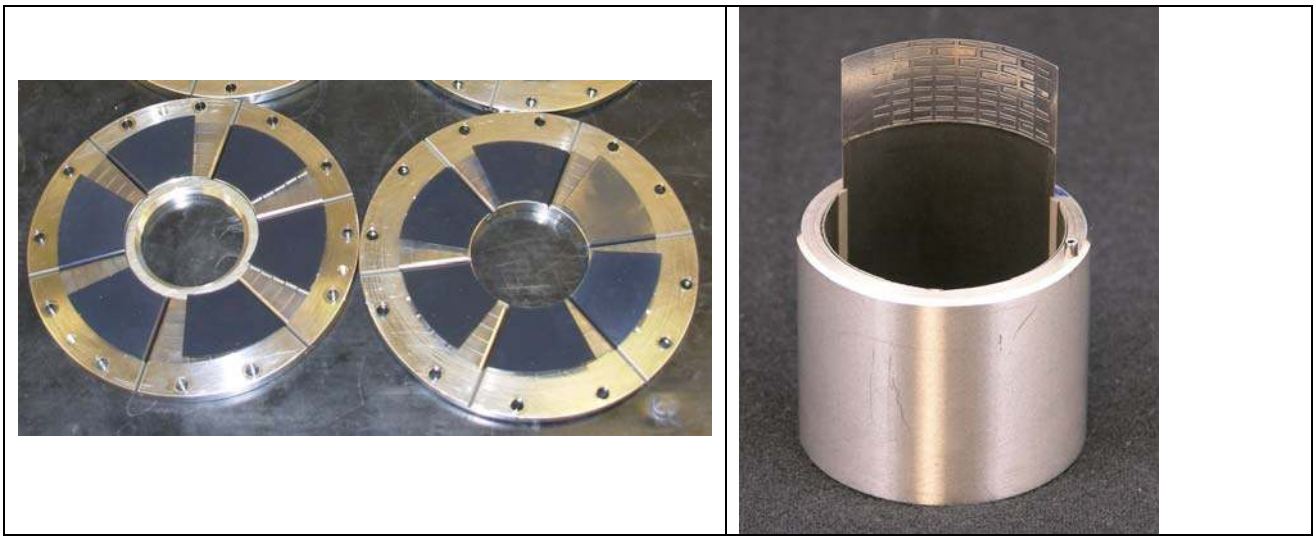

Figure 5-21: Photos of the gas foil bearings for use in the GenIV turbomachinery. The left image shows the bump-foil thrust bearings which were designed and manufactured by Barber Nichols Inc. The right image shows the journal gas foil bearings. These bearings were purchased from Capstone Microturbines.

The theory and models for gas foil bearing operation are complicated and not widely applied beyond a few experts in the field. Our analysis of the gas foil bearings is largely based on data reported by NASA Glenn Research Center by C. DellaCorte and Bruckner (DellaCorte, 2006 and Bruckner, 2009). This data suggests that the bearings are capable of withstanding 1 lb/in^2 of load per 1000 rpm. Thus, the thrust bearing which has about 3 in^2 of surface area can withstand loads of 3 in^2 x 75,000 krpm or about 225 lbs of thrust. These correlations were developed for gases at low pressure and not for high pressure CO_2.

Windage power loss models indicate that the bearing heating will be proportional to the fluid density. For this reason we have placed the gas foil bearings in the rotor cavity region where the pressure and density can be reduced to 200-300 psia (16 kg/m^3) by using scavenging pumps. At the current time we are using gas booster pumps manufactured by Haskel to reduce the rotor cavity pressure. Unfortunately, these pumps together with the labyrinth seal technology are only capable of reducing the pressure to 650-700 psia. This means that the rotor cavity has a density of about 100 kg/m^3 or 6-7 lb/ft^3 which is about 5 - 7 times more dense than desired. This also means that the frictional heating power will also be about 5-7 times greater than the design goal. Still these arguments have led us to explore the use of advanced seals

that may be able to reduce the seal leakage by up to order of magnitude compared to the stepped labyrinth seal. Several tests using a variety of seal types have been tested but are not reported here.

5.5.2.1 Gas-Foil Bearing Test Results

The gas foil bearings, (both the thrust and the journal bearings) were operated for several hours in June 2009 using the Sandia compression loop. Figure 5-22 through Figure 5-25 show the results from one test that lasted approximately 20 minutes. This test operated the gas foil bearings with the compressor on the shaft (but no turbine) at speeds of 27,000 rpm up to 40,000 rpm. Figure 5-22 shows the speed and gas bearing temperature as a function of time for this test. The shaft initially started at 27,000 rpm then increased to 40,000 rpm. The thermistors measured the gas temperature at the exit of the journal or thrust bearing as described in the previous section of this report. Btemp1 (magenta) is the compressor journal bearing temperature. Btemp2 (yellow) is the "turbine" journal bearing temperature (but there is no turbine). It was cooled by a manually controlled valve that flows a small amount of CO_2 on the bearing. The green line shows the thrust bearing temperature. As can be seen the bearing temperatures are well behaved and do not exceed temperatures the system can be operated indefinitely. The most interesting aspect of this test is that until 950 seconds the gas bearing temperatures are much cooler than the compressor inlet temperature (88-92°F). This is because the expanding CO_2 through the labyrinth seals flashes to liquid at the rotor cavity pressure of 750 psia which has a saturation temperature of 65°F. This means that the compressor thrust and journal bearings are operating on saturated CO_2 which is a mixture of gas and liquid. Until this test it was not obvious that the gas foil bearings could operate successfully on liquids, but this test confirms it. This effectively opens the operating envelop for these types of gas-foil bearings. This could have significant benefits for transients operations and for startup and shutdown transients.

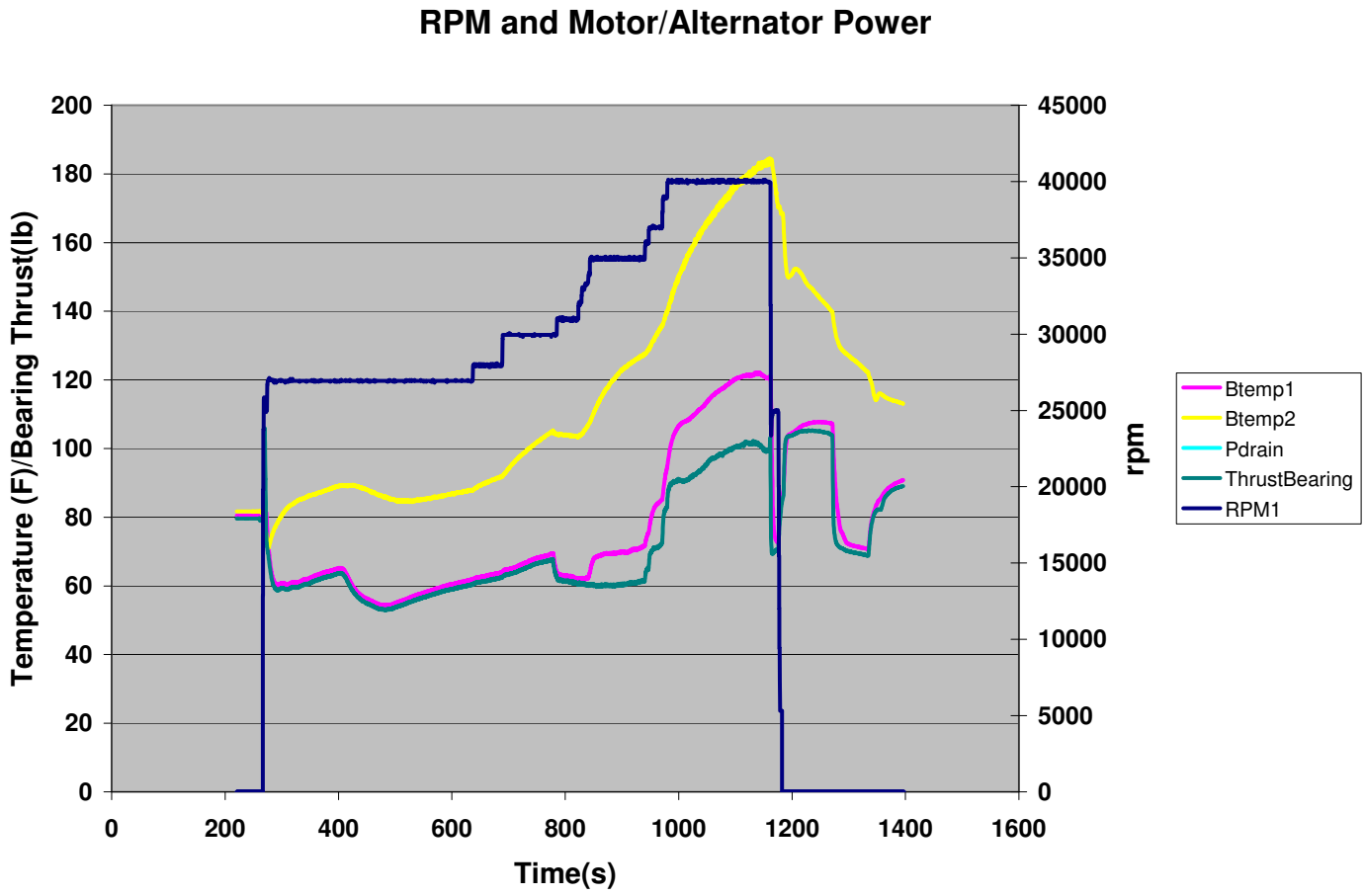

Figure 5-22: Measured gas temperature near the bearings in CBC_090626_1303.

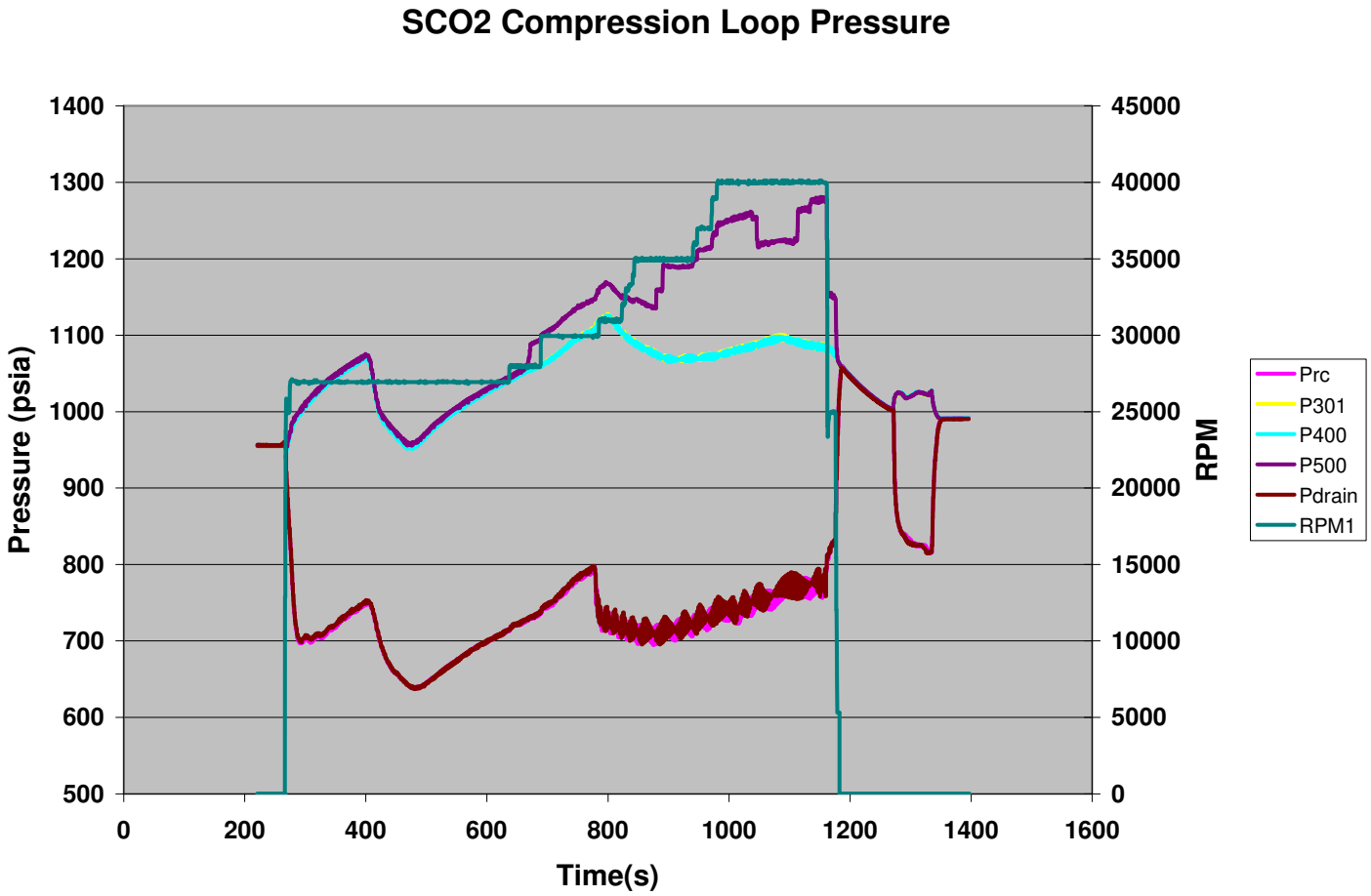

Figure 5-23: Measured pressure in gas foil bearing test CBC_090626_1303

The compression loop pressure and temperature for this same test are illustrated in Figure 5-23 and Figure 5-24, and the density and flow rate are shown in Figure 5-25. Notice that the drain temperatures approach the bearing temperatures, and that the mass flow rate through the compressor is nearly 5 lb/s with a pressure ratio of about 1.2. The oscillations in the density and flow at the beginning of the test show that the compressor was also operating in the two phase saturation conditions. This type of two phase compressor inlet conditions has been observed many times and causes no problems as the oscillation period is very slow ~ 60 seconds. It is estimated that the period of oscillation is related to the time it takes fluid to flow around the loop.

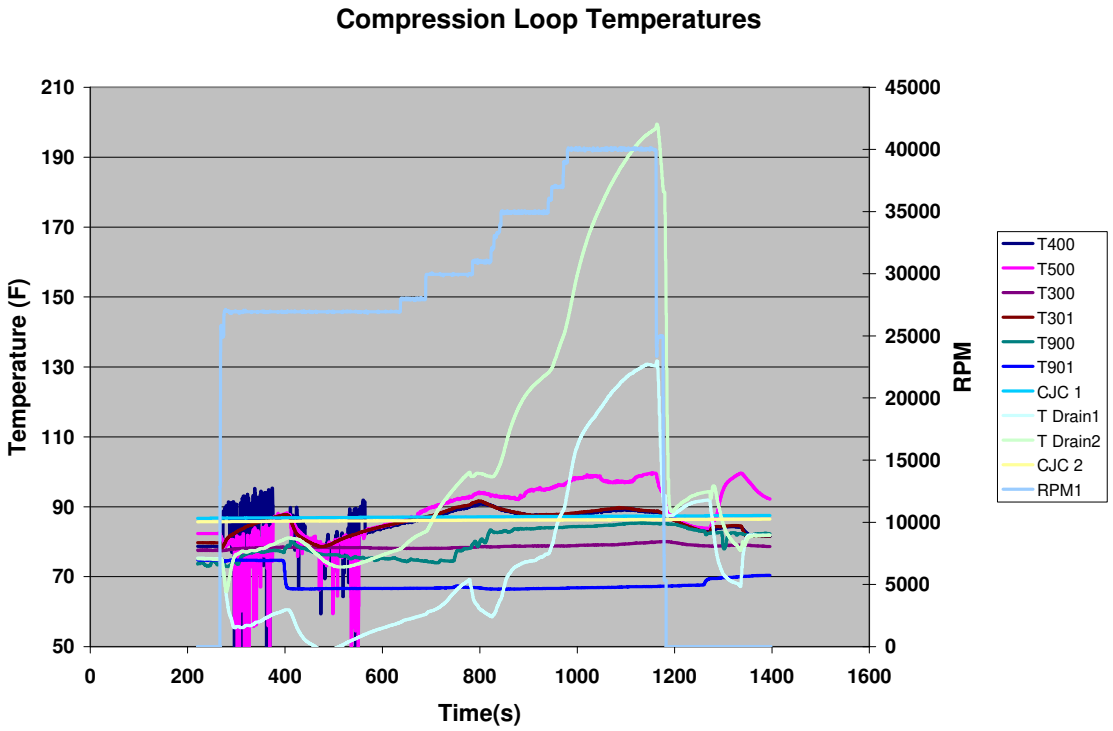

Figure 5-24: Measured loop and turbomachinery drain temperatures in CBC_090626_1303

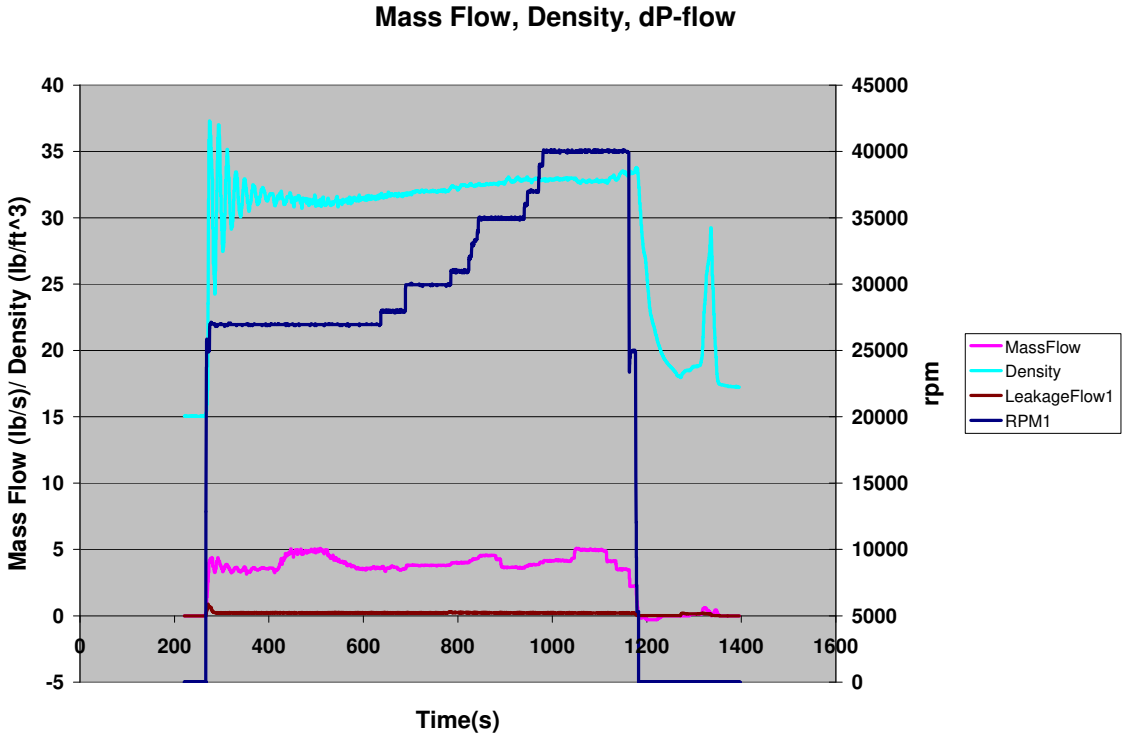

Figure 5-25: Measured density, flow rate and leakage rate for CBC_090626_1303, leakage average flow is 0.21 lb/s.

5.6 *Rotor Shaft Dynamics*

Figure 5-26 shows an engineering drawing of the rotor shaft connected to the compressor (right) and the motor-assist turbine (left). The rotor is supported by two gas foil journal bearings located near the compressor and turbine wheels. The thrust bearing is the disk that is located next to the compressor wheel. The rotor uses Sm/Co for the permanent magnet, and holds these magnets in place by using a pre-stressed Inconel 718 shroud. The rotor is approximately 2" in diameter, which makes it much larger than the diameter of the compressor wheel (~ 1.5").

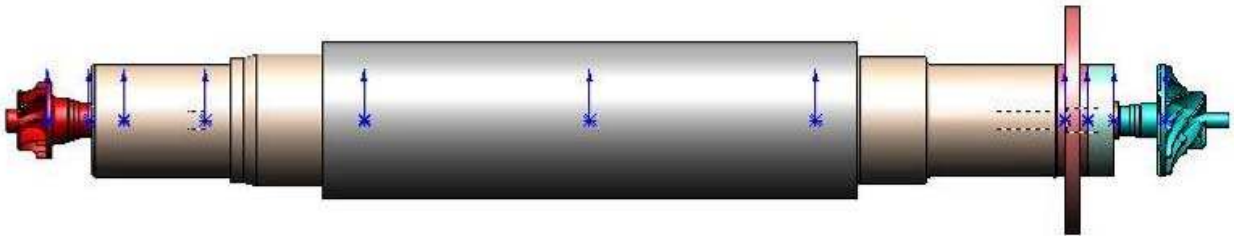

Figure 5-26: Engineering schematic of the Sm-Co Permanent Magnet rotor with gas foil journal and thrust bearings. The thrust bearing is on the right next to the compressor wheel. The moment of inertia is 7.53 lbs/in^2 in the current design. The "red" disk is the thrust bearing surface, but was increased in size to allow for greater thrust load capability and for the inclusion of magnetic thrust bearings.

Rotor dynamics were investigated for the ball bearing supported shaft and for the gas-foil bearing supported shaft. Figure 5-27 shows the discretization used to estimate the rotor dynamics with the ball bearings providing support on both ends. The stiffness of the ball bearings using flex-mounts is estimated to be about 34,000 lb/in. Figure 5-28 shows a plot of the critical speed for the first three modes of vibration as a function of bearing stiffness. For the expected design, it is seen that the shaft will be operating between the second and third fundamental modes. The first and second vibration modes are often considered to be the rigid body modes, while the third mode has two zero crossings representing the "U" shaped bending mode. The first and second modes occur at approximately 17,000 and 32,000 rpm, while the third mode does not occur until 104,000 rpm. A vibration analysis was performed to assure that the vibrations would be acceptable within BNI's ability to balance the rotor shaft. Stress strain calculations were also performed on the compressor wheel to assure that the loads imposed by the CO_2 were within limits. The peak stress levels were located in the compressor blade and were approximately 7,000 psi which is well within the limits of Aluminum 6061 T-6 from which the compressor is made.

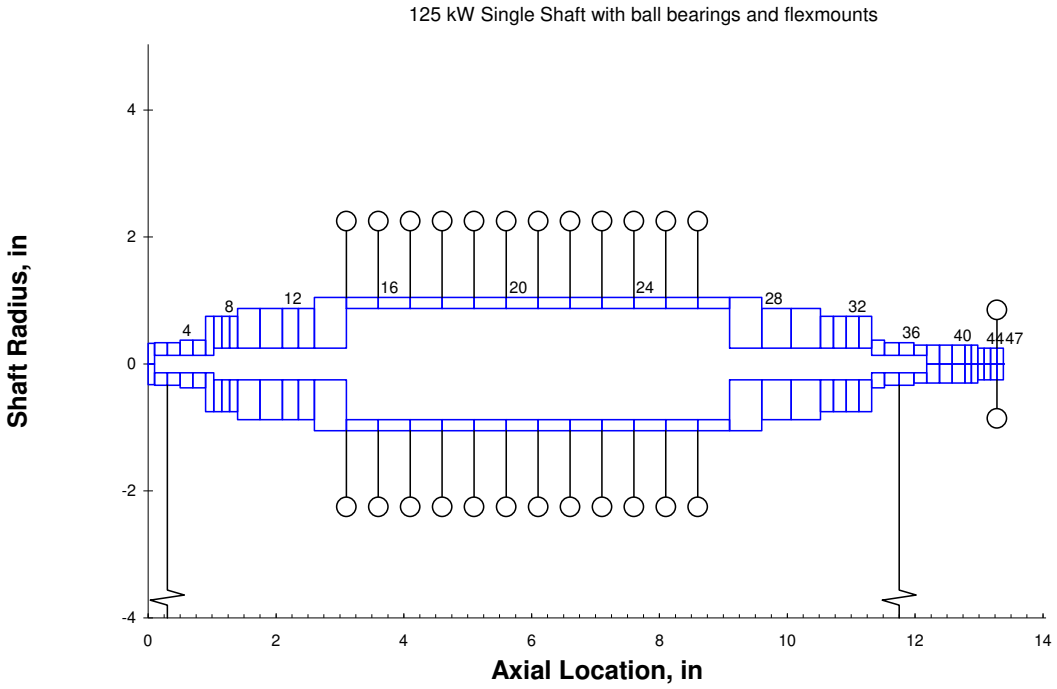

Figure 5-27: Schematic illustrating the discretization used to estimate the rotor dynamics.

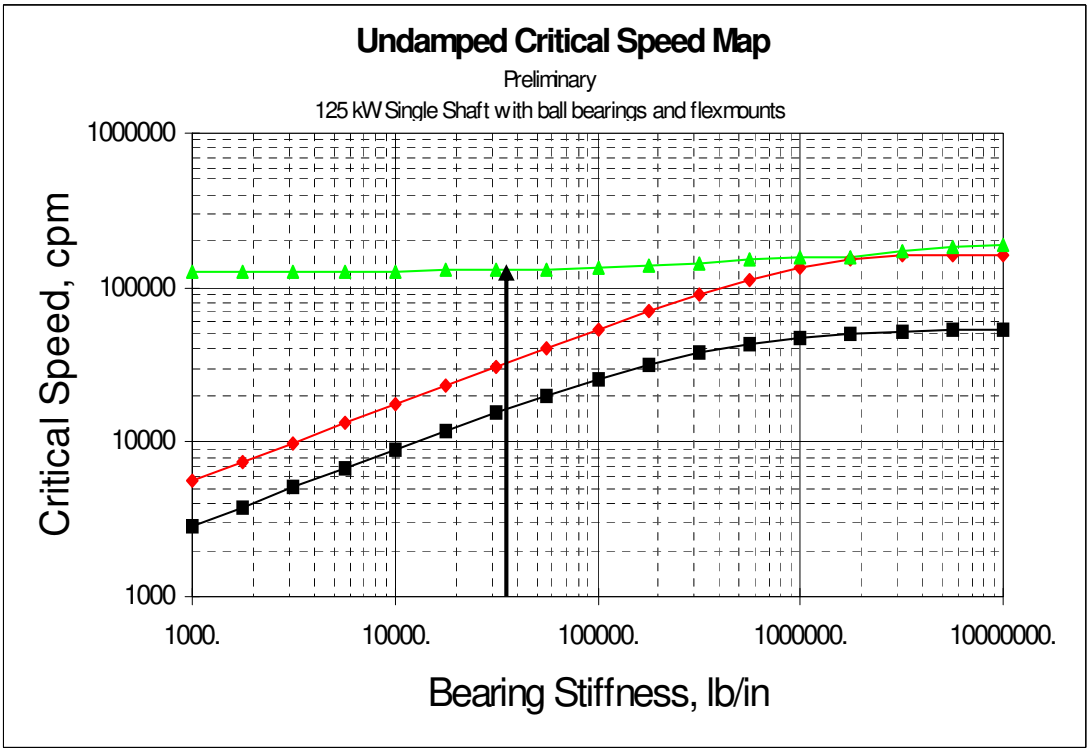

Figure 5-28: Critical speed map showing revolutions per minute for the first, second and third fundamental modes of vibration as a function of bearing stiffness. The ball bearings are mounted on flex-mount material that is estimated to have a bearing stiffness of 34,000 lb/in. At 75,000 rpm the rotor shaft is between the 2nd and 3rd fundamental mode. Note that the idle speed should be above 40,000 rpm. Also during startup the rotor shaft should accelerate rapidly through the 1st and 2nd fundamental modes at 17,000 and 32,000 rpm respectively.

5.7 *Thrust Load Balancing*

The total axial thrust on the shaft must be accommodated by a thrust bearing. Figure 5-29 conceptually illustrates the pressure along the front and back surface of the compressor wheel. Because the pressure in the S-CO_2 loop is high, the thrust on the back face of the bearing can be substantially different than the thrust from the front side of the wheel. In the worst case, the back face can have an average pressure that is approximately 500-1000 psia greater than the front face pressure. Even though the wheel is small, an average differential pressure of even 500 psia across the wheel area of 1.5 in^2 can result in 750 lbs of thrust force.

In the compression loop design, pump-out vanes are provided on the back surface of the wheel to balance the thrust that is on the front face. These pump-out vanes act as a small compressor and attempt to match the pressure profile that exists on the front face. The height of the pump-out vanes can be trimmed to reduce the pressure that they create. However, the exact back face pressure profile is uncertain and in addition varies over the full operating range of the compressor. For these reasons, the motor-driven compressor was designed so that a load cell can be installed to measure the thrust loads. Initially, the height and size of the pump out vanes have been adjusted to approximately balance the force on the wheel, but it is arranged to push toward the inlet of the compressor. This will allow BNI to measure the thrust and therefore in a few attempts trim the height of the pump-out vanes so that the net force is zero. Large deviations in thrust load and misalignments will cause the bearings to burnout, rub against the shroud or labyrinth seal and damage the compressor wheel. This is the reason why nine compressor wheels were fabricated as illustrated in Figure 5-30. A similar approach will be used for the turbine, however, cutouts rather than pump-out vanes were used.

For the initial S-CO_2 motor-driven compressor the ball bearings are capable of supporting up to 1000-2000 lbs of thrust load. The lifetime of the bearing is dependent on the magnitude of this load, and at these loads, the lifetime is at most only 10-20 hours. However, this is sufficient time to allow for the bearing thrust load to be measured and then trim the pump-out vanes. Once the thrust load were balanced and found to be within the capabilities of the gas-foil bearings, the ball bearings were replaced with the gas-foil bearings (both journal and thrust).

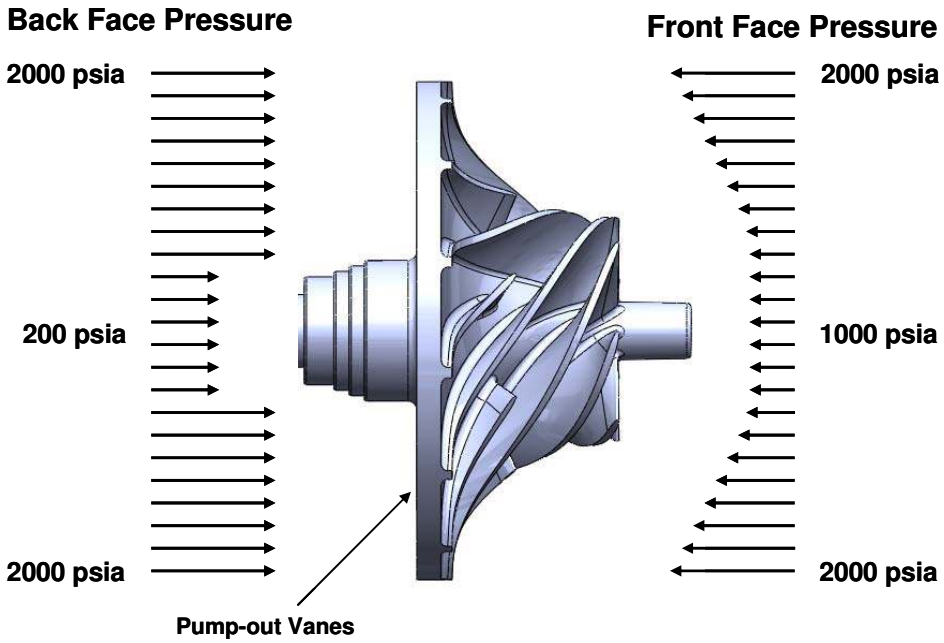

Figure 5-29: Illustration of thrust load balancing. For the wheel to be thrust load balanced the integral of the pressure times the area on the front face must equal the pressure times the area on the back face.

Figure 5-30: Multiple compressor wheels are provided to allow for several attempts to balance the thrust load. The pump-out vanes that are on the back of each wheel are shown. The height of the pump out vanes can be trimmed to reduce the load on the compressor wheel.

5.7.1 Measured Thrust Loads

Thrust load was measured by using the load cell that was installed in the motor-driven compressor (see Figure 3-1). The axial thrust was designed to be taken by the ball bearings which were configured in a back-to-back thrust bearing arrangement but is backed only by a spring loaded load cell. This means that the bearing on the turbine side of Figure 3-1 prevents the shaft from moving to towards the turbine while the bearings on compressor side are limited only by the preload applied to the load cell. The load cell can be placed on either the turbine or the compressor side, but it only measures the load in one direction. BNI expected the loads to push towards the compressor; therefore the load cell was initially set up to measure loads up to 500 lbs in this direction. However, the thrust loads at 55,000 rpm were limited to about 75-90 lbs, but the thrust was towards the turbine side. To measure this thrust the load cell had to be moved to the turbine side. This value of thrust (75-90 lbf) was sufficiently small that it falls within the expected gas bearing thrust load capability (~225 lbs).

As illustrated in the previous sections one test varied the shaft speed in steps from 10,000 rpm to 40,0000 rpm while the rotor cavity pressure was held nearly constant at ~500 psia, see Figure 5-19. This test was used to develop shaft thrust load models, but was also used to illustrate the labyrinth seal leakage flow rate models.

The measured and predicted thrust values are shown in Figure 5-31. The measured thrust is towards the rotor cavity (or towards the turbine end of the shaft) and is seen to be on the order of 100 lbs, and it is slightly shaft speed dependent. The magnitude of the thrust is judged to be low enough to allow the use of gas foil thrust bearings. The model for thrust uses the geometry of the compressor wheel, the shaft speed, the mass flow rate and the leakage flow rate, plus an assumed slip coefficient to estimate the gas velocity to predict the static pressure rise on the front and back face of the compressor. The static pressure is integrated with the area of the compressor to determine the axial thrust. In Figure 5-31, the slip coefficient is fit to the data, hence we see very good agreement. The slip coefficient is a very weak function of shaft speed (on the order of 75%). However, this same model, when used on other tests, provides reasonably good predictions of the thrust load. At the current time the model is quite simple but the results appear to provide reasonable estimates or the thrust. Because there can be many hundreds to a thousand of pounds of force across the front and back face of the compressor the model must subtract two very large numbers to find a total thrust that is near zero. This also makes it difficult to predict the direction and magnitude of the thrust. This is an area of future research and measurement, and further reports are expected in this area.

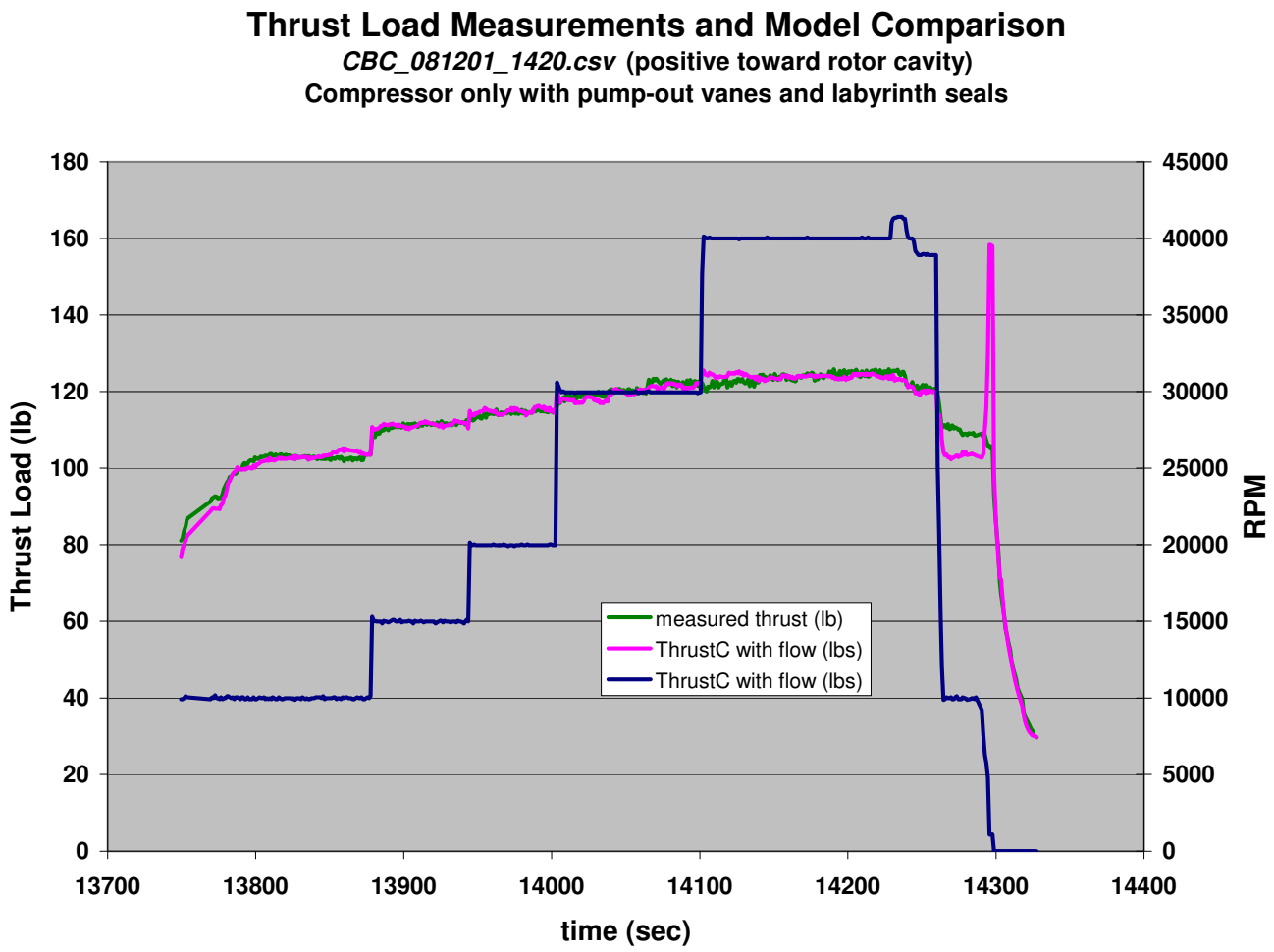

Figure 5-31: Comparison of measured thrust (green) and modeled thrust (magenta) with shaft speed as well.

5.8 *Heated Un-recuperated Brayton Loop Results*

In December 2008 after the first set of compressor mapping studies, the compression loop was substantially reconfigured by adding heaters and a small turbine. Figure 5-32 shows a schematic flow diagram of the reconfigured "heated but un-recuperated" Brayton loop. The instrumentation naming convention (e.g. T100 or P100) for the temperature and pressure measurements is also illustrated. Figure 5-33 and Figure 5-34 show photos of the heated but un-recuperated Brayton loop. Figure 5-33 shows the two 130 kW heaters in the foreground with the rest of the loop in the background, while Figure 5-34 shows a close up of the TAC with the piping to the heaters and the flow return to the turbine. The turbomachinery uses a turbine with a 1.215" (30.8 mm) OD and a compressor with a 1.471" (37 mm) OD. Figure 5-35 shows photos of the turbine and nozzle along with the compressor and diffuser. The main-compressor shaft used ball bearings, and stepped labyrinth seals were used to isolate the rotor cavity volume from the compressor and turbine. Air driven Haskel gas booster pumps are used to reduce the rotor cavity pressure to control the windage losses. The shaft has a load cell that is placed on the compressor side of the TAC which allows one to measure the thrust load towards the compressor. In

February 2009 the load cell was moved to the turbine side so it could measure the thrust towards the turbine.

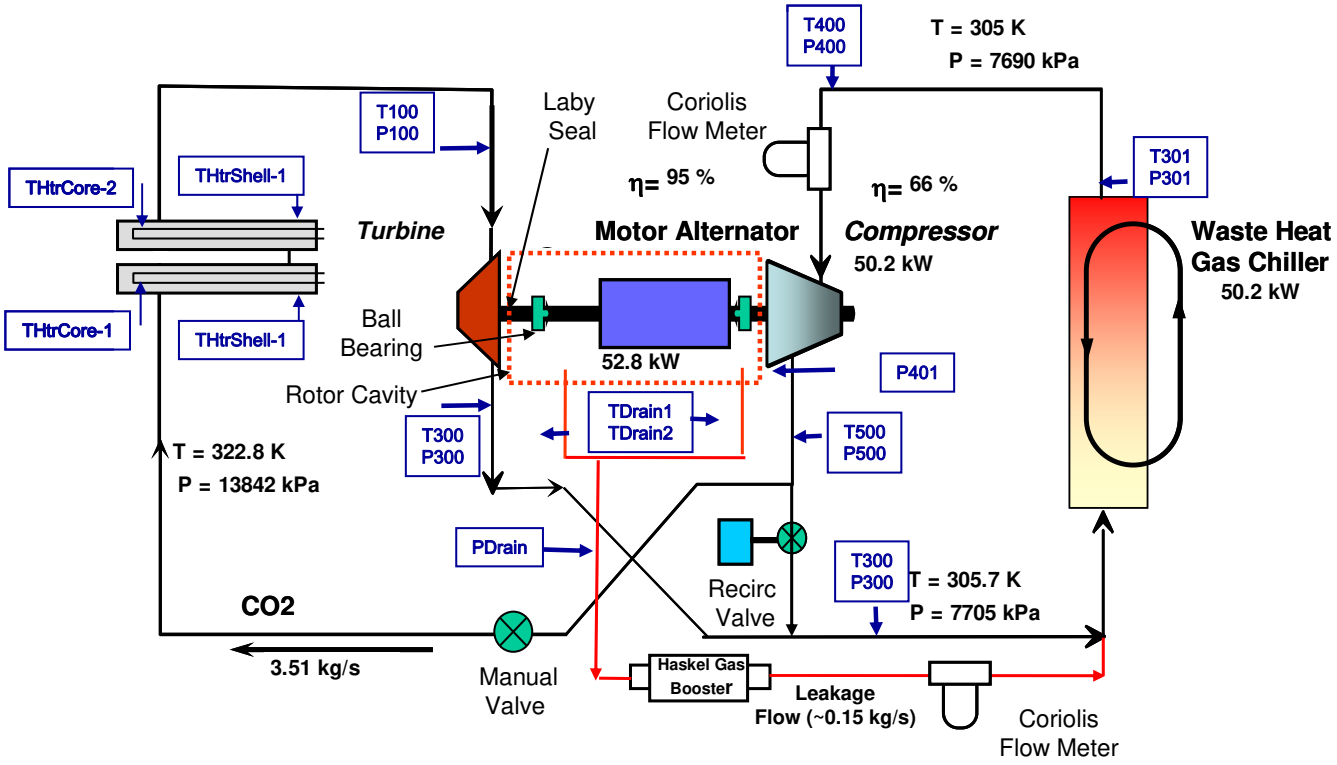

Figure 5-32: Simple diagram of the heated un-recuperated supercritical CO_2 Brayton loop.

In addition, the loop is configured with two isolation valves. In the normal mode of running, the heater isolation valve is open, while the recirculation valve is fully closed. In this configuration the flow is forced to go through the heaters and turbine resulting in a simple Brayton cycle configuration. However, in a separate configuration, the heater isolation valve can be closed to force the flow to bypass the heaters and turbine. In this configuration the CO_2 flows directly through the main compressor, through the Main-Compressor-Flow-Valve (MCFV), and then directly to the gas chiller. The MCFV is a V-ball valve and can be partially opened or closed by using a motor. This provides the ability to vary the compressor pressure ratio while at constant rpm, and thereby measure the compressor performance map. Note however, that in this compressor mapping configuration the turbine is still attached to the shaft, thus it is churning in stagnant CO_2 which introduces more losses.

Figure 5-33: Photograph of the heated but un-recuperated S-CO_2 Brayton loop. The foreground shows the two 130 kW (each) heaters. The turbo-machinery test skid is shown in the background. The display for the data acquisition and control system is shown on the cart.

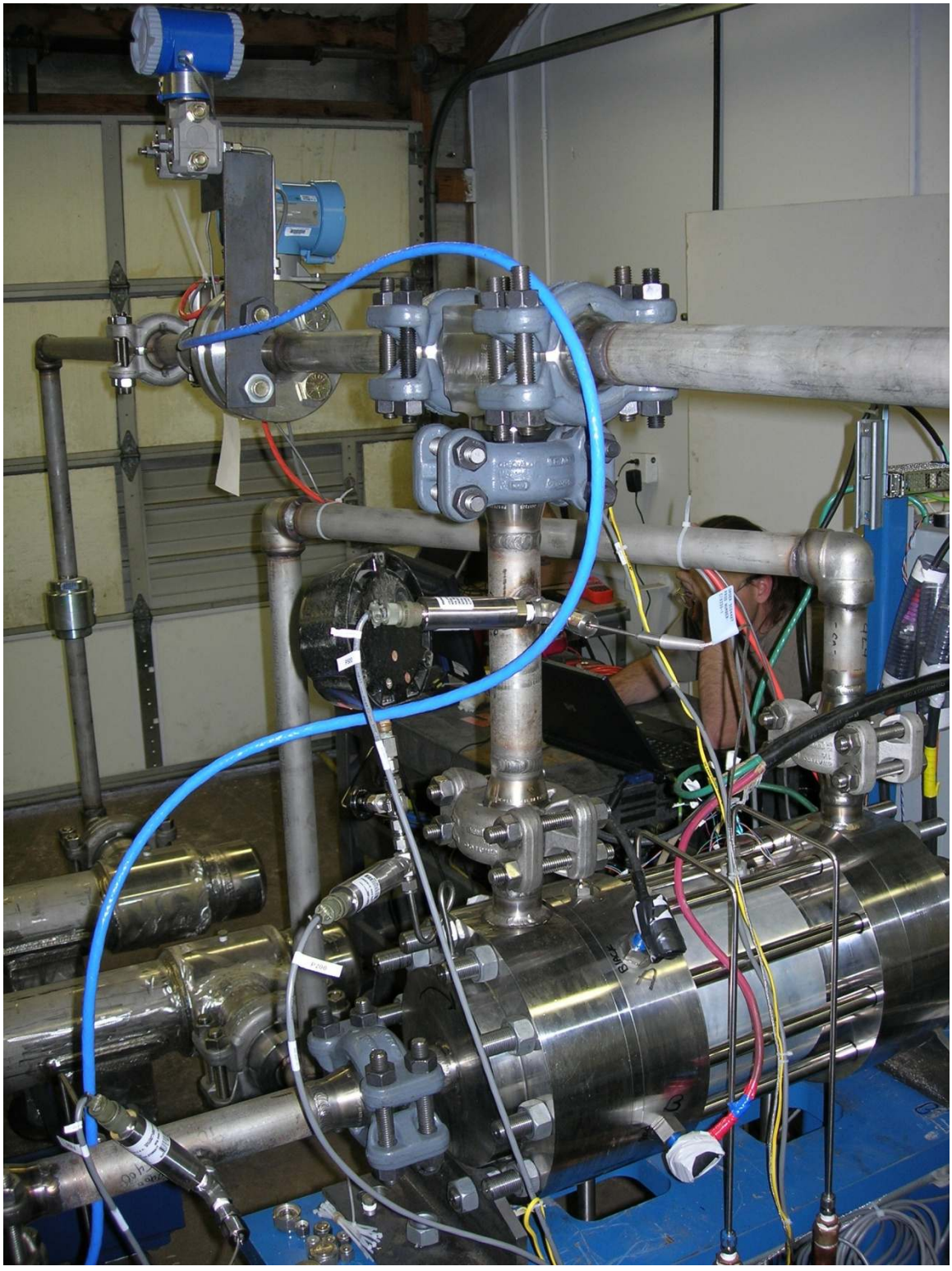

Figure 5-34: Close up view of the turbo-alternator-compressor (TAC) for the S-CO_2 Brayton loop. The compressor is on the left. The turbine is on the right side of the TAC.

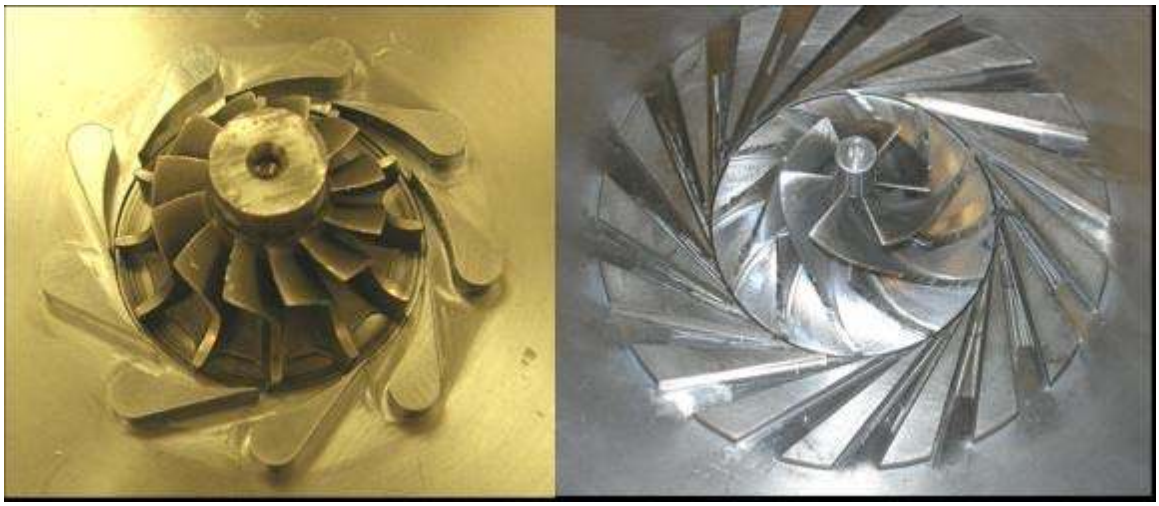

Figure 5-35: Photo of the 1.215" OD turbine and nozzle (left) and the 1.471" OD compressor with its diffuser (right).

5.8.1 Test Series Description

Four types of tests were performed in the heated but un-recuperated Brayton cycle (Wright, 2009c). The first series of tests measured the leakage rate through the labyrinth seals. The second set of tests recorded the heat up process to illustrate the behavior of the loop as the supercritical conditions are being approached. The heat up process uses a combination of heating only and spinning plus heating to reach the supercritical conditions. During much of the heat up phase the turbomachinery is operating at saturation conditions. Thus on a T-S plot, the operating points appear to be on the liquid-vapor saturation curve (or dome). The third type of test that was performed was a compressor performance mapping test (Noall, 2008 and Wasserbauer, 1975). As described earlier, the heater isolation valve was closed for these tests and the heaters were not operated, except during preheat. The last and fourth test was a near steady-state operation at 78 kW of heater power. A brief description of each of these test results is provided below.

5.8.1.1 Labyrinth Seal Test

The labyrinth seal testing showed that the leakage rates with a turbine and a compressor were approximately twice those measured for the compression loop testing alone. The leakage is twice the compressor-only-leakage, because there are two seals. Typical leakage rates were on the order of 0.35 lb/s of flow. One of the tests used a wind-back labyrinth seal design. This leakage data has not been fully analyzed to date.

5.8.1.2 Preheat Testing

The second test sequence consisted of the preheat phase and the approach to the critical point. The preheating data can be broken into two phases, heating without spinning and heating with spinning. With no spinning all the pressures in the loop are the same, but the densities can change based on the local temperature. Generally the coldest temperature in the chiller an on a T-S diagram this point is on the

vapor-side of the saturation curve for the fill conditions in this test. (Note that higher fill densities could place this point on the liquid side of the saturation curve as well.) While spinning, at low shaft speeds, we observed density fluctuations. These appear to oscillate between the liquid to the vapor side of the saturation curve. The oscillations are seen in both the measured density at the compressor inlet, and in the predicted densities (based on T and P measurements). The oscillations are very slow and seem to correspond with the time it takes fluid to flow around the loop (~15 s). As the critical point is reached the magnitude of the density oscillations diminished, until the loop is operating above the dome when oscillations were no longer observed.

5.8.1.3 Compressor Mapping Test

The compressor mapping tests were performed in two tests, CBC_090217_1139.csv and CBC_090217_1335.csv. The maps were made at speeds up to 50 krpm. Post test analysis shows that the compressor inlet was on the vapor side of the saturation curve. In spite of operating on the saturation curve, the data still show good agreement with the predicted compressor maps as described in the companion paper by Wright (Wright, 2009).

5.8.1.4 Near Steady-State Heating Test

The last test was SpinTest62_CBC_090217_1426 which was a near steady-state operation of the heated un-recuperated loop at a heating power of ~78 kW. A brief description of this transient is provided here. During the first portion of this test the water cooling flow through the loop was adjusted to match the heater power while keeping the compressor inlet conditions just above the critical point. The power was estimated by using the requested fractional power requested for each heater and assuming 130 kW per heater. For this test, the water inlet temperature was 77°F. Prior to the high speed transient the shaft speed was at an idle speed of 10,000 rpm and the flow rate was 0.91 lb/s. At this very low flow and with the heaters operating, the turbine inlet temperature was 182°F, but the heater element temperature was 440°F (and increasing). The high speed transient was then started by increasing the shaft speed to 45,000 rpm which increased the flow rate to 3.2 lb/s. After a spike in temperature and mass flow rate, the system began to "approach" near steady-state conditions.

During the "near steady-state" portion of the test, the compressor inlet temperature and pressure was 94.5°F and 1149 psia and changing only slowly. These temperatures were well above the critical point (87.7°F and 1069 psia). The turbine inlet temperature at this time was 134.3°F and the CO_2 thermal power increase was near 80 kW. This is a relatively low turbine inlet temperature but as will be shown in the next section, our analysis shows that the turbine was producing about ~7 kW or about as much power as the compressor was consuming. The measured test data results are shown in Figure 5-36 through Figure 5-40.

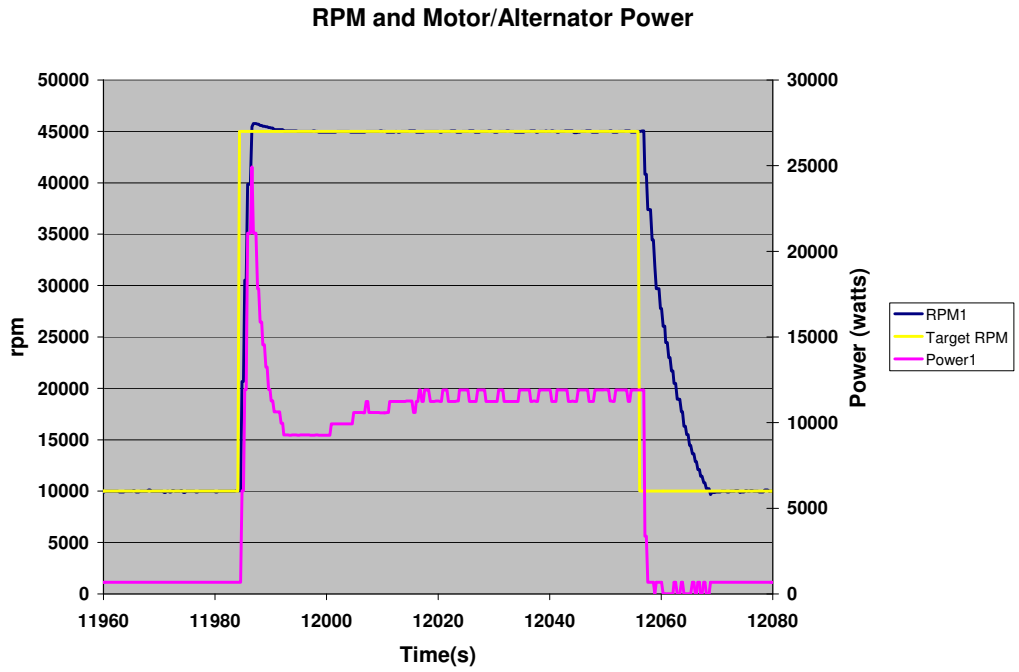

Figure 5-36: Measured shaft speed (rpm1), motor controller power, and target rpm for SpinTest62_CBC_090217_1426. The motor power is measured in the motor controller. The shaft power is approximately 93% of this value which accounts for losses in the electrical switching and magnetic losses in the stator. Note that near the end of this transient run the motor controller power is ~19 kW.

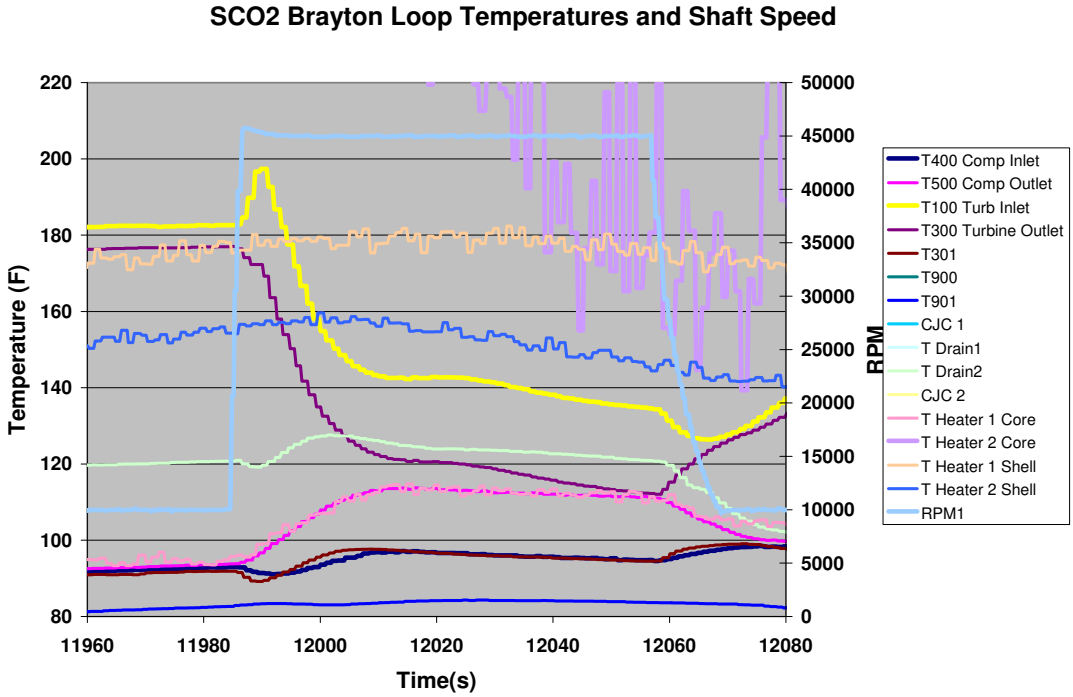

Figure 5-37: Measured temperature at the compressor and turbine inlet. T400 and T500 are the compressor inlet and outlet total temperatures. T100 and T300 are the turbine inlet and outlet temperatures. These values together with the pressures are used to determine the inlet and outlet enthalpy values.

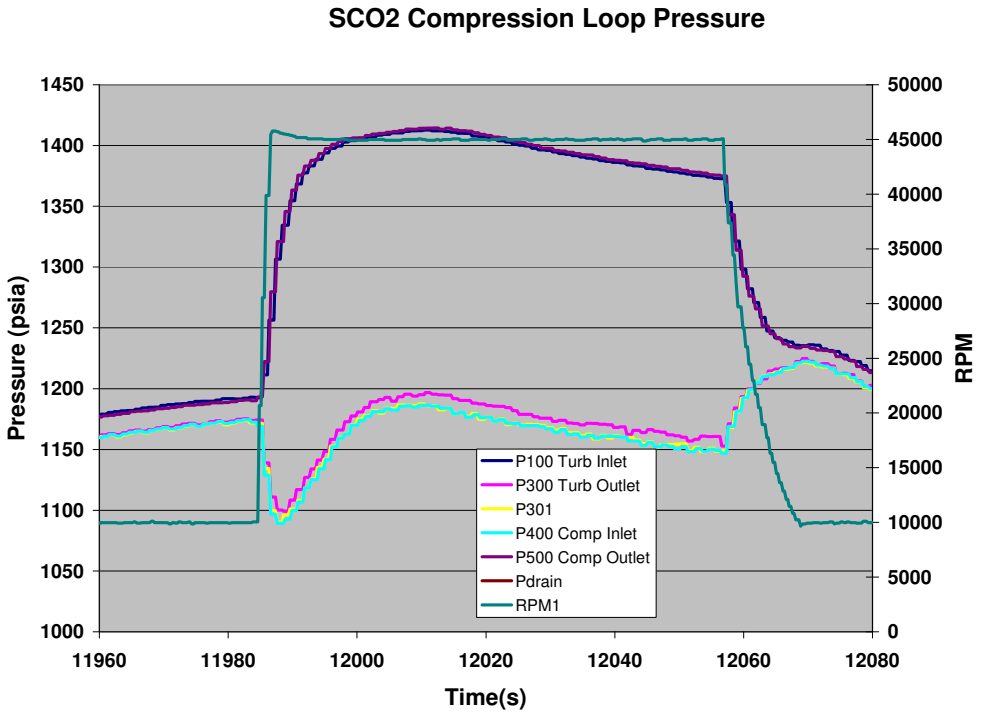

Figure 5-38: Measured pressures at the compressor and turbine inlet. P400 and P500 are the compressor inlet and outlet total pressure. P100 andP300 are the turbine inlet and outlet pressures.

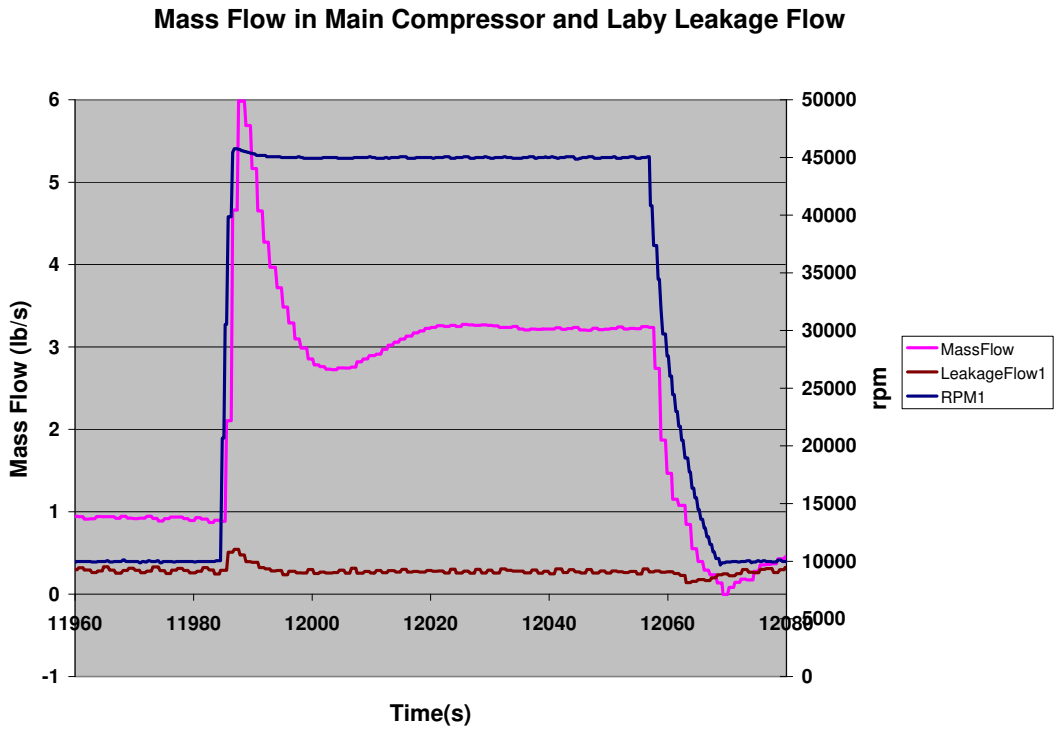

Figure 5-39: Measured mass flow rate (Magenta) and leakage flow rate (brown). The flow rate was measured by the coriolis flow meter.

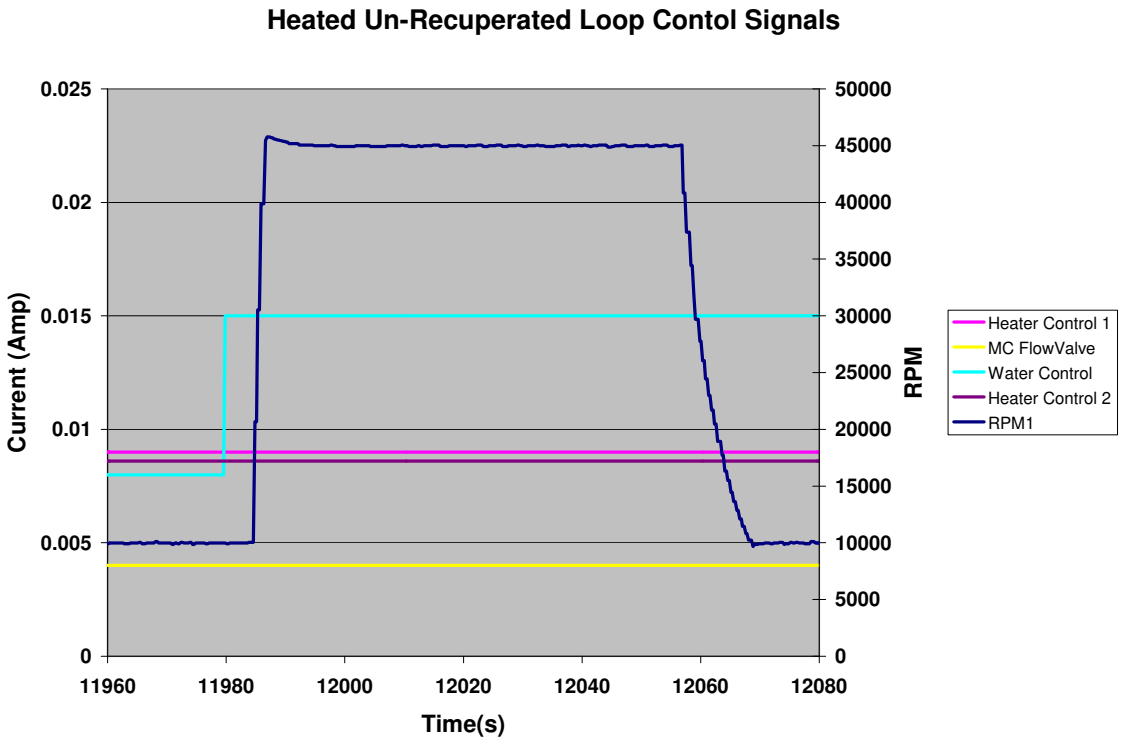

Figure 5-40: Control positions during the spin test. Heater controller 1 and 2 were operating at ~9 mA and 8 mA, respectively. As these are 4-10 mA controllers , we estimate the total power to be ~78. kW.

The measured data shown above provide the temperature and pressure at the inlet and outlet of every component in the loop. With this information, it is possible to estimate the enthalpy change and power of that component, given the measured flow rate. The initial results of this analysis are shown in Figure 5-41 and Figure 5-42. The power transferred to the fluid in the heater and the gas chiller is shown in Figure 5-41. Note that the values are nearly identical indicating that initially the system was near steady-state. During the high speed transient the heaters and gas chiller initially began to transfer approximately 300 kW but quickly settled down to approximately 80 kW which is near the electrical heater power. If true steady state conditions were achieved the gas chiller should be rejecting the heater power plus the motor power (~ 10 kW), but this is not observed in this simple analysis. This may simply be, because the mass flow rate was not adjusted to account for leakage flows. Also for the magnitude of the heat being transferred (~80 kW), one could easily envision uncertainties due to transient heat transfer effects on the order of a few kWs which could easily obscure these secondary effects.

The estimated power in the turbine (magenta) and the compressor (yellow) are shown in Figure 5-42. Notice that the turbine power nearly equals the compressor power but exceeds the compressor power by a few kW near the end of the transient. This indicates that the turbine was producing more power than the compressor was consuming, which means we were close to break-even conditions. Also note that the motor power (brown) is very close to the windage power (purple), which further indicates near break-even conditions. As mentioned, this analysis is not complete and we have not taken into account the leakage flow rates, nor have we accounted for the heat losses to plumbing due to transient heating and cooling effects. Two other similar transients at lower temperatures were performed (not shown), and they all

confirm the analysis that is provided here. A more complete and thorough energy balance still needs to be applied, but for the present it appears that except for losses (windage, bearing friction, pump-out vane losses, electrical, magnetic, thermal heat losses) the TAC appeared to be approaching break-even operating conditions.

Future testing will increase the heater power to 260 kW, at which time we hope to more clearly identify the break-even operating point for this very small turbine. The turbine that we are using was only meant to provide some turbo assist and was not designed to produce power in this loop. It is also important to get the loop operating with gas foil bearings as they will be needed to truly reach steady-state conditions.

A few other observations are important to make. First, the loop operates very much like the small low pressure closed Brayton loop that Sandia has been operating for the past 3 years (Wright, 2006). One observation is that as the shaft speed increases the high pressure leg increases while the low pressure leg decreases (see Figure 5-38). The magnitude of the pressure rise is controlled by the ratio of volumes in the low pressure and high pressure leg's of the loop and the fill inventory. Also we observe that as the loop heats, all the pressures increase. Probably the most striking observation is that because of the high power density and low mass of the system, the loop can change temperatures and pressures very rapidly. For example, in these tests the structure and gas temperatures in the loop essentially found new equilibrium temperatures in 1-2 minutes at 50% speed and at 10% power. Therefore, at full speed and full power the new equilibrium values will be observed in just 10-15 seconds. Thus the S-CO_2 Brayton loop has a very rapid time response.

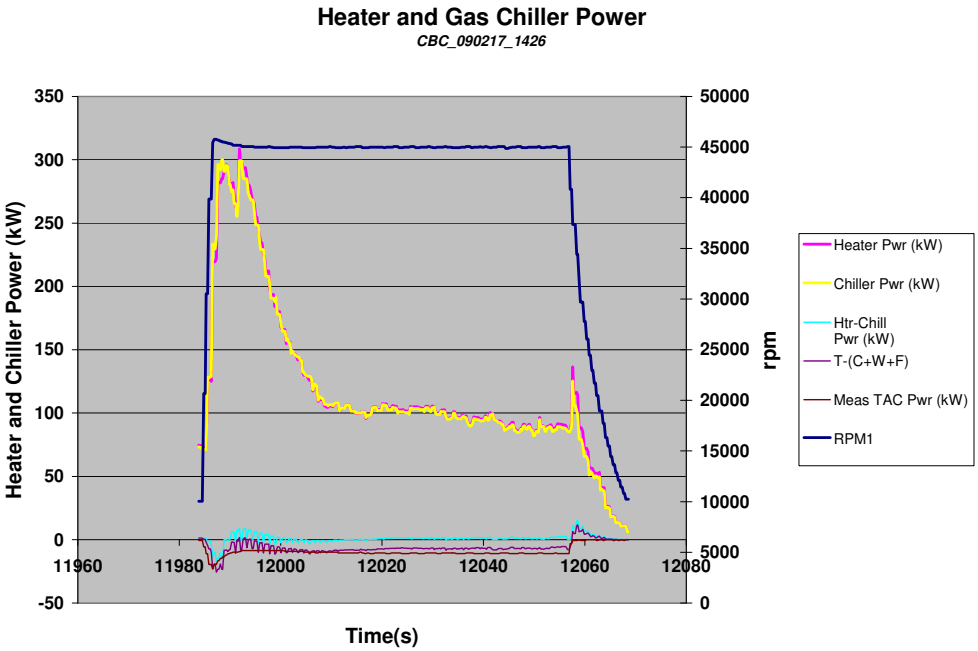

Figure 5-41: Estimate of power removed from the heater (magenta) and lost in the gas chiller assuming constant flow around the loop.

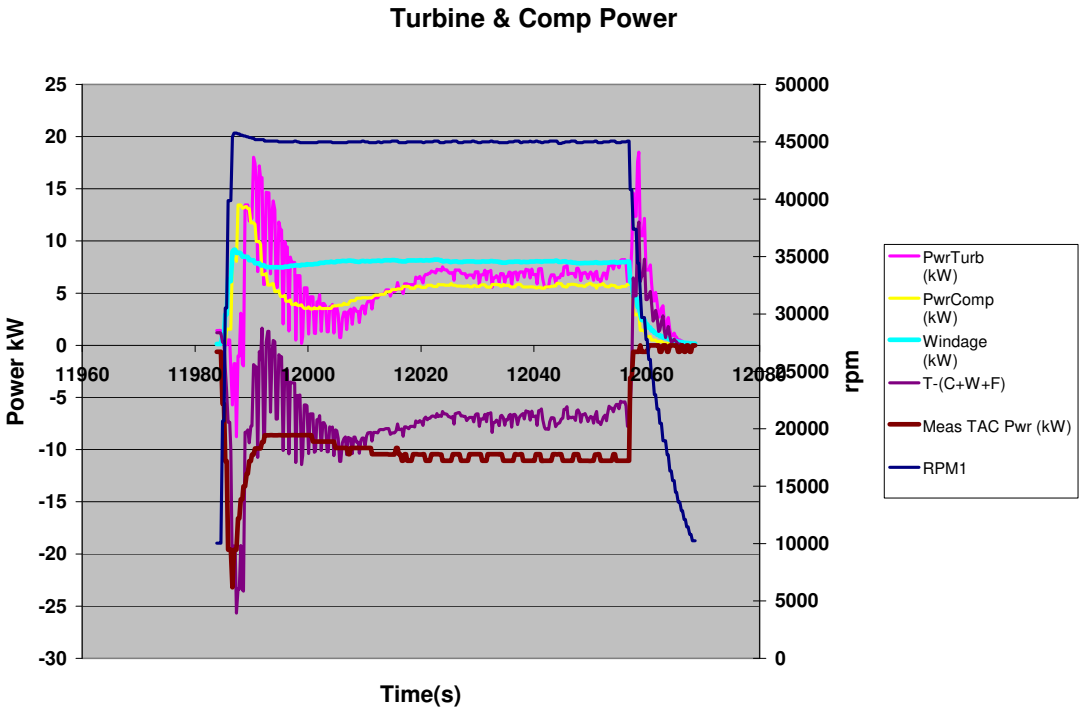

Figure 5-42: Measured power in the turbine (magenta) versus the compressor (purple). The TAC shaft power (brown) was estimated from the measured motor controller power and then reduced by 7% to account for electrical and magnetic losses.

6 CONCLUSIONS

The initial results obtained from the small scale Brayton cycle loop developed under this LDRD have provided the first experimental data on compression near the critical point of CO_2. Stable operation of the compression stage in this region of non-linear working fluid properties was a critical issue for establishing the viability of this cycle, The results obtained in this project demonstrated stable and controllable operation near the critical point over a range of conditions and confirmed the performance potential of these cycles. The small scale loop used modular and reconfigurable hardware to allow the flexibility to construct a range of compression and Brayton cycle configurations, and also to serve as a test bed for the development of the key bearing, seal, and controller technology necessary for loop operations. .

The key component of these loops is the turbo-alternator-compressor unit and the technologies used in its design. In its final configuration, the TAC uses gas foil bearings, a high speed permanent magnet motor/alternator and labyrinth gas seals to reduce the rotor cavity pressure. Because of the extremely high power densities and fluid density, Sandia has filed a Technical Advance for the TAC design. The early tests are focused on measuring leakage flow rates, windage losses, balancing thrust loads and measuring the compressor performance characteristics. Many of these early tests used ball bearings (with limited life) rather than gas foil bearings to allow for early testing and to minimize gas foil bearing development risks. The results of these tests were discussed in this report.

The compression loop has been operating for over a year. Nearly 100 test operations have been performed on the loop including measurements of the compressor performance map, the thrust loads (with just a compressor or with a small turbine), labyrinth seal leakage tests, operations in the two-phase region, and operations using gas foil bearings. The loop has been operated up to speeds of 65,000 rpm and at flow rates of 4 lb/s and at a pressure ratio of 1.65. Future testing will focus on measuring the performance maps for different compressor inlet conditions but still near the critical point. Other tests will explore surge conditions. Testing will also be performed with gas-foil bearings and various types of seals to determine the compatibility of these seals with gas-foil bearings and to estimate or determine seal leakage flow rates.

In general, the measured data from the supercritical CO_2 compression loop agree with our models. However, we are still early in the test program and more data needs to be measured over a wide range of conditions. Although these are only the first results to be analyzed, these results indicate that the basic design and performance predictions are sound. For example, we believe that the measured compression loop efficiency maps validate the “similarity” approach used to predict the performance curves and to design the compressors and turbines. The compression test loop is now the test bed that has largely confirmed the parameters to support the next stage of development, which is a 1 MW heater-class split-flow re-compressor Brayton cycle that will be capable of generating up to 250 kWe.

This page intentionally left blank.

7 References

Barber Nichols Incorporated, www.barber-nichols.com, 2008.

Bird, R B., W. E. Stewart, and E. N. Lightfoot. *Transport Phenomena*, J. Wiley & Sons, New York, NY, p 259, 1969.

Bruckner R.J. and DellaCorte C., "Windage Power Loss in Gas Foil Bearings and the Rotor-Stator Clearance of High Speed Generators Operating in High Pressure Carbon Dioxide Environments", *Proceedings Supercritical CO_2 Power Cycle Symposium,* Rensselaer Polytechnic Institute, Troy, NY, USA, April 29-30, 2009.

DellaCorte, C. Personal communication and presentation to SNL, NASA Glenn Research Center, Cleveland, Ohio, 2006.

Dostal, V. Driscoll, M.J. and Hejzlar, P. "A Supercritical Carbon Dioxide Cycle for Next Generation Nuclear Reactors," MIT-ANP-TR-100, March 2004

Egli A., "Leakage of Steam through Labyrinth Seals", Trans ASME, 57, pp. 115–122, 1937.

Galvas M. R., Fortran Program for Predicting Off-Design Performance of Centrifugal Compressors, NASA TN D-7487, 1973.

Glassman A. J., Turbine Design and Application, NASA SP-290, pp 58-60, 1972.

Gong, Y, et al. "Analysis of Radial Compressor Options for Supercritical CO_2 Power Conversion Cycles," MIT-GFR-034, June 2006

Heatric, a Meggit Group, http://www.heatric.com/, Dorset, UK, 2008.

Japikse, D. and N.C. Baines. *Introduction to Turbomachinery*, Concepts ETI Inc. and Oxford University Press, 1997.

Japikse, D. *Centrifugal Compressor Design and Performance*, Concepts ETI Inc. 1996.

Jiang W., Khan J., Dougal R., "Dynamic centrifugal compressor model for system simulation", *Journal of Power Sources, No. 158, pages 1333-1343, 2006.*

Lemmon E.W., Huber M.L., McLinden M.O., NIST Standard Reference Database 23: Reference Fluid Thermodynamic and Transport Properties-REFPROP, Version 8.0, National Institute of Standards and Technology, Standard Reference Data Program, Gaithersburg, 2007.

Martin H.M., "Labyrinth Packings", Engineering, Jan 10, pp 35-36, 1908.

Mathworks, www.mathworks.com, 2008.

National Instruments, www.ni.com/labview, 2008.

Noall, J. and Forsha, M. "Off-Design Turbo-machinery Performance Mapping", Internal Barber Nichols Inc, Program Report, September 26, 2008.

Oh, H.W., Yoon E.S., Chung M.K., "An optimum set of loss models for performance prediction of centrifugal compressors", *Proc. Instn Mech Engrs, Vol. 211 Part A, Pages 331-338, 1997.*

PrimeCore Systems Incorporated, www.pcsvi.com, 2008.

Vermes G. "A Fluid Mechanics Approach to the Labyrinth Seal Leakage Problem" Enineering, Series D, Vol. 81, 1959, pp 332-340.

Vranick, J.E., *Predicitoin of Windage Power Loss in Alternators,* NASA TN D-4849, NASA Lewis Research Center, Cleveland, Ohio, October 1968.

Wasserbauer, C.A. and Glassman, A.J. "FORTRAN Program for Predicting Off-Design Performance of Radial-Inflow Turbines", NASA TN D-8063, 1975.

Watlow Electric Manufacturing Company, www.watlow.com, St. Louis, Missouri, March 2008.

Wright S.A., Fuller R., et. al. , "Operational Results of a Closed Brayton Cycle Test-Loop," Proceedings of Space Technology and Applications International Forum (STAIF-2005), February, AIP Conference Proceedings, Albuquerque, NM, February 2005.

Wright S. A.,. Lipinski R. J., et. al., *Closed Brayton Cycle Power Conversion Systems for Nuclear Reactors, Modeling, Operations, and Validation*, SAND2006-2518, Sandia National Laboratories, Albuquerque, NM, 2006.

Wright S.A., Lipinski R.J., "Self-Driven Decay Heat Removal in a GCR Closed Brayton Cycle Power System", in *Proceedings of International Congress on Advances in Nuclear Power Plants*, June 4-8, 2006.

Wright S. A., Vernon M. E, .Pickard P.S., "Final Design for the Small Scale S-CO_2 Brayton Cycle Demonstration System for Gen IV Power Conversion", DOE Gen IV progress report, June 1, 2007.

Wright S. A., Vernon M. E, .Pickard P.S., "Status Report of Small Scale S- CO_2 Brayton Cycle Demonstration Program", DOE Gen IV progress report, September 11, 2007.

Wright S.A., Fuller R., et.al., "Supercritical CO_2 Brayton Cycle Compression and Control Near the Critical Point", Proceedings of International Congress on Advances in Nuclear Power Plants, June 8-12, Anaheim, California, 2008.

Wright S.A., Fuller R, et.al., "Initial status and test results for a supercritical CO_2 Brayton cycle test-loop", *Proceedings of International Congress on Advances in Nuclear Power Plants*, June 8-12, Anaheim, California, 2008.

Wright S. A., Pickard P.S., "Design of the Gen IV Supercritical CO_2 Split-flow Compressor Test Loop", DOE Gen IV progress report, February 29, 2008.

Wright S.A., Ross Radel, Milton Vernon, Heather Schriner, and Paul Pickard, "Analysis of Supercritical CO_2 Compressor Operation Near the Critical Point of CO_2", DOE Gen IV progress report, June 30, 2008.

Wright, S.A., Radel, R, Vernon, M. and Pickard, P. "Gen IV S- CO_2 Brayton Cycle Test Loop Design and Split-flow S- CO_2 Compressor Test Loop Construction Description" DOE Gen IV progress report, September 15, 2009Wright S.A., Pickard P.S. Fuller R, Radel R.F. Vernon M.E., "Supercritical CO_2 Compression Loop Operation and Test Results", in *Proceedings Supercritical CO_2 Power Cycle Symposium,* Rensselaer Polytechnic Institute, Troy, NY, USA, April 29-30, 2009.

Wright S.A., Pickard P.S. Fuller R, Radel R.F. Vernon M.E., "Supercritical CO_2 Heated, but Un-recuperated, Brayton Loop Operation and Test Results", in *Proceedings Supercritical CO_2Power Cycle Symposium,* Rensselaer Polytechnic Institute, Troy, NY, USA, April 29-30, 2009.

Wright S. A., Pickard P.S., "Supercritical CO_2 Test Loop Operation and First Test Results", *Proceedings of the International Congress on Advances in Nuclear Power Plants*, May 10-14, Tokyo, 2009.

Wright S.A., P.S. Pickard, Fuller R., Radel R.F., Vernon M.E., "Supercritical CO_2 Brayton Cycle Power Generation Development Program and Initial Test Results", in Proceedings of the ASME Power 2009 Conference, ASME Power 2009, Albuquerque, New Mexico, July 21-23, 2009.

Wright S.A., P.S. Pickard, Vernon M.E., Radel R.F., " Description and Test Results from a Supercritical CO_2", in Proceedings of 7th International Energy Conversion Engineering Conference, August 2-5, Denver, Colorado, 2009.

THIS PAGE IS INTENTIONALLY BLANK

Distribution

EXTERNAL

1 Barber Nichols Inc.
Attn: Bob Fuller
6325 W. 55th Ave
Arvada, Colorado 80002

1 Barber Nichols Inc.
Attn: Bill Batten
6325 W. 55th Ave
Arvada, Colorado 80002

1 Barber Nichols Inc.
Attn: Ken Nichols
6325 W. 55th Ave
Arvada, Colorado 80002

1 MIT Department of Nuclear Science and Engineering
Attn: Michael Driscol
77 Massachusetts Avenue
Cambridge, MA 02139

1 MIT Department of Nuclear Science and Engineering
Attn: Ron Ballinger
77 Massachusetts Avenue
Cambridge, MA 02139

1 Department of Energy
Attn: Tom O'Connor, DOE/NE-33
19901 Germantown, MD 20874

1 Department of Energy
Attn: Robert Versluis, DOE/NE-33
19901 Germantown, MD 20874

1 Department of Energy
Attn: Carl Sink, DOE/NE-33
19901 Germantown, MD 20874

1 Department of Energy
Attn: Schott Harlow, DOE/NE-34
19901 Germantown, MD 20874

1 Department of Energy
Attn: B.P. Singh, DOE/NE-54
19901 Germantown, MD 20874

1 Department of Energy
Attn: Carter Savage, DOE/NE-54
19901 Germantown, MD 20874

1 Argonne National Laboratory
Attn: James Sienicki, NE
9700 S. Cass Avenue
Argonne, IL 60439

1 Argonne National Laboratory
Attn: Anton Moisseytsev, NE
9700 S. Cass Avenue
Argonne, IL 60439

1 Argonne National Laboratory
Dae Cho, NE
9700 S. Cass Avenue
Argonne, IL 60439

1 Argonne National Laboratory
Attn: Richard Vilim, NE
9700 S. Cass Avenue
Argonne, IL 60439

1 Argonne National Laboratory
Attn: Robert Hill, NE
9700 S. Cass Avenue
Argonne, IL 60439

1 Knolls Atomic Power Lab
Attn: Ken Kimball, 103
PO Box 1072
Schenectady, NY 12301

1 Knolls Atomic Power Lab
Attn: Rudy Cuervo, 103
PO Box 1072
Schenectady, NY 12301

1 Knolls Atomic Power Lab
Attn: Joe Nehrbaurer, 103
PO Box 1072
Schenectady, NY 12301

1 Knolls Atomic Power Lab
Attn: Joe McDonnel, 103
PO Box 1072
Schenectady, NY 12301

1 Bettis Atomic Power Laboratory
Attn: Dave Vargo
PO Box 79
West Mifflin, Pennsylvania 15122

1 Bettis Atomic Power Laboratory
Attn: Rick Siergiej
PO Box 79
West Mifflin, Pennsylvania 15122

1 Northrop Grumman Shipbuilding
Newport News, Va. Shipyard
Attn: Michael Rap
E86 Engineer 600-1
4101 Washington Avenue
Newport News, Virginia 23607-2770

1 NASA Glenn Research Center
Attn: Chris DellaCorte
21000 Brookpark Road
Cleveland, OH 44135

1 NASA Glenn Research Center
Attn: Lee Mason
21000 Brookpark Road
Cleveland, OH 44135

1 Oak Ridge National Laboratory
Attn: Lou Qualls, MS6165
P.O. Box 2008
Oak Ridge, TN 37831

1 Oak Ridge National Laboratory
Attn: Sherrell Greene, MS6162
P.O. Box 2008
Oak Ridge, TN 37831

1 Oak Ridge National Laboratory
Attn: Daniel Ingersoll MS6162
P.O. Box 2008
Oak Ridge, TN 37831

1 Idaho National Laboratory
Attn: Chang Oh
Mailing Address
Box 1625
Idaho Falls, ID 83415-3695

1 Idaho National Laboratory
Attn: James Werner
Mailing Address
Box 1625
Idaho Falls, ID 83415-3695

Internal

1	MS0736	John Kelly	6770
1	MS1136	Gary Rochau	6771
1	MS1136	Paul Pickard	6770
1	MS1136	Ross Radel	6771
5	MS1146	Steven A Wright	6771
1	MS1146	Milton Vernon	6771
1	MS1146	P. J. Griffin	6771
1	MS1146	Gary Harms	1384
1	MS0701	Marianne Walck	6700
1	MS0747	Ronald Lipinski	6774
1	MS1127	Nate Siegel	6337
1	MS1127	Rich Diver	6337
1	MS0734	Ellen Stechel	6339
1	MS0899	Technical Library	9536
1	MS0123	D. Chavez, LDRD Office	1011


Sandia National Laboratories